UC San Diego

UC San Diego Electronic Theses and Dissertations

Title

Development and Application of Decellularized Extracellular Matrix Hydrogels for Translational Regenerative Engineering

Permalink

https://escholarship.org/uc/item/2ch2t89s

Author

Zelus, Emma Isabel

Publication Date

2024

Peer reviewed|Thesis/dissertation

eScholarship.org Powered by the California Digital Library
University of California

UNIVERSITY OF CALIFORNIA SAN DIEGO

Development and Application of Decellularized Extracellular Matrix Hydrogels for Translational Regenerative Engineering

A Dissertation submitted in partial satisfaction of the

requirements for the degree Doctor of Philosophy

in

Bioengineering

by

Emma Isabel Zelus

Committee in charge:

Professor Karen L. Christman, Chair
Professor Marianna Alperin, Co-Chair
Professor Adam J. Engler
Professor Sameer B. Shah

2024

Copyright

Emma Isabel Zelus, 2024

All rights reserved.

The Dissertation of Emma Isabel Zelus is approved, and it is acceptable in quality and form for publication on microfilm and electronically.

University of California San Diego

2024

DEDICATION

To my parents, Brian and Cheryl, my brothers, Matt and Andrew,

and my loving partner, Chris.

TABLE OF CONTENTS

DISSERTATION APPROVAL PAGE....iii
DEDICATION....iv
TABLE OF CONTENTS....v
LIST OF FIGURES....viii
LIST OF TABLES....x
LIST OF ABBREVIATIONS....xi
ACKNOWLEDGEMENTS....xii
VITA....xv
ABSTRACT OF THE DISSERTATION....xvi
Chapter 1: Extracellular Matrix Hydrogels for Tissue Regeneration in Translationally Relevant Models....1
1.1 History of Decellularized Extracellular Matrix Biomaterials....1
1.2 Overview of Tissue Decellularization Techniques....2
1.2.1 Physical Decellularization Techniques....3
1.2.2 Chemical and Biologic Decellularization Agents....4
1.2.3 Manufacturing and Translation of Decellularized ECM Biomaterials: What Works?....7
1.3 Clinical Application of Decellularized ECM Biomaterials....9
1.3.1 Grafts and Sheets....9
1.3.2 Powders and Hydrogels....12
1.4 Understanding the Pro-Repair Mechanisms of Decellularized ECM Biomaterials....13
1.4.1 Overview of Decellularized ECM Biocompatibility and Bioactivity....13
1.4.2 Cellular Proliferation and Differentiation....14
1.4.3 Fibrosis and ECM Remodeling....15
1.4.4 Vascularization....16
1.4.5 Neural Regeneration....17
1.4.6 Immune Modulation....17
1.5 Conclusion: Expanding Translation of Decellularized ECM Biomaterials....20
1.6 Thesis Outline....21
Chapter 2: Immunomodulatory Extracellular Matrix Hydrogel Induces Tissue Regeneration in a Model of Partial Glossectomy....23
2.1 Introduction....23
2.2 Results....25
2.2.1 Determining optimal injection volume of SKM hydrogel....25
2.2.2 Higher volume of SKM hydrogel reduces scar formation in a rat model of partial glossectomy....27
2.2.3 SKM hydrogel improves muscle regeneration within scar region....28

2.2.4 SKM hydrogel upregulates pro-regenerative immune response, myogenic response, and angiogenic signaling 31
2.2.5 SKM hydrogel promotes microvasculature development 65
2.2.6 SKM injection leads to increased fibroadipogenic progenitors at 3 days post-injection and encourages myogenic growth 67
2.2.7 SKM injection mitigates area of injury as early as 7 days post-injection 70
2.3 Discussion 71
2.4 Conclusions 75
2.5 Materials and Methods 76
2.5.1 SKM Hydrogel Fabrication 76
2.5.2 Partial Glossectomy Model 76
2.5.3 Reliability of the SKM Injection and Volume Optimization 77
2.5.4 Histomorphological Assessment of SKM Therapeutic Efficacy 78
2.5.5 RNA Isolation, Nanostring Multiplex Gene Expression Analysis, and Bulk RNA Sequencing 80
2.5.6 Histological Characterization at Early Timepoints Post-Injection 82
2.5.7 Statistical Analysis 83
2.6 Acknowledgements 84
Chapter 3: Development of a Translationally Relevant Preclinical Model of Stress Urinary Incontinence and Preliminary Investigation of Extracellular Matrix Hydrogel Treatment 85
3.1 Introduction 85
3.2 Results 88
3.2.1 Single SBI model of SUI 88
3.2.2 Repeated SBI model of SUI 91
3.2.3 Retired Breeder model of SUI 93
3.2.4 Ovariectomy model of SUI 94
3.2.5 Correlation of functional data with skeletal muscle sphincter morphology in models of SUI 96
3.2.6 Choosing a model of SUI for evaluation of potential therapeutics 99
3.2.7 Optimization of EUS injection volume and retention of SKM in the EUS . 99
3.2.8 Injection of SKM hydrogel delivered to the EUS does not restore urethral function 103
3.2.9 Investigating the effect of SKM injection on EUS morphology 106
3.3 Discussion 106
3.4 Conclusion 110
3.5 Materials and Methods 110
3.5.1 Animal Use Approval Statement 110
3.5.2 Leak Point Pressure Measurement 110
3.5.3 Animal models of SUI 113

3.5.4 Histological assessment of EUS morphology in SUI models 115
3.5.5 SKM Hydrogel Fabrication 115
3.5.6 Optimization of SKM injection volume 116
3.5.7 Assessing effect of SKM injection on urethral function 117
3.5.8 Histological assessment of the effect of SKM injection on EUS morphology 117
3.6 Acknowledgements 118
Chapter 4: Development of a Novel Vaginal Extracellular Matrix Hydrogel for Combating Genitourinary Syndrome of Menopause 119
4.1 Introduction 119
4.2 Results 125
4.2.1 Fabrication and characterization of vaginal ECM (vECM) hydrogel 125
4.2.2 vECM improves epithelial thickness and morphology in ovariectomized rats 130
4.2.3 vECM improves smooth muscle thickness and modulates smooth muscle proliferation 135
4.2.4 Cells, particularly macrophages, are observed localizing to vECM in the vaginal lumen and fibromuscularis 138
4.2.5 vECM treatment recruits macrophages to vaginal tissues 143
4.3 Discussion 145
4.4 Conclusion 148
4.5 Materials and Methods 148
4.5.1 vECM hydrogel fabrication and characterization 148
4.5.2 Preparation of vECM and collagen for intravaginal administration 150
4.5.3 Intravaginal administration of saline, vECM, and collagen 150
4.5.4 Histological assessment of epithelial thickness 151
4.5.5 Histological assessment of epithelial stem cell activity and phenotype . 151
4.5.6 Histological assessment of smooth muscle thickness and proliferation 152
4.5.7 Histological assessment of macrophage infiltration and phenotype after treatment 153
4.5.8 Intravaginal administration of fluorescently prelabeled vECM and macrophage staining at early timepoints 154
4.5.9 Statistical analysis 155
4.6 Acknowledgements 155
Chapter 5: Conclusions and Future Directions 156
5.1 Summary of Work 156
5.2 Future Directions and Outlooks 159
REFERENCES 162

LIST OF FIGURES

Figure 1.1 Graphical depiction of the effect of decellularization on tissue composition .. 2

Figure 1.2 Overview of Decellularization Methods 2

Figure 2.1 SKM hydrogel injection volume optimization after tongue partial glossectomy injury..... 26

Figure 2.2 SKM injection after partial glossectomy injury reduces scar formation..... 28

Figure 2.3 SKM Injection improves muscle regeneration within scar area. 30

Figure 2.4 Muscle fibers within scar of SKM and saline injected animals are smaller than healthy, but there is no difference in proportion of centralized nuclei..... 31

Figure 2.5 SKM injections induce significant differential transcriptomic expression when compared to both no injection and saline control groups. 36

Figure 2.6 SKM injection stimulates muscle regeneration and immune response related pathways and genes as demonstrated through differential bulk RNA sequencing analysis. 44

Figure 2.7 SKM injection promotes a transient increase in vasculature development.. 67

Figure 2.8 Fibroadipogenic progenitors are more prominent in the SKM group 3 days post-injection and are colocalized with developing myofibers within the SKM scaffold. 69

Figure 2.9 SKM injection mitigates area of injury as early as 7 days post-injection..... 71

Figure 3.1 Vaginal distention simulates childbirth injury and results in damage to the external urethral sphincter..... 86

Figure 3.2 Single SBI injury model produces divergent results, with inconsistent establishment of urethral function deficit. 90

Figure 3.3 Repeated SBI injury model does not produce consistent urethral function deficit..... 92

Figure 3.4 Retired Breeder injury model is insufficient for establishing stress urinary incontinence phenotype 94

Figure 3.5 Ovariectomy with repeated injury produces a relatively more consistent model of urinary incontinence at the cost of experimental duration 95

Figure 3.6 Histological assessment of external urethral sphincter and correlation between histological and functional data in models of stress urinary incontinence..... 98

Figure 3.7 Urethral morphology after injection of different materials to the EUS and retention of SKM in the EUS 102

Figure 3.8 Urethral function following SKM or saline injection..... 105

Figure 3.9 Skeletal muscle sphincter histomorphology following SKM or saline injection 106

Figure 3.10 Diagram of leak point pressure experimental setup 112

Figure 4.1 Histology of vaginal tissue layers. 119

Figure 4.2 Downstream effects of hypoestrogenism in vaginal tissues 121

Figure 4.3 Cellular proliferation assay performed with mouse vascular smooth muscle cells. 123

Figure 4.4 Production of a porcine vaginal tissue derived ECM hydrogel..... 127

Figure 4.5 H&E staining of porcine vaginal tissue throughout the decellularization process 128

Figure 4.6 Encapsulation of L929 and HUVEC cells in vECM to assess cytocompatibility 130

Figure 4.7 Evaluation of vECM efficacy in restoring vaginal epithelium in menopausal rats 132

Figure 4.8 Characterization of vaginal epithelial phenotype in vECM treated animals 134

Figure 4.9 Evaluation of vECM efficacy in restoring vaginal smooth muscle in menopausal rats..... 136

Figure 4.10 Assessment of vaginal smooth muscle cell proliferation following treatment 137

Figure 4.11 Retention of and cellular interaction with vECM at 1, 2, and 3 days post administration..... 139

Figure 4.12 vECM is observed colocalized with M2 macrophages and other cells in the vaginal fibromuscularis..... 140

Figure 4.13 Confocal imaging of M2 macrophages with vECM in vaginal lumen and fibromuscularis 142

Figure 4.14 Assessment of macrophage infiltration in vaginal tissues after treatment 144

LIST OF TABLES

Table 1.1 FDA Approved and Clinically Used Decellularized ECM Grafts and Sheets... 9

Table 2.1 List of genes included in custom NanoString panel. 37

Table 2.2 List of differentially expressed genes for NanoString multiplex gene expression experiment: day 3 post-injection, SKM vs no injection. 40

Table 2.3 List of differentially expressed genes for NanoString multiplex gene expression experiment: day 7 post-injection, SKM vs no injection. 42

Table 2.4 List of differentially expressed genes for NanoString multiplex gene expression experiment: day 3 post-injection, SKM vs saline. 43

Table 2.5 List of differentially expressed genes for NanoString multiplex gene expression experiment: day 7 post-injection, SKM vs saline. 43

Table 2.6 List of differentially expressed genes for bulk RNA sequencing transcriptomics experiment: day 3 post-injection, SKM vs no injection. 46

Table 2.7 List of differentially expressed genes for bulk RNA sequencing transcriptomics experiment: day 7 post-injection, SKM vs no injection. 54

Table 2.8 List of differentially expressed genes for bulk RNA sequencing transcriptomics experiment: day 3 post-injection, SKM vs saline. 64

Table 2.9 List of differentially expressed genes for bulk RNA sequencing transcriptomics experiment: day 7 post-injection, SKM vs saline. 64

Table 3.1 Summary of SUI models tested and their recovery rates 99

Table 4.1 vECM batches and processing variables 126

Table 4.2 Material characterization assays performed on vECM 129

LIST OF ABBREVIATIONS

ECM	Extracellular Matrix
EUS	External Urethral Sphincter
GSM	Genitourinary Syndrome of Menopause
IAS	Internal Urethral Sphincter
SBI	Simulated Birth Injury
SDS	Sodium Dodecyl Sulfate
SKM	Decellularized Skeletal Muscle Derived Extracellular Matrix
SUI	Stress Urinary Incontinence
vECM	Decellularized Vaginal Tissue Derived Extracellular Matrix

ACKNOWLEDGEMENTS

I would like to thank my advisors, Karen Christman and Marianna Alperin, for their mentorship, guidance, and support for the years that I have been working with them. Karen has encouraged my growth as a researcher and individual even when I began as an undergraduate in the lab, and she has fostered my passion for translational research. Karen has provided me countless opportunities to learn about biomaterials, manufacturing development, and regulatory practices, and I am fortunate to have the opportunity to continue working with her after my PhD in getting ECM biomaterials from the bench to the clinic. Marianna has been a tremendous inspiration throughout my PhD, and I would not have pursued this path without the passion for women's health research that she fostered in me. My core motivation has always been my desire to impact patient lives, and Marianna has always provided the clinical and patient perspective which has been vital to my growth as a researcher and individual. I am extremely fortunate and grateful to have worked through my PhD research under the unique coadvisement of both Karen and Marianna, combining expertise on biomaterials, regenerative engineering, translational research, women's health, and clinical applications. I am also forever thankful for their support and encouragement of me through the many setbacks and difficulties I've faced along the way.

I would like to thank Adam Engler and Sameer Shah for participating in my committee and providing critical feedback that has helped to shape and refine my dissertation research. I would like to thank Andrew Vahabzadeh-Hagh, whom I collaborated closely with for tongue fibrosis project, for all of his help with animal

procedures and for being incredibly kind and supportive throughout the last few years that we have worked together.

I have been fortunate to belong to both the Christman and Alperin labs throughout my doctoral studies, and I'm grateful for all of the support, friendships, advice, and feedback throughout the years. I would like to thank all members of both the Christman and Alperin labs, both past and present. In particular, I have to express my enormous gratitude to Pamela Duran for the incredible mentorship and friendship she has given me ever since I joined the Christman lab as an undergraduate sectioner in 2017. Pamela spearheaded the biomaterials for women's health collaboration between Karen and Marianna, and this dissertation genuinely would not have been possible without her. She has been an excellent role model and the dearest friend, and I will always look up to her as an incredibly hard-working scientist and genuinely kind person. I must also thank Danna Du, who embarked with me on the long and winding journey to apply ECM hydrogels in a model of stress incontinence. Together, we encountered a lot of difficulties and setbacks, but she has been a fantastic partner to share the work on this project with. She has also been a phenomenal roommate and friend, and I am excited to see her complete her master's thesis. Lastly, I would like to thank all of the undergraduate students that I have mentored and worked with, including Aaron Panduro, Vanessa Cini, Isha Deshmukh, Jacqueline Grime, Alexa Roa, and Ellio Ou.

I would like to thank all of my friends outside of lab as well for helping me get through grad school – I cherish all the hikes, volleyball rallies, board game nights, happy hours, and dinners we've shared along with all of the conversations that don't revolve in any way, shape or form around work or research. I am endlessly thankful for my family –

my parents, Cheryl and Brian, and my brothers, Matt and Andrew – for their love, support, and especially for not asking when I'll be finished with my PhD. Finally, I would like to thank Chris for being the most fantastic partner throughout the hardest part of my graduate journey. He has been a steadfast source of love, support, and encouragement, and I would be in a very sorry state without his company, including all the motorcycle rides, electric unicycle adventures, beach explorations, and cozy mining time.

Chapter 2, in part, is a reprint of the material as it appears in Bioactive Materials 2024. Emma I. Zelus, Aaron Panduro, Isha Deshmukh, Jacqueline Grime, Marianna Alperin, Andre M. Vahabzadeh-Hagh, Karen L. Christman. The dissertation author was the primary researcher and author of this paper.

Chapter 3, in part is currently being prepared for submission for publication of the material. Emma I. Zelus, Danna Du, Marianna Alperin, Karen L. Christman. Danna Du contributed to the histological evaluation of various models of stress urinary incontinence, as well as the optimization of urethral injection methodology. The dissertation author was the primary researcher and author of this material.

Chapter 4, in part is currently being prepared for submission for publication of the material. Emma I. Zelus, Jacqueline Grime, Marianna Alperin, Karen L. Christman. The dissertation author was the primary researcher and author of this material.

VITA

2019 Bachelor of Science in Bioengineering (Biotechnology), University of California San Diego

2024 Doctor of Philosophy in Bioengineering, University of California San Diego

PUBLICATIONS

Pamela Duran, **Emma I. Zelus**, Lindsey Burnett, Karen L. Christman, Marianna Alperin. Repeated birth injuries lead to long-term pelvic floor muscle dysfunction in the preclinical rat model. American Journal of Obstetrics & Gynecology. 2024; in review.

Emma I. Zelus, Aaron Panduro, Isha Deshmukh, Jacqueline Grime, Marianna Alperin, Andrew M. Vahabzadeh-Hagh*, Karen L. Christman*. Immunomodulatory Extracellular Matrix Hydrogel Induces Tissue Regeneration in a Model of Partial Glossectomy. Bioactive Materials. 2024; in press. *Co-corresponding author.

Raymond M. Wang., Joshua M. Mesfin., Maria L. Karkanitsa, **Emma I. Zelus**, Jessica Ungerleider, Yuxue Zhang, Yu Kawakami, Yuko Kawakami, Toshiaki Kawakami, Karen L. Christman. Immunomodulatory Contribution of Mast Cells to the Biomaterial Microenvironment. NPJ Regenerative Medicine, 2023; 8, 53.

Melissa J. Hernandez, **Emma I. Zelus**, Martin T. Spang, Rebecca L. Braden, and Karen L. Christman. Dose Optimization of Decellularized Skeletal Muscle Extracellular Matrix Hydrogels for Improving Perfusion and Subsequent Validation in an Aged Hindlimb Ischemia Model. Biomaterials Science. 2020; 8:3511-3521.

Melissa J. Hernandez, Grace E. Yakutis, **Emma I. Zelus**, Ryan C.Hill, Monika Dzieciatkowska, Kirk C. Hansen, Karen L. Christman. Manufacturing Considerations for Producing and Assessing Decellularized Extracellular Matrix Hydrogels. Methods. 2020; 171:20-27.

ABSTRACT OF THE DISSERTATION

Development and Application of Decellularized Extracellular Matrix Hydrogels for Translational Regenerative Engineering

by

Emma Zelus

Doctor of Philosophy in Bioengineering

University of California San Diego, 2024

Professor Karen L. Christman, Chair
Professor Marianna Alperin, Co-Chair

Decellularized extracellular matrix (ECM) biomaterials have been used extensively in diverse clinical applications, and numerous preclinical studies have demonstrated their potential for regenerative tissue engineering. While decellularized ECM patches and sheets dominate the clinical space, ECM hydrogels, which are thermoresponsive and can be delivered to tissues minimally invasively, have seen increasing attention in preclinical research with a recent clinical application. Thus, with the goal of expanding clinical translation of decellularized ECM hydrogels, this dissertation presents a review of tissue decellularization techniques and the pro-repair mechanisms of ECM biomaterials as well as application of ECM hydrogels for regenerative tissue engineering in three different highly translational preclinical animal models of underserved soft tissue disorders.

In designing ECM hydrogels for tissue repair with the goal of clinical translation, it is critical to understand various decellularization techniques, their scalability and impact on manufacturing processes, and their history of use in clinical applications. Furthermore, we may utilize our knowledge of successful translation of ECM biomaterials and the mechanisms of pro-repair in established treatment models to inform novel design and application of ECM biomaterials. Utilizing these strategies, we have designed tissue-specific injectable ECM hydrogels for tissue regeneration in translational preclinical models of tongue fibrosis, stress urinary incontinence, and vaginal atrophy associated with genitourinary syndrome of menopause.

In all applications, ECM hydrogels demonstrate remarkable versatility and potential to mediate pro-repair in various soft tissue disorders. In a model of tongue fibrosis, skeletal muscle derived ECM hydrogel demonstrates reduction of scar formation, improvement of muscle regeneration, transient increase in neovascularization, and

modulation of the immune response towards a pro-repair and anti-inflammatory phenotype. In a model of stress urinary incontinence, ECM hydrogels may be used as a minimally invasive and highly targeted potential therapeutic, warranting further investigation. Finally, in a model of menopause, a tissue-specific ECM hydrogel improves both epithelial and smooth muscle repair despite being delivered through intravaginal administration, and anti-inflammatory macrophages are implicated in this pro-repair response spanning multiple layers of the vaginal tissue. Overall, the studies presented herein demonstrate the translational potential of ECM hydrogels for tissue regeneration in diverse applications.

Chapter 1: Extracellular Matrix Hydrogels for Tissue Regeneration in Translationally Relevant Models

1.1 History of Decellularized Extracellular Matrix Biomaterials

The extracellular matrix (ECM) is a complex network of proteins secreted by cells, serving both structural and biochemical function through cellular interactions. The ECM is comprised of collagens, elastin, fibronectin, laminin, glycosaminoglycans (GAG), and a variety of glycoproteins; though the specific composition of the ECM varies significantly among tissue types, owing to the diverse cell types that can secrete ECM.[1] The ECM is critical to supporting cell growth, differentiation, and migration, and as such, ECM structure and function has informed and guided the design of tissue regenerative therapeutic strategies for decades.

The first demonstration of decellularized ECM for tissue regeneration involved the use of small intestinal submucosa as arterial grafts in a preclinical animal model in 1990.[2] Following this initial investigation, further research in the 90s found that the decellularized small intestinal submucosa was superior to routine tissue culture matrices (i.e. Vitrogen, Matrigel), in promoting cell growth and differentiation.[3] These early studies gave rise to the modern day broad field of decellularized ECM materials as they are used for tissue-mimetic *in vitro* culture systems and tissue regenerative strategies. Presently, decellularization techniques for the production of ECM biomaterials have expanded tremendously, and decellularized ECM biomaterials have shown remarkable potentiation of endogenous tissue repair through the recruitment of cellular migration, promotion of cellular proliferation and differentiation, and modulation of cellular activity and interactions.

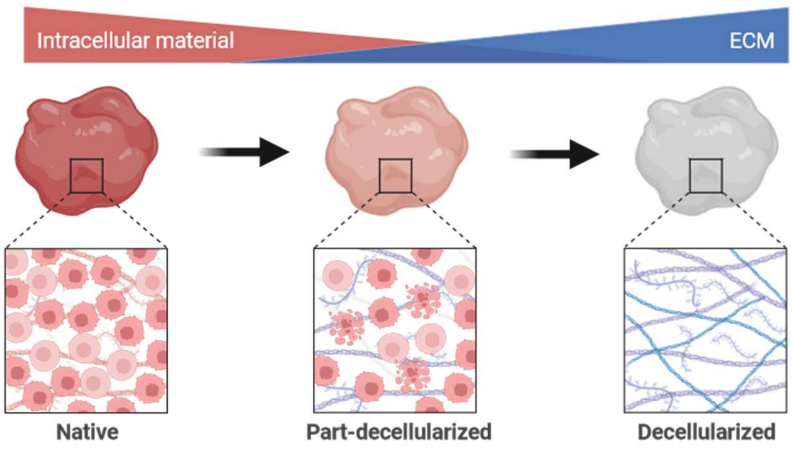


Figure 1.1 Graphical depiction of the effect of decellularization on tissue composition

1.2 Overview of Tissue Decellularization Techniques

Broadly, three methods may be used to decellularize tissue and produce ECM biomaterials: physical, chemical, and biological decellularization.[4] Different decellularization methods have a variety of benefits and drawbacks.

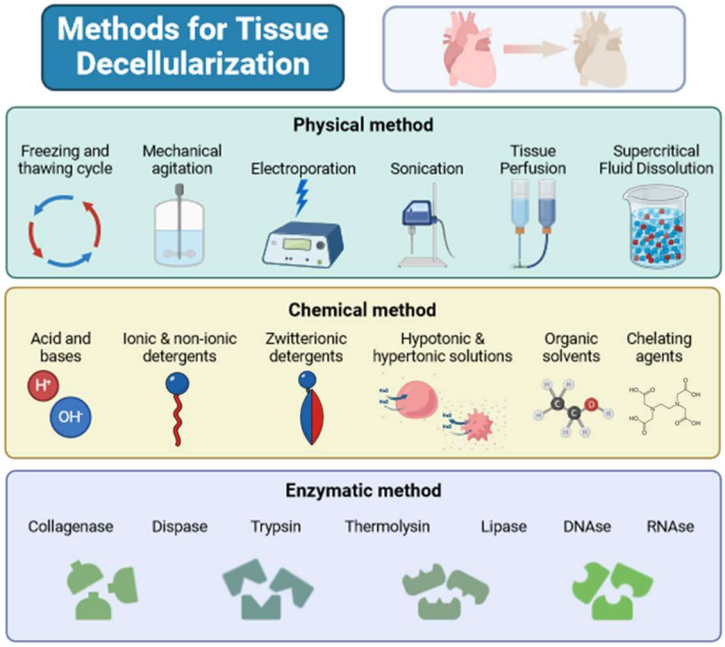


Figure 1.2 Overview of Decellularization Methods

1.2.1 Physical Decellularization Techniques

Basic physical decellularization techniques, which are usually used to aid delivery of chemical and biological decellularization agents, include freeze-thaw cycling, mechanical abrasion or agitation, and tissue perfusion. Freeze-thaw cycles are simple and cost-effective and do not contaminate the ECM with chemical or biological agents; however, they may not achieve complete cell removal, and the formation of ice crystals through repeat freeze-thaw cycles can damage the structural composition of the ECM.[5] Mechanical decellularization methods present much the same advantages and drawbacks as freeze-thaw cycling, but are largely useful as a means of accelerating circulation of chemical and biological agents as well as tissue clearing. Perfusion decellularization involves *in vivo* or *ex vivo* perfusion of the vascular tree of whole tissues, and it enables thorough and uniform decellularization while preserving native ECM and whole-tissue structure.[6] However, perfusion methods are complex to set up, costly, and time consuming; as such, they are not a viable method for scaled-up manufacturing processes to support translation of decellularized ECM therapeutics.[5]

Additional physical decellularization techniques which are useful for breaking down cell membranes and removing cellular content include electroporation, sonication, and super critical fluid dissolution. Nonthermal irreversible electroporation uses electricity to perforate cell membranes, causing cell death without negatively affecting the ECM structure.[5] When this technique is applied *in vivo*, the endogenous immune response can facilitate full clearing of the target tissue and effective decellularization by 3 days post electroporation, leaving a fully functional ECM scaffold.[7]

Sonication involves the use of high-frequency sound waves to disrupt cell membranes and release cellular content. This technique is useful initial breakdown of cells in the tissue but requires subsequent washes with chemical or biologic agents to achieve sufficient removal of cellular material from the tissue.[8] Dissolution of supercritical fluids, such as CO_2, is a more recent technique that has been tested in comparison to established decellularization techniques in application on a porcine heart.[9] Supercritical CO_2 dissolution decellularization can provide selective removal of cellular components while notably preserving ECM structure, and this process is notably scalable, having been used in a variety of food and drug applications.[9]

1.2.2 Chemical and Biologic Decellularization Agents

Chemical and biological agents used for decellularization include detergents, acids and bases, hypertonic and hypotonic solutions, organic solvents, chelating agents, and enzymes. In general, these agents are used in combination with physical decellularization techniques, such as mincing and immersed agitation of tissue, to enable the chemical or biological agent to effectively penetrate and thoroughly decellularize the tissue.[4,5] The primary drawback of all of these agents is the presence of residual chemicals or biologics in the tissue following decellularization. When considering the translational application and manufacturing development of decellularized ECM materials, it is vital to choose a decellularization agent which is either not harmful or can be sufficiently cleansed from the decellularized tissue. In the latter case, it is additionally important to reliably and accurately quantify the residual decellularization agent remaining in the tissue to facilitate the establishment of strict manufacturing quality control standards.

Several detergents have been identified as effective decellularization agents: ionic detergents (sodium dodecyl sulfate [SDS], sodium deoxycholate, and Triton X-200), non-ionic detergents (Triton X-100), and zwitterionic detergents (CHAPS and sulofbetaine-10 or -16).[8] SDS is highly effective at stripping cellular material from tissue but can compromise GAG content and disrupt the native ECM structure. SDS-based decellularized ECM biomaterials have been used extensively with well-established chemical assays to quantify residual detergent in decellularized tissues (Methylene Blue assay).[5] Sodium deoxycholate is a slightly less aggressive detergent and will better preserve the ECM structure at the cost of slightly less complete decellularization and longer processing time.[10] Triton X-200 is an ionic detergent that is more effective at removing cellular content from thin tissues but causes significant disruption of ECM ultrastructure; additionally, Triton X-200 is difficult to effectively remove from tissue and is thus a poor candidate for manufacturing-scale production of decellularized ECM.[11] Similarly, Triton X-100, which is the primary non-ionic detergent used, exhibits problems with residual detergent residing in the tissue following decellularization; however, it is a more gentle decellularization agent and results in better retention of ECM structure and composition, particularly GAGs.[8] Zwitterionic detergents are less commonly used, but owing to the presence of both anionic and cationic groups, they have a less disruptive effect on ECM structure and composition.[11] However, these reagents can be more costly and difficult to optimize, and zwitterionic detergents are more likely to denature proteins and compromise ECM function.[8]

Alkaline and acidic solutions are used to solubilize cytoplasmic cell components and remove nucleic acids. Acidic solutions (hydrochloric acid, acetic acid, sulfuric acid,

and peracetic acid) tend to produce a more thorough decellularization with the cost of higher risk of damage to ECM structure as compared to alkaline solutions (sodium hydroxide and ammonium hydroxide).[11] Of these reagents, peracetic acid is commonly used as a complementary decellularization reagent when working with thin, delicate structures.[8] Notably, alkaline and acidic solutions are more likely to compromise GAG and growth factor content when used for decellularization.[11]

Organic solvents used for decellularization include alcohols (ethanol, methanol), acetone, and tributyl phosphate (TBP). While effective for membrane disruption, organic solvents are not as effective in clearing cytoplasmic and nuclear content from tissues; as such, they are often combined with other agents to achieve complete decellularization.[11] Additionally, the use of alcohols and acetone as tissue fixatives means that they should be used as decellularization agents conservatively and with caution, as they can significantly can damage ECM ultrastructure and crosslink ECM to alter scaffold stiffness.[11,12]

Hypotonic and hypertonic solutions respectively have a significantly lower or higher concentration of solute compared to intracellular content, causing cell lysis when used as a decellularization agent. However, similar to organic solvents, they are less effective at thoroughly clearing cell debris and thus are often used in conjunction with other decellularization agents.[13]

Finally, biologics used for decellularization include chelating agents and various enzymes. Chelating agents, such as EDTA and EGTA, bind to metal ions to disrupt cell adhesion to the ECM as well as enzymatic activity. They are ineffective when used alone and are best used in conjunction with other options, like detergents or enzymes, as they

are generally a mild and biocompatible decellularization agent and protect the structure and composition of the native ECM.[14]

Enzymes used for decellularization include nucleases (RNAse, DNAse), trypsin, collagenase, dispase, lipase, and thermolysin. Nucleases effectively removed nuclear residues from decellularized tissue, which is important for reducing immunogenicity of ECM biomaterials, and are useful in conjunction with other decellularization agents to ensure complete removal of nucleic acids.[11] Trypsin is a serine protease often used in combination with EDTA for effective detachment and removal of cells; however, trypsin can easily degrade ECM protein content and must be used with caution.[8] Trypsin is thus useful as a brief step early in the decellularization process to detach cells and open up the matrix for more effective clearing with other decellularization agents.[11] Collagenase is specifically useful when decellularizing tissues with particularly dense collagen network and otherwise can easily compromise ECM structure and function.[13] Dispase and thermolysin are more neutral proteases that can aid in cellular removal without significant damage to ECM components if used conservatively, while lipase aids in delipidation of the ECM when used in conjunction with other decellularization agents.[11]

1.2.3 Manufacturing and Translation of Decellularized ECM Biomaterials: What Works?

It is evident that there is enormous variety in the decellularization methods currently available; different physical, chemical, and biologic techniques have distinct and unique advantages and disadvantages. To accommodate for significant variation in ECM composition between different tissues, the techniques discussed above can be combined and tuned to best suit the tissue characteristics and end goal of decellularization, which may vary from *in vitro* tissue modeling to creation of skin grafts for wound healing. In this

dissertation, the primary focus is the use of decellularized ECM biomaterials for translational and clinical applications; as such, it is important to understand the decellularization techniques that have proved most successful in generation of manufacturing-scale therapeutic decellularized ECM biomaterials.

For evaluating decellularization techniques in translational applications, the major considerations are scalability of the processes and establishment of rigorous and streamlined quality assurance/quality control (QA/QC) assays. As such, reagents may not be prohibitively expensive, and techniques should not require extensive manual intervention. QA/QC procedures should be relatively simple, robust and repeatable, and provide an efficient readout to decisively determine batch quality. This can include evaluation of decellularization through quantifying residual nuclei acid content with a PicoGreen assay,[8] quantification of residual chemical or biological decellularization agent, *in vitro* assessment of biocompatibility, and biomechanical testing to evaluate material properties of decellularized ECM biomaterials.

Of the decellularized ECM biomaterials which have been FDA approved and are manufactured for clinical translation, the most common approach is to utilize detergent based decellularization, sometimes with the addition of a brief enzymatic wash step. The most common chemical detergent used in translational decellularized ECM biomaterials is SDS, while Triton X-100 is used less frequently.[15] Enzymes used include DNAse and RNAse for degradation of nucleic acid and trypsin for assisting in cell removal prior to detergent washing, but these should be used with caution to avoid unnecessary addition of cytotoxic residuals and damage to ECM ultrastructure and composition.[15]

1.3 Clinical Application of Decellularized ECM Biomaterials

1.3.1 Grafts and Sheets

The most common form of decellularized ECM biomaterials used clinically are ECM patches, sheets, and grafts. These materials are decellularized tissues derived from both allogenic and xenogeneic sources with minimal downstream processing; tissue is isolated, decellularized, and formed into a thin, flexible, and typically shelf-stable matrix. The tissue source for these materials can include dermis, small intestinal submucosa, pericardium, and others. FDA approved clinical application of decellularized ECM patches and grafts includes chronic wound and burn healing, cardiovascular reconstruction, breast reconstruction, pelvic floor repair, and many more. The following table provides a comprehensive and historical overview of clinically used decellularized ECM grafts and sheets.[16–19]

Table 1.1 FDA Approved and Clinically Used Decellularized ECM Grafts and Sheets.

Device and Manufacturer	**Tissue Source**	**Clinical Application**
AlloDerm® LifeCell	Human dermis	Wound, hernia, pelvic, and breast reconstruction; dental soft tissue augmentation
AlloMax® CR Bard/Davol	Human dermis	Hernia, chest wall, and post-mastectomy breast reconstruction
Allopatch® Conmed	Human dermis	Tendon repair and augmentation
AlloSkin™ AlloSource	Human dermis	Wound healing
ArthroFlex® Arthrex	Human dermis	Soft tissue repair
Axis™ Coloplast	Human dermis	Pelvic floor repair and urethral sling implantation
AxoGuard® AxoGen	Porcine small intestinal submucosa	Peripheral nerve injury repair

Table 1.1 FDA Approved and Clinically Used Decellularized ECM Grafts and Sheets (continued).

Biodesign® Cook Medical	Porcine small intestinal submucosa	Otolaryngology head and neck surgery soft tissue repair
Cancello-Pure® Wright Medical Technology	Bovine bone	Bone graft
CardioCel® LeMaitre	Bovine pericardium	Heart repair and reconstruction, great vessel repair
CollaMend CR Bard/Davol	Porcine dermis, cross-linked	Hernia and abdominal wall repair
Conexa™ Tornier	Porcine dermis	Tendon repair and reinforcement
CorMatrix® CorMatrix Cardiovascular	Porcine small intestinal submucosa	Carotid repair, pericardial repair and reconstruction, cardiac tissue repair
Cortiva® RTI Surgical	Human dermis	Wound healing
CryoValve® CryoLife	Human pulmonary or aortic valves	Valve replacement, congenital reconstruction
CuffPatch® Arthrotek	Porcine small intestinal submucosa	Tendon repair
Cytal® ACell	Porcine urinary bladder matrix	Burn, wound, and surgical soft tissue repair
DermACELL® Novadaq	Human dermis	Wound healing, breast reconstruction
DermaMatrix® Synthes CMF	Human dermis	Oral cavity and soft tissue repair and augmentation, bone regeneration
DermaPure Tissue Regenix Group	Human dermis	Chronic wound healing
Endoform™ Aroa Biosurgery	Ovine forestomach submucosa	Acute and chronic wounds repair
Epiflex® Hannover Medical School	Human dermis	Burn and scar treatment, breast reconstruction
FasLata® Allograft C.R. Bard	Human fascia lata	Pelvic floor and pelvic organ prolapse reconstruction
FlexHD® Ethicon	Human dermis	Wound, hernia, and breast reconstruction
GraftJacket™ Wright Medical Technology	Human dermis	Tendon repair and reinforcement
Integra™ Integra Life Sciences	Bovine dermis, cross-linked	Burn wound healing

Table 1.1 FDA Approved and Clinically Used Decellularized ECM Grafts and Sheets (continued).

IntreXen™ American Medical Systems	Porcine dermis	Pelvic organ prolapse repair
Lyoplant® Aesculap	Pericardium	Dural repair and reconstruction in neurosurgery
MatriDerm® Dr Suwelack AG	Bovine dermis	Full- and split-thickness skin regeneration, burn wound healing
Medeor® Koninklijke DSM	Porcine dermis	Soft tissue repair and reinforcement
Meso BioMatrix™ Kensey Nash Corp	Porcine mesothelium	Congenital, surgical, or oncologic soft tissue defects repair
MiroDerm® Miromatrix Medical	Porcine liver	Wound healing
NeoForm™ Mentor Worldwide	Human dermis	Breast reconstruction
Oasis® Cook Biotech	Porcine small intestinal submucosa	Wound and surgical soft tissue repair
OrthADAPT Synovis Orthopedic and Wound Care	Equine pericardium	Apdominal and thoracic wall repair, muscle and soft tissue reinforcement
Permacol™ Medtronic	Porcine dermis, cross-linked	Hernia and abdominal wall and breast reconstruction
PhotoFix™ CryoLife	Bovine pericardium	Atrial, ventricle, and great vessel repair and pericardial closure
Prima™ Plus Edwards Life Sciences	Porcine heart valve	Valve replacement
Repliform® Boston Scientific	Human dermis	Enteroceles, retroceles, cystoceles, and pelvic floor repair
Restore™ DePuy Orthopedics	Porcine small intestine	Soft tissue repair
SJM™ St. Jude Medical	Bovine pericardium	Cardiovascular repair and reconstruction
Strattice™ LifeCell	Porcine dermis	Hernia and body wall repair, breast reconstruction
SurgiMend® Integra LifeSciences	Bovine dermis	Soft tissue repair: hernia repair, breast reconstruction
Surgisis® Cook Biotech	Porcine small intestinal submucosa	Pelvic and hernia reconstruction
Suspend® Coloplast	Human fascia lata	Pelvic floor repair and urethral sling implantation
TissueMend® TEI Biosciences	Fetal bovine dermis	Tendon repair and reinforcement

Table 1.1 FDA Approved and Clinically Used Decellularized ECM Grafts and Sheets (continued).

Tutopatch® RTI Surgical	Povine pericardium	Duraplasty, oral surgery, hernia, pelvic, and cardiac wall repair and reconstruction
Tutoplast® IOP Opthalmics	Human pericardium	Ophthalmic repair
Unite® Synovis Life Technologies	Equine pericardium	Soft tissue and chronic wound repair
Veritas® Synovis Surgical Innovations	Bovine pericardium	Pelvic floor, pelvic and rectal prolapse, and hernia repair
Xenform™ Boston Scientific	Bovine dermis	Pelvic floor defect and soft tissue repair
XenMatriX™ Devol	Porcine dermis	Hernia and abdominal wall repair
Zimmer Collagen™ Zimmer	Porcine dermis	Wound and surgical soft tissue repair

1.3.2 Powders and Hydrogels

While the clinical application of decellularized ECM biomaterials has been dominated by the various grafts and sheets discussed, the use of ECM powders and hydrogels has been investigated extensively preclinically and presents much more opportunities for clinical development. ECM powders are decellularized ECM materials that have been lyophilized and milled to a fine, uniform powder which can present a much more versatile form of ECM for tissue engineering and regenerative medicine approaches. MicroMatrix®, previously known as MatriStem, is a decellularized urinary bladder matrix powder developed by ACell, which produces Cytal® Wound Matrix. This material has seen extensive clinical used, including treatment of anal fistulas,[20] flap reinforcement in head and neck surgery,[21] treatment of nonhealing radiation wounds,[22] and chronic wound healing.[23] More recently, InnovaMatrix® has emerged as a porcine placental decellularized ECM powder for use in wound healing applications.[24]

Decellularized ECM powders may be further processed with enzymatic digestion to produce a liquid and injectable form of ECM that forms a gel when injected into tissues.[25] VentriGel, produced by Ventrix, was the first decellularized ECM hydrogel to be translated in humans. VentiGel was assessed in a phase 1 clinical trial for the transendocardial injection of a porcine left ventricle derived decellularized ECM hydrogel in patients who had undergone myocardial infarction.[26] This study confirmed safety and feasibility of VentriGel and suggested improvement in functional outcomes and left ventricular remodeling.[26]

While the use of decellularized ECM powders and hydrogels has been explored extensively in preclinical studies, incorporating a wide range of tissue sources and regenerative applications, the clinical application of these materials clearly lags far behind that of decellularized ECM grafts and sheets. Thus, the greatest potential for novel clinical applications of decellularized ECM biomaterials lies in the development of powders, hydrogels, and other forms of decellularized ECM.

1.4 Understanding the Pro-Repair Mechanisms of Decellularized ECM Biomaterials

1.4.1 Overview of Decellularized ECM Biocompatibility and Bioactivity

Decellularized ECM biomaterials are biocompatible owing to the removal of immunogenic cellular debris from the ECM scaffold; it is for this reason that different decellularization techniques have been so thoroughly explored, as described in section 1.2. It is essential to achieve near complete removal of cellular debris and nuclear residue to prevent a negative immune response upon injection or implantation of decellularized ECM biomaterials. However, the need for thorough decellularization must be balanced

with the maintenance of bioactive components within the ECM, which can be stripped from the scaffold if decellularization conditions are too harsh.[11] These bioactive components include structural proteins, glycosaminoglycans, growth factors, cytokines and chemokines, and extracellular vesicles.[27] Importantly, many of these bioactive components are released as degradation products through cell-mediated remodeling of the ECM after implantation or injection; thus, the degradation of decellularized ECM is critical in both the biocompatibility and bioactivity of these materials.[28]

Decellularized ECM materials can mediate tissue regeneration and repair through both structural and biochemical cues. Proteins such as collagens, laminins, fibronectin, and elastin are integral to ECM structure and potentiate cellular adhesion and migration. The biochemical cues, often released as the ECM scaffold is broken down by invading cells, are vital for the pro-repair mechanism of decellularized ECM biomaterials and can influence cellular proliferation and differentiation, ECM remodeling, neovascularization, neural regeneration, and immune modulation.[5]

1.4.2 Cellular Proliferation and Differentiation

Decellularized ECM biomaterials have demonstrated marked effects on cellular proliferation and differentiation in a variety of applications both clinically and preclinically. One of the most prolific applications of decellularized ECM clinically – patches for wound care – demonstrates that these biomaterials encourage cellular attachment and ingrowth followed by proliferation and differentiation to result in tissue regrowth in ECM scaffolds.[29] Specifically, structural proteins such as collagens, laminins, elastin, and fibrillin encourage migration and proliferation of cells to form granulation tissue, and growth factors along with other bioactive ECM components contribute to proliferation and

differentiation of keratinocytes and fibroblasts.[29] In another application, decellularized liver ECM scaffolds promote proliferation and differentiation of both hepatic progenitor cells[30] and cholangiocytes,[31] indicating their efficacy in liver regeneration.

These materials have additionally been shown to improve regeneration of cardiac and skeletal muscle in a variety of injury and disease models. Cardiac tissue derived ECM hydrogels supported increased cardiomyocyte proliferation and hypertrophy in rat models of myocardial infarction[32] and right heart failure.[33] Both porcine dermis and porcine urinary bladder matrix hydrogels demonstrated improvement in myogenesis (skeletal muscle proliferation and differentiation) in a rat model of abdominal wall defect.[34] Skeletal muscle hydrogels potentiated muscle progenitor infiltration and muscle cell proliferation in both a model of hindlimb ischemia in the rat[35] as well as a model of volumetric muscle loss in the mouse.[36]

Preclinical investigations of decellularized ECM biomaterials have demonstrated improvements in cellular proliferation and differentiation for diverse cell types in a wide variety of applications. Beyond wound healing and soft tissue defect repair, which have been extensively explored clinically, there is considerable potential for clinical translation of decellularized ECM hydrogels based on their support of cell growth shown *in vivo.*

1.4.3 Fibrosis and ECM Remodeling

Another hallmark mechanism of decellularized ECM biomaterials is their influence on ECM remodeling and reduction of pathological fibrosis. This is evident in the wound healing application of decellularized ECM sheets and grafts, in which these materials interact with fibroblasts and immune populations to stimulate remodeling of the native ECM and complete the wound healing process.[17] Furthermore, decellularized ECM

hydrogels have shown reduction in pathological fibrosis in a variety of applications, including right heart failure,[33] myocardial infarction,[37] pelvic floor muscle injury,[38] pulmonary fibrosis,[39], and liver fibrosis.[40]

1.4.4 Vascularization

Decellularized ECM biomaterials have demonstrated a remarkable potentiation of neovascularization across a variety of different injury models and applications. Clinically, decellularized ECM sheets used as skin grafts for healing of chronic wounds and burns show significant improvement in development of microvasculature after implantation.[41] Improvement in vascularization of the injury site contributes greatly to the wound healing and tissue repair process. Decellularized ECM materials have also been used extensively in great vessel repair and vascular reconstruction in the heart clinically, as ECM scaffolds and grafts promote recellularization and healthy vascular growth.[18]

In preclinical research, decellularized ECM has been deployed as a hydrogel in a variety of applications and has shown a consistent upregulation of microvasculature development across different models. Injectable ECM hydrogels have induced arteriogenesis and neovascularization in models of peripheral artery disease,[42] right heart failure,[33] and myocardial infarction.[43] Decellularized ECM has even been developed as an infusible form, by removing high molecular weight proteins through a combination of centrifugation and filtration. When applied in a preclinical model of myocardial infarction, the infusible ECM demonstrated localization to damaged vasculature within the infarcted region of the heart and promoted neovascularization within the heart.[44] Similar improvements in vasculature were seen after administration of infusible ECM in a model of traumatic brain injury.[45]

1.4.5 Neural Regeneration

Decellularized ECM sheets and grafts are already used clinically for peripheral nerve repair (AxoGuard®) and dural repair and reconstruction (Lyoplant® and Tutoplast®). Preclinically, acellular nerve grafts have demonstrated improvements in axonal regeneration in a model of peripheral nerve injury.[46] Another group showed that decellularized spinal cord grafts enhanced proliferation and differentiation of neuronal progenitors and neuronal tissue repair in a model of spinal cord injury.[47] Additionally, engineered neural tissue has been created utilizing decellularized tissue from bone, liver, and small intestinal submucosa sources, and improvements in Schwann cell activity, dorsal root ganglia neurite extension, and axonal regeneration were observed. [48] While neural regeneration is a less explored mechanism of decellularized ECM hydrogels, it is evident that there is significant potential that remains to be explored.

1.4.6 Immune Modulation

The immunomodulatory properties of decellularized ECM biomaterials are perhaps the most conserved mechanism across their various applications in both preclinical and clinical studies, and immune modulation contributes to many other mechanisms already mentioned, such as cellular recruitment, ECM remodeling, and vascularization. This immunomodulatory mechanism may be broken down according to the response of different immune populations (B and T cells, macrophages, granulocytes, etc.) to decellularized ECM biomaterials.

The macrophage response is among the most well-documented and robust mechanisms of the immune response to decellularized ECM biomaterials. Macrophages are broadly considered to display one of two phenotypes: M1, a pro-inflammatory

phenotype, or M2, an anti-inflammatory and pro-regenerative phenotype.[49] They are classified as such based on the cytokines and chemokines that these macrophages release and respond to, as well as the downstream pathways that they influence. M1 macrophages are typically associated with a sustained inflammation response that can lead to pathological fibrosis, while M2 macrophages can attenuate inflammation, potentiate ECM remodeling, and induce cellular proliferation and differentiation.[50] Many of the clinically used decellularized ECM biomaterials report a high M2:M1 ratio, and it is known that macrophages are critical for the degradation and remodeling of decellularized ECM scaffolds.[51] This remodeling of the decellularized ECM upon implantation or injection enables the release of bioactive degradation products, which, as previously discussed, are critical for the pro-repair effects of these biomaterials. During macrophage mediated remodeling of the ECM, these cells facilitate a strong chemotaxis response, which in turn encourages cellular migration into the decellularized ECM scaffold, neovascularization, and subsequent tissue growth and repair.[50] This mechanism has been frequently validated in preclinical studies, which show elevated M2 macrophage activity following treatment with decellularized ECM biomaterials in models of right heart failure,[33] abdominal wall defect,[51] xenotransplantation,[52] and surgical mesh implantation.[53] It is evident that decellularized ECM biomaterials are immunomodulatory, and macrophage activity is critical in their application for tissue regeneration.

The T cell response is another critical mechanism by which decellularized ECM biomaterials can elicit pro-repair effects. Similar to their effect on macrophages, ECM biomaterials can affect helper ($CD4^+$) T cell polarization. Helper T cells may be broken down into a few broad populations – again defined by their association with different

cytokines and chemokines and influence on downstream pathways – including Th1 and Th17, which are pro-inflammatory, and Th2, which are anti-inflammatory and pro-regenerative.[54] Th1 and Th17 populations contribute to an overall inflammatory response in part by polarizing naïve macrophages to an M1 phenotype, while Th2 attenuate sustained inflammation and support M2 macrophages in promoting vascularization and tissue repair.[53] Tregs are another population of $CD4^+$ T cells which are integral in the pro-repair immune response, reducing inflammation and fibrosis while promoting a pro-regenerative microenvironment.[55] In preclinical studies, decellularized ECM biomaterials have demonstrated upregulation of Tregs in a model of pelvic floor injury,[38] and modulation of T cell activity in a model of traumatic brain injury,[45] and a Th2 mediated response to xenogeneic ECM graft implantation.[56] Additionally, the cytotoxic ($CD8^+$) T cell response is important in application of decellularized ECM, for insufficient removal of antigenic material from ECM scaffolds can activate cytotoxic T cells and result in a negative immunogenic response.[8] Overall, the T cell response to decellularized ECM biomaterials remains less thoroughly explored than the macrophage response, yet several studies indicate that it may be critical for the pro-repair effects of these materials.

Other immune populations have been much less thoroughly explored in their response to decellularized ECM biomaterials. One study found a robust B cell response both locally and systemically following treatment with decellularized ECM in a model of volumetric muscle loss.[57] Another study investigated the immunomodulatory contribution of mast cells, specifically in regards to macrophage polarization, after subcutaneous implantation of decellularized ECM scaffolds.[58] Overall, it is evident that ECM biomaterials can have diverse and robust immunomodulatory effects on tissue, which are integral to

their tissue regenerative properties and must be further investigated to fully elucidate the mechanism of repair.

1.5 Conclusion: Expanding Translation of Decellularized ECM Biomaterials

Decellularized ECM biomaterials have been developed in a wide range of forms – sheets, grafts, powders, hydrogels, and infusible materials – utilizing a variety of decellularization techniques and downstream processing methods. Clinically, decellularized ECM sheets and grafts have been the most extensively explored and have yielded promising results in applications of wound care, soft tissue repair and reconstruction, and other indications. ECM biomaterials that are FDA approved and clinically used employ a combinatorial decellularization approach, typically combining physical decellularization (tissue isolation and mechanical agitation), detergents (most commonly SDS and Triton X-100), and occasionally enzymes (DNAse, trypsin). To advance the clinical application of ECM biomaterials, we may utilize proven and accepted decellularization techniques in combination with novel processing methods to develop more versatile applications for decellularized ECM, which demonstrates remarkable tissue regenerative abilities.

Preclinical models have established the key mechanisms by which these materials facilitate regeneration – cellular proliferation and differentiation, ECM remodeling, vascularization, and immune modulation. Additionally, the usage of decellularized ECM hydrogels has been extensively explored in preclinical models, presenting the most viable future direction for clinical translation of ECM biomaterials. Taking into account FDA-approved decellularization techniques, established mechanisms of repair, and promising

preclinical studies will facilitate the successful translation of decellularized ECM biomaterials in novel approaches and applications.

1.6 Thesis Outline

This thesis is broken into 4 subsequent chapters.

Chapter 2 describes the novel implementation of a porcine skeletal muscle derived ECM (SKM) hydrogel, previously utilized in preclinical models of peripheral artery disease and pelvic floor muscle injury, in a model of tongue fibrosis. It includes the dose optimization for injection of the SKM hydrogel in the scar region following a partial glossectomy injury model. This chapter then demonstrates the dose-dependent effect of SKM on scar reduction. It also shows an improvement in muscle regeneration, a transient upregulation in microvasculature development, immunomodulatory response, and recruitment of pro-repair fibroadipogenic progenitors following injection of SKM. This chapter provides evidence that the SKM hydrogel is a promising regenerative therapeutic that may be applied in the underserved clinical application of tongue fibrosis and dysphagia following oropharyngeal cancer treatment.

Chapter 3 discusses the optimization of a preclinical model of stress urinary incontinence, which is a prevalent and underserved pelvic floor disorder primarily affecting women undergoing vaginal delivery. This chapter demonstrates the use of a functional outcome of urinary incontinence to compare several different preclinical models previously established and identifies the model that most represents clinical outcomes. It then discusses the novel application of the SKM hydrogel for external urethral sphincter regeneration in a preclinical model of stress urinary incontinence. This chapter overviews the histomorphological and functional outcomes of SKM injection in this model and

provides future directions for developing ECM therapeutics to treat stress urinary incontinence.

Chapter 4 presents the fabrication and characterization of the first reported porcine vaginal tissue derived ECM (vECM) hydrogel, which was developed for application in a preclinical model of genitourinary syndrome of menopause. It discusses the dose-dependent retention of vECM following intravaginal administration as well as the dose-dependent regenerative effect of vECM in vaginal epithelial and smooth muscle repair. This chapter provides characterization of vaginal epithelial phenotype following vECM treatment as well as investigation of smooth muscle cell proliferation. It further provides evidence that vECM, when administered intravaginally, recruits immune cells to the vaginal lumen and is trafficked from the lumen to subepithelial and muscularis tissues of the vagina. This chapter concludes with future directions for investigation and application of this novel and highly translatable ECM biomaterial.

The final chapter provides a summary of the results of this dissertation and discusses the broader implications for the tissue engineering field. Finally, the chapter discusses future studies and opportunities for design of translational and regenerative decellularized ECM biomaterials.

Chapter 2: Immunomodulatory Extracellular Matrix Hydrogel Induces Tissue Regeneration in a Model of Partial Glossectomy

2.1 Introduction

Dysphagia is a debilitating condition defined broadly as difficulty swallowing. Dysphagia may result from atrophy, denervation, or fibrosis of the tongue muscles.[59] While this condition is commonly implicated in aging or neurological disorders, another patient population of interest is those recovering from head and neck cancer.[60] Treatment of these cancers typically involves surgical removal of the tumor followed by radiation with or without chemotherapy. Dysphagia is a common sequela of treatment – affecting at least half of oropharyngeal cancer patients – and demonstrates a particularly high incidence following treatment of tongue cancer, which is the most frequent intraoral head and neck cancer.[61,62] Dysphagia is a morbid condition that severely affects quality of life and potentially leads to feeding tube dependence, aspiration, malnutrition, and even death.[62,63] Current standard of care for oropharyngeal dysphagia is limited to rehabilitative strategies such as swallow therapy and lingual muscle exercises. However, these approaches do not provide long-term improvement in swallowing and tongue strength, and they do not reverse the tissue-level pathology by improving muscle regeneration and reducing scar tissue formation.[64] About 18,000 cases of tongue cancer are diagnosed annually in the US, with a 5-year survival rate of approximately 70%; as such, there is a growing patient population in dire need of improved treatment options following cancer treatment to prevent or reverse tongue fibrosis and atrophy and address the underlying pathophysiology of oropharyngeal dysphagia to not only prolong life but improve its quality.

Considering these deficiencies in treatment, a number of investigative cell-based therapies that seek to regenerate tongue muscle or provide structural augmentation to improve tongue function have emerged. While preclinical investigation of allogeneic mesenchymal stem cell injection in an athymic rat model has demonstrated some potential,[65,66] the manufacturing, cost, and difficulties associated with a living stem cell product pose translational challenges. Additionally, autologous muscle-derived cell therapy demonstrated safety but lacked efficacy after 2 years in a Phase 1 trial.[67] Overall, the current body of research demonstrates a continued need for an accessible and minimally invasive therapeutic that can induce tissue regeneration to reduce scar formation and muscle atrophy to improve muscle repair and maintain muscle bulk.

The use of decellularized extracellular matrix (ECM) hydrogels that induce immune modulation, cellular recruitment and differentiation, neovascularization, and ECM remodeling has been explored as a therapeutic in numerous disease phenotypes.[25] The ECM is a complex network of proteins and polysaccharides vital for structural support and cell signaling; when a whole tissue is decellularized, the ECM remains as an acellular biomaterial with tissue regenerative properties.[25] Additionally, due to their thermoresponsive properties, ECM hydrogels, formed via partial enzymatic digestion of decellularized ECM, can be delivered minimally invasively via injection, and after exposure to physiologic conditions, the liquid forms a scaffold comprised of a nanofibrous ECM network.[68] With sufficient decellularization, the acellular xenogeneic ECM hydrogels are biocompatible and have been utilized in large[69,70] and small animal models,[71] as well as a human Phase 1 clinical trial that assessed safety and feasibility for intervention in subacute and chronic myocardial infarction.[26] We have previously demonstrated that a

decellularized porcine skeletal muscle ECM hydrogel (SKM) increased vascularization, enhanced the recruitment and differentiation of muscle progenitors, and reduced muscle atrophy and cell death in an ischemic injury model.[35,42,68] SKM has further been shown to prevent skeletal muscle atrophy and mitigate fibrotic degeneration, as well as modulate the immune response after mechanical muscle injury in pelvic floor muscles.[38]

In the present study, we investigated the therapeutic efficacy and potential mechanisms of action of SKM in a preclinical animal model of partial glossectomy. We observed that SKM reduces scar formation and improves fiber area in a rat tongue partial glossectomy model. We further demonstrated that SKM modulates the immune response and upregulates genes related to angiogenesis. Overall, we found that SKM injection is a promising treatment in a preclinical model of partial glossectomy that warrants further investigation as a potential minimally invasive acellular therapeutic for oropharyngeal dysphagia.

2.2 Results

2.2.1 Determining optimal injection volume of SKM hydrogel

Acellular biomaterial therapeutics have not been previously investigated for oropharyngeal dysphagia in a pre-clinical animal model, so we first conducted a study to determine the optimal injection volume of SKM. A rat partial glossectomy injury model, previously developed to mimic the fibrosis and muscle atrophy that follows head and neck cancer treatment, was used.[66] The study design (Figure 2.1A) included injection volumes ranging from 50 to 300 µL.

Based on previous ECM hydrogel studies, greater material retention led to improved repair with a typical degradation time of approximately 3 weeks; thus, it was

desirable to see high material retention in the tissue at 1 week post-injection to enable prolonged pro-regenerative cues and sufficient repair.[35,72] Representative images of injection boluses are shown for all SKM dosages (Figure 2.1B-E), demonstrating increased material retention and spread through the tongue with higher injection volumes. Therefore, we found that 200 and 300 µL injection volumes were suitable for further investigation.

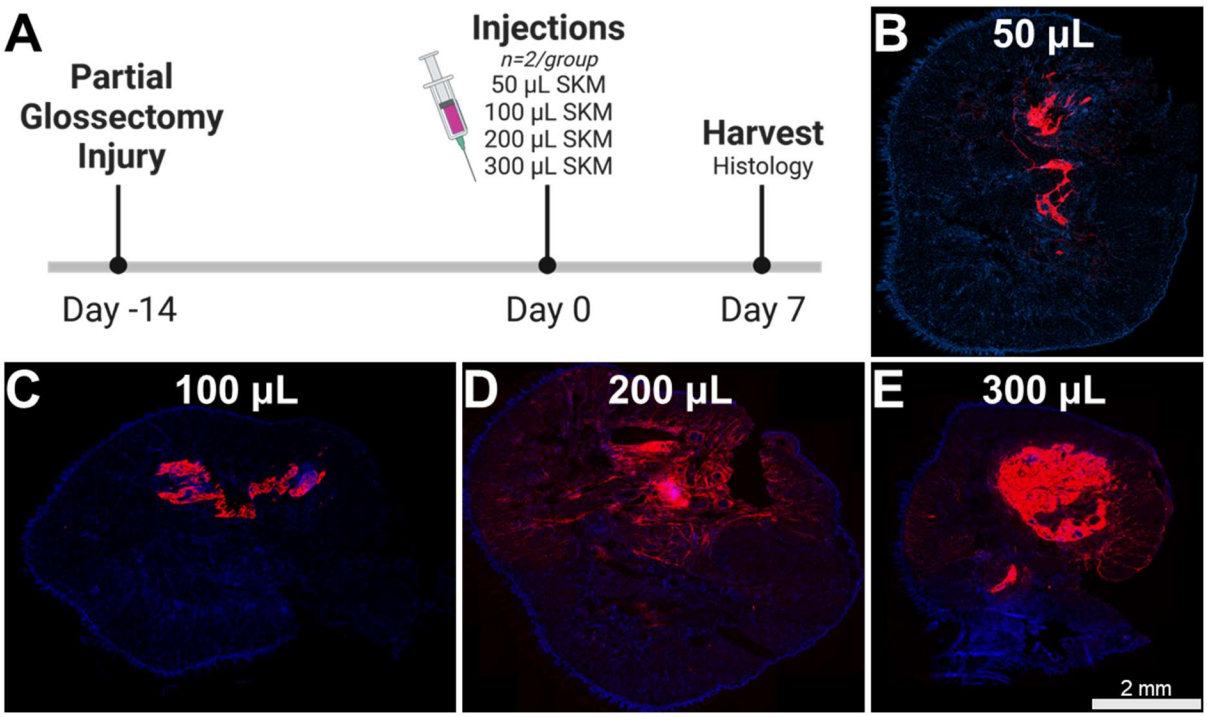


Figure 2.1 SKM hydrogel injection volume optimization after tongue partial glossectomy injury.

(A) A range of SKM volumes were injected 2 weeks after partial glossectomy injury, and tissues were harvested 1 week post-injection. Representative fluorescent images show pre-labeled SKM material in red against a DAPI counterstain in blue to indicate cell nuclei. SKM material spread and retention in the target tissue is shown for a range of injection volumes including 50 (B), 100 (C), 200 (D), and 300 µL (C). Scale bar: 2 mm.

2.2.2 Higher volume of SKM hydrogel reduces scar formation in a rat model of partial glossectomy

To investigate therapeutic potential of SKM hydrogel, the chosen injection volumes – 200 and 300 µL – were injected 2 weeks following partial glossectomy injury as low or high dose therapeutic options (Figure 2.2A). The experimental control group received a saline injection at the same time point. Whole tongues were harvested 4 weeks after injection for assessment of histomorphological properties. First, we investigated whether SKM decreased scar formation in this injury model, which is important as scarring contributes to dysphagia following surgical resection of head and neck cancers. Representative brightfield images of tongue cross-sections from the treatment groups are shown in Figure 2.2B-D. As shown in Figure 2.2E, the scar area fraction was significantly reduced in the higher dose SKM group compared to both low dose SKM ($P=0.005$) and saline ($P=0.02$) groups.

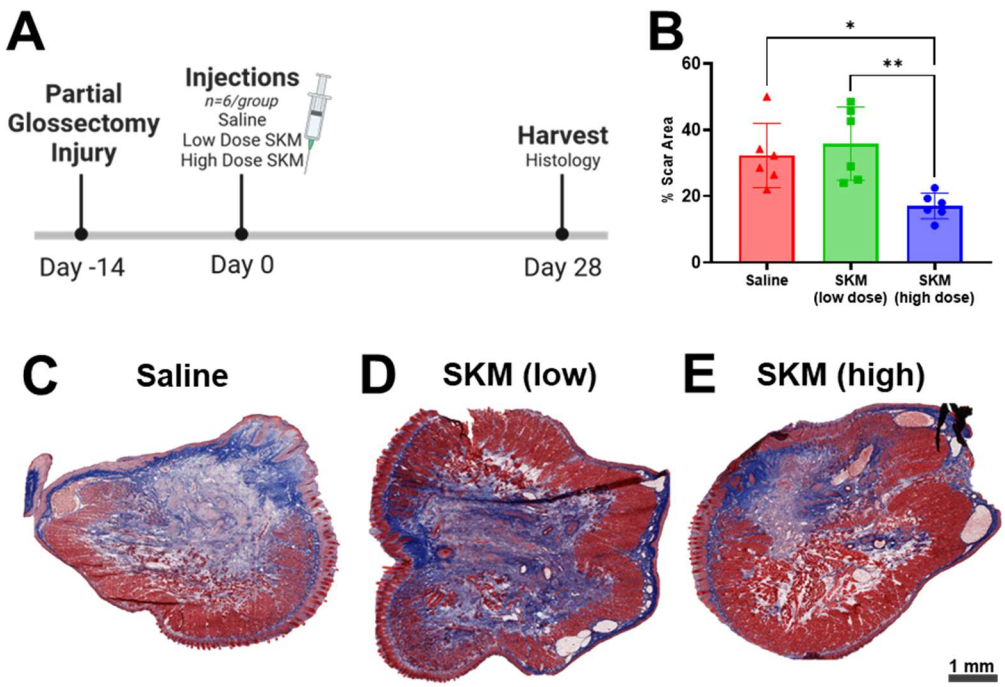


Figure 2.2 SKM injection after partial glossectomy injury reduces scar formation.

(A) Timeline of study to assess therapeutic potential of two doses of SKM hydrogel injection. Tissues were harvested 4 weeks after injection for assessment of scar formation via Masson's Trichrome stain, in which collagen is blue, denoting the scar region, and muscle fibers are red. B) High dose SKM group significantly reduced scar formation compared to both the low dose SKM and saline injected groups. Treatment groups were compared using one-way ANOVA with Tukey multiple comparisons test (*$p<0.05$; **$p<0.01$). Representative images for the saline (C), low dose SKM (D), and high dose SKM (E) injection treatment groups are shown. Scar area was quantified and normalized to the total cross-sectional area for each tissue section including scar tissue, and values for all sections including the scar were averaged for each animal. n=5-6 animals analyzed/group.

2.2.3 SKM hydrogel improves muscle regeneration within scar region

For subsequent evaluation, only the higher dose SKM group was used as the lower dose SKM injection did not demonstrate reduction of scar formation. Short axis cross-sections of tongue specimens were stained with antibodies against collagen I, sarcolemma (α-sarcoglycan), and a nuclear stain (DAPI). Representative fluorescent images are shown in Figure 3A-B. A higher magnification image demonstrates the presence of skeletal

muscle fibers (red) inside the scar area (green, Figure 3C-D). To assess the effect of SKM injection on muscle regeneration, we quantified fiber number and fiber cross-sectional area inside the scar region, as defined by the area with collagen staining. There were no quantitative differences in myofiber density in the scar between the groups (Figure 2.3E, P=0.86), however, fiber cross-sectional area was significantly greater in the high dose SKM compared to saline group (Figure 2.3F, $p<0.0001$). Although, both SKM and saline demonstrated smaller fiber area compared to age-matched healthy controls (Figure 2.4C). The proportion of centrally nucleated fibers was quantified to determine if the muscle was actively regenerating; there was no difference between SKM and saline treated animals, indicating that muscle regeneration was not ongoing and fiber area measurements were reflective of the tissue at homeostasis. This was supported by comparison to central nucleation in healthy tissue (Figure 2.4D), which showed no difference in proportion of centralized nuclei among SKM, saline, and healthy groups, indicating that both injected groups had returned to baseline and were not undergoing active regeneration.

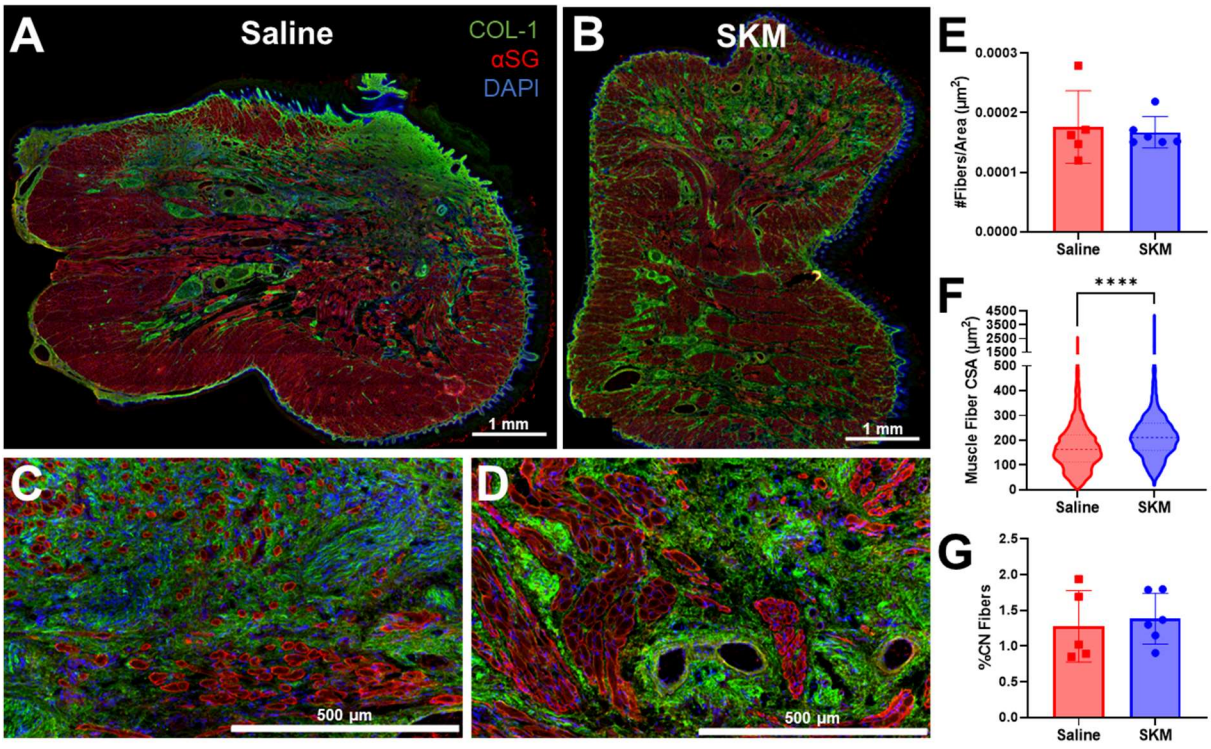


Figure 2.3 SKM Injection improves muscle regeneration within scar area.

Tongue sections underwent immunohistochemical staining to denote the scar (collagen I, green), myofibers (α-sarcoglycan, red), and nuclei (DAPI, blue). Representative fluorescent images are shown for saline (A) and SKM (B) injection groups (Scale bar: 1 mm). Higher magnification saline (C) and SKM (D) representative images demonstrated differences in fiber size and organization within the region of scar. Scale bar: 500 µm. (E) Fiber counts were normalized to scar area, showing no significant difference between treatment groups. (F) Muscle fiber area distributions are displayed as violin plots, with the dashed line indicating the median. Using a Mann-Whitney test, SKM demonstrated significantly increased fiber areas compared to saline injection (****$p<0.0001$). (G) Within the scar area, proportion of fibers with centralized nuclei did not differ between groups. n=5-6 animals analyzed per group.

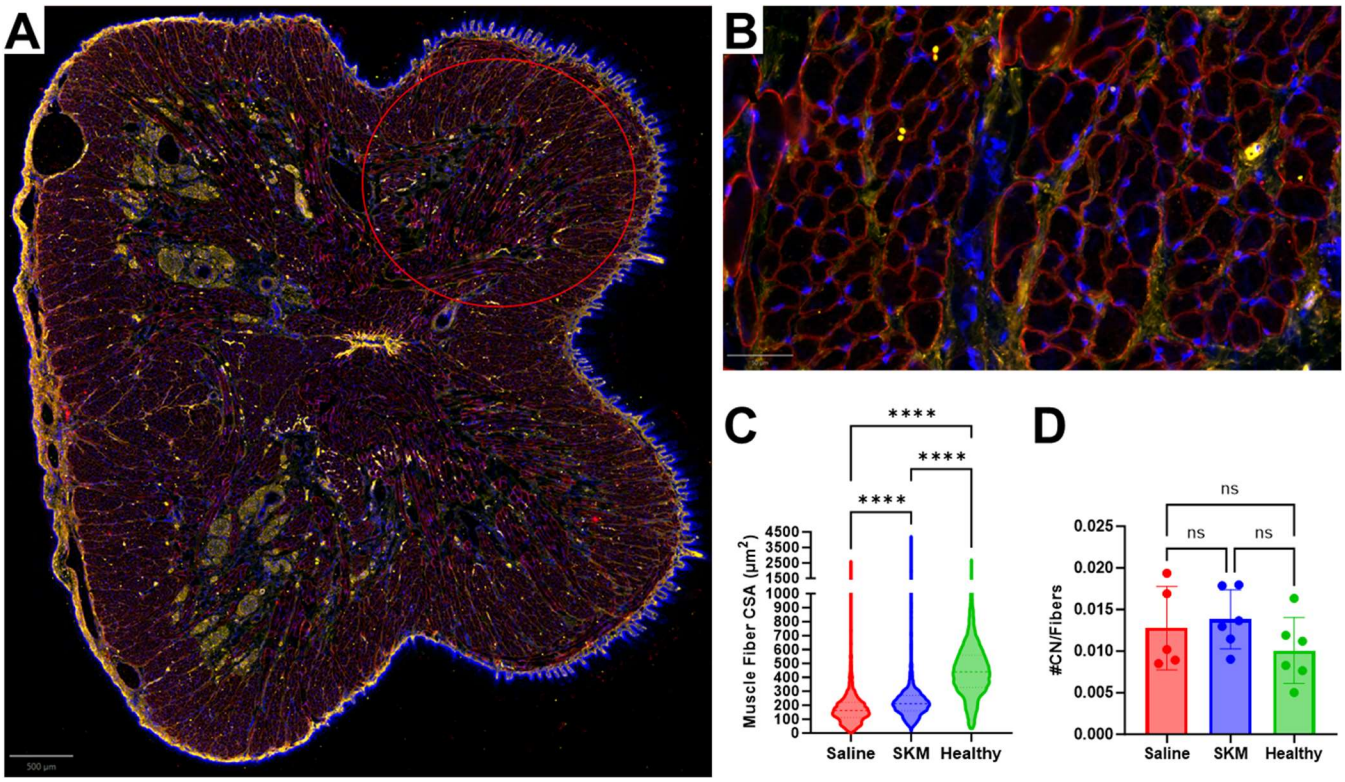


Figure 2.4 Muscle fibers within scar of SKM and saline injected animals are smaller than healthy, but there is no difference in proportion of centralized nuclei.

Age-matched healthy controls (n=6) were used to investigate the expected muscle fiber area and proportion of centralized nuclei. (A) Tissue section location and region of interest (red circle) were selected to match the region of scar in injured animals. (B) Tissue sections were stained against α-sarcoglycan (red), collagen (green), and nuclei (blue). (C) Healthy muscle fiber area distribution was compared to fiber area within the scar region of saline and SKM injected animals (shown previously), and healthy demonstrated significantly higher muscle fiber area compared to both groups. (D) Similarly, proportion of centralized nuclei was compared, but no difference was observed between the groups. Scale bar: 500 μm (A), 50 μm (B).

2.2.4 SKM hydrogel upregulates pro-regenerative immune response, myogenic response, and angiogenic signaling

Having demonstrated significant histomorphological improvements with SKM injection in this model, we then conducted a gene expression study to investigate potential mechanisms driving these changes. Two weeks following partial glossectomy injury, SKM

or saline were injected into the site of injury. Additionally, non-injected injured animals were used. To capture physiologically relevant timepoints for early changes in the immune response, myogenesis, and ECM remodeling, tissues were harvested for RNA isolation at 3 and 7 days post-injection (Figure 2.5A). A custom NanoString multiplex gene expression panel of 145 genes for rat skeletal muscle, which included pathways of interest such as the immune response, myogenesis, muscle anabolism/catabolism, angiogenesis, and ECM remodeling, was used to characterize the tissue response to injury with and without SKM injection (Table 2.1). The significantly differentially expressed genes for comparisons between SKM and either saline or no injection groups are shown for days 3 and 7 post-injection in Figure 2.5B-E.

At day 3 post-injection, SKM induced dramatic differential gene expression as compared to non-injected controls. Genes involved in skeletal muscle structure and contraction were downregulated (*Acta1, Actn2, Des, Mybpc1, Mybpc2, Myf6, Myh1, Mylk2, Sln, Ttn3, Ttn*), as were genes related to muscle catabolism and cellular survival (*Akt2, Ccn4, Fbxo32, Nfkbia, Nol3, Rps6Ka1, Trim63*). Genes involved in ECM deposition and fibrosis (*Ctgf, Smad3, Timp1, Tgfb)* were upregulated, while some angiogenic growth factors (*Fgf2, Vegfb*). Several pro-inflammatory cytokines and chemokines (*Il1b, Il6, Il12b, Ccl2, Ccl3, Ccl4),* which are involved in early stage of injury response and facilitate recruitment of macrophages and neutrophils [73,74], were upregulated. SKM further demonstrated increased expression of *Irf4* and *Irf5* (transcription factors of M2 and M1 macrophages, respectively), *Il10ra* (implicated in the transition of macrophages from the M1 to M2 phenotype), *Nkg7* (T cell marker), and *Cxcl1* (recruits neutrophils and M2 macrophages)[75]. SKM injection also led to upregulation of *Pdgrfralpha,* a marker for

fibroadipogenic progenitors (FAPs), in addition to the cytokines *Il15* and *Il33*. *Il15* is known to be a key regulator of FAPs, inhibiting fatty infiltration and promoting muscle regeneration, while *Il33* is involved in recruitment of T regulatory (Treg) cells, which are similarly important in regulation of FAPs to promote a muscle repair phenotype[76,77].

At day 7 post-injection, the differential gene expression between SKM and no injection groups altered significantly. Relative to day 3, fewer genes involved in muscle structure were downregulated (*Mstn, Myh1, Mypbc2, Tcap, Ttn)*, and other genes involved in muscle structure and myogenesis were indeed upregulated (*Hgf, Myh3, Myh7, Tnnt1*). At this timepoint, there was a general shift in ECM expression towards remodeling through the downregulation of MMP inhibitors (*Timp3, Timp4*) and the upregulation of MMPs (*Mmp2, Mmp9, Mmp12, Mmp14).* There was persistent upregulation of some pro-inflammatory cytokines and chemokines (*Ccr2, Ccl2, Il12b*) and M1 macrophage transcription factors (*Irf5, Stat1*). Additionally, T cell marker *Nkg7* and, in particular, the Th2 marker *Gata3*, were both upregulated at this time point in the SKM group. Macrophage marker *Adgr1* was enriched, and several pro-regenerative cytokines (*Il10, Il10ra, Il15*) demonstrated increased expression at this timepoint as well.

The significant differentially expressed genes between SKM and saline animals are displayed in a volcano plot for days 3 and 7 post-injection alongside their associated pathways in Figures 4D and E, respectively. At day 3 post-injection, SKM led to upregulation of *Adgr1*, a macrophage marker, as well as *Pparg*, a macrophage transcriptional marker of pro-repair macrophages.[78] We further observed SKM immunomodulation through the downregulation of *Cxcr2,* associated with neutrophils and a pro-inflammatory response, and upregulation of pro-regenerative cytokine *Il33* with

respect to saline. SKM also resulted in upregulation of *Ctgf*, which is known for a pro-reparative role in wound healing when expressed transiently in early injury response.[79] Compared to saline, SKM group had higher expression of *Timp4*, a matrix metalloproteinase inhibitor that regulates ECM remodeling as well as angiogenesis.[80] At day 7 post-injection, SKM modulation of *Adgr1*, *Cxcr2,* and *Il33* expression was maintained with respect to saline. SKM induced downregulation of *Nfkbia*, which is an inhibitor of the NF-κB pathway. Finally, SKM increased expression of *Vegfr2* and downregulated *Thsb1*, indicating an overall increase in angiogenic signaling.

To confirm and further assess transcriptomic changes at these early timepoints, RNA from tissues collected 3 and 7 days post-injection for SKM, saline, and non-injected groups underwent bulk RNA sequencing. Differential expression at 3 (Figure 2.6A) and 7 (Figure 2.6B) days post-injection for SKM and non-injected groups based on this analysis is shown in volcano plots, alongside gene ontology for up- and downregulated genes at each timepoint in Figure 2.6. At 3 days post-injection, SKM upregulated pathways were associated with muscle development and regeneration as well as blood circulation and vasculature development. Downregulated pathways of note included maintenance of keratinized epithelium (keratinocyte development and differentiation, formation of the cornified epithelium) and regulation of immune response (cytokine production, mast cell degranulation). Conversely, at day 7 post-injection, upregulated pathways are almost entirely related to immune activation and regulation.

Differential expression between SKM and saline was also evaluated at these timepoints. As fewer differentially expressed genes, genes were assessed individually rather than utilizing GO analysis, At both day 3 (Figure 2.6C) and day 7 (Figure 2.6C)

post-injection, these genes were predominately associated with the immune response – particularly upregulation of immune cell infiltration (*Ccr9, Ddx60, Pla2g2d, Pdia5*), Treg response (*Ly49si4, Rsad2, Slc13a3, Xcr1*), macrophage response (*Adgre1, Pdia5, Slc13a3*), regulation of the immune response (*Klf2, Lgals9*), and other immune related or interferon induced genes (*Jchain, RGD1563231, Fclr2, Mx2, C6, Cmpk2, Gbp1, Gbp6-ps2*) as well as downregulation of pro-inflammatory expression (*Defb4, Rpph1, Slc15a1*) and genes that inhibit T-cell and macrophage activity (*Klk12, Vsig10l, Tmem125*). We additionally observed upregulation of genes supporting myoblast differentiation and regeneration (*Per1, Oas1f, Oas2*) and proliferation (*Egr1*). Finally, genes involved in keratinization and cornified envelop development were downregulated (*Lce3d, Loricrin*).

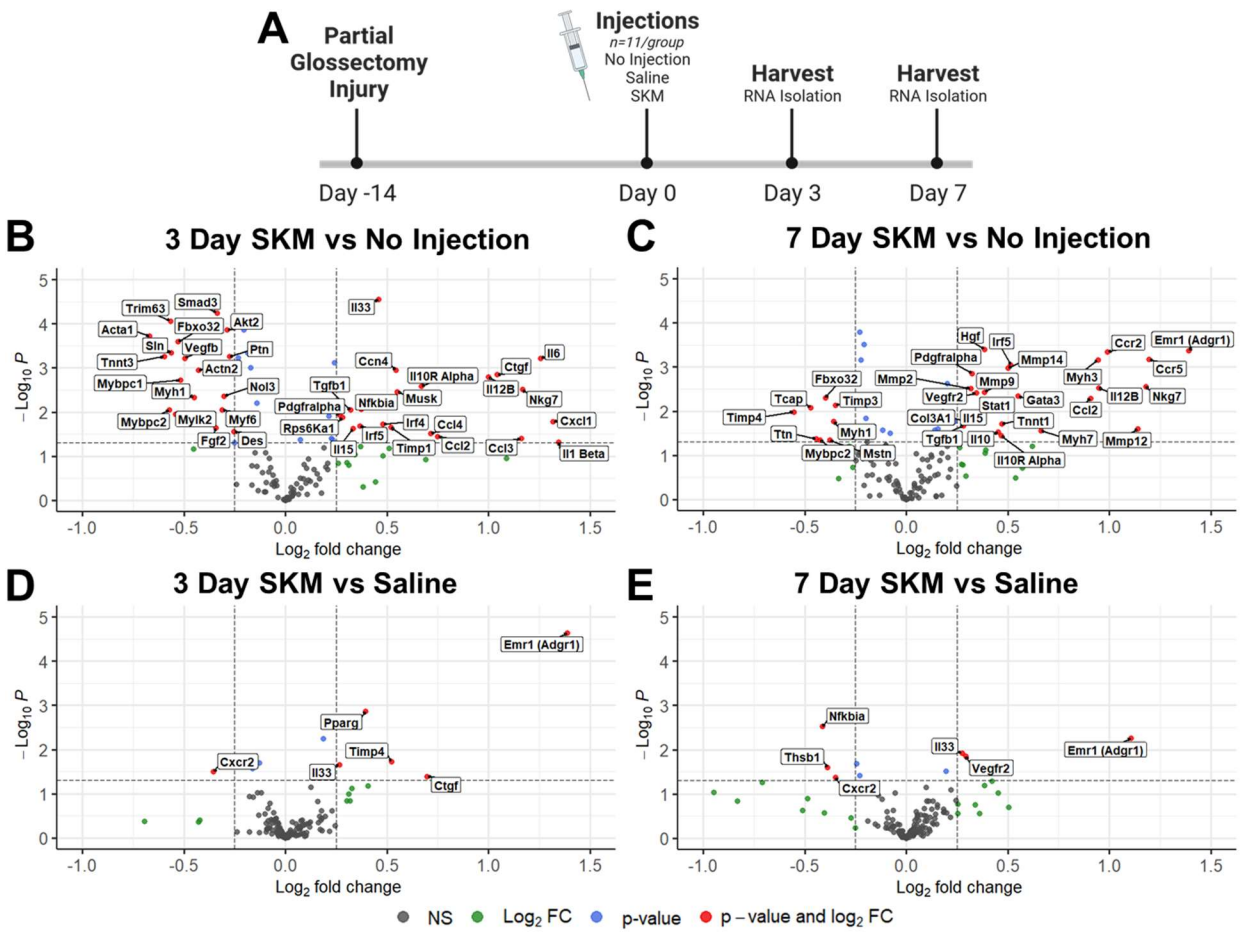


Figure 2.5 SKM injections induce significant differential transcriptomic expression when compared to both no injection and saline control groups.

(A) Experimental timeline for gene expression study using a custom NanoString multiplex gene expression panel. Differentially expressed genes between SKM and either no injection (B-C) or saline controls (D-E) are displayed in a volcano plot for both 3 and 7 day timepoints. n=11 animals analyzed per group.

Table 2.1 List of genes included in custom NanoString panel.

Category	Gene	Accession	Classification
Immune response Pro-inflammatory	Il1b	NM_031512.1	Cytokine
	Il6	NM_053836.1	Cytokine
	Tnf	NM_012675.2	Cytokine
	Ifng	NM_138880.2	Cytokine
	Il12b	NM_022611.1	Cytokine
	Il2	NM_022611.1	Cytokine
	Tnfrsf1a	NM_013091.1	Receptor/growth factor
	Ccl2	NM_031530.1	Chemokine
	Ccl3	NM_013025.2	Chemokine
	Ccl4	NM_053858.1	Chemokine
	Ccr2	NM_021866.1	Chemokine
	Cxcl1	NM_053960.3	Chemokine
	Cxcl5	NM_053304.1	Chemokine
	Cxcr2	NM_017183.1	Chemokine
	Nos2	NM_012611.2	M1
	Tbx21	NM_001271120.1	Th1
	Il23a	NM_130410.2	Cytokine
	Stat1	NM_032612.2	M1 transcription factor
	Irf5	NM_001106586.1	M1 transcription factor
	Adgre1	NM_001007557.1	Macrophages
	Myd88	NM_198130.1	Monocytes
	Nfkb1	XM_342346.3	Transcription factor
	Nkg7	NM_133540.1	T cells
	Mmp12	NM_053963.2	Metalloelastase
Immune response Pro-regenerative (Anti-inflammatory)	Il33	NM_001014166.1	Cytokine
	Il13	NM_053828.1	Cytokine
	Il4	NM_201270.1	Cytokine
	Il5	NM_021834.1	Cytokine
	Il15	XM_008772363.2	Cytokine
	Il17	NM_001106897.1	Cytokine
	Il10	NM_012854.2	Cytokine
	Il10ra	NM_057193.2	Cytokine/Receptor
	Igf1	NM_001082477.2	Growth factor
	Igf1r	NM_052807.2	Growth factor/Receptor
	Ccr5	NM_053960.3	Chemokine
	Arg1	NM_017134.2	M2
	Gata3	NM_133293.1	Th2
	Foxp3	NM_001108250.1	T regulatory cells
	Stat6	NM_001044250.1	M2 transcription factor
	Irf4	NM_001106108.1	M2 transcription factor

Table 2.1 List of genes included in custom NanoString panel (continued).

Myogenesis	Pax7	NM_001191984.1	Quiescent and activated muscle stem cells
	Myod1	NM_176079.1	Activated muscle stem cells
	Myf5	NM_001106783.1	Activated cells
	Myf6	NM_013172.1	Differentiated cells
	Myog	NM_017115.2	Differentiated muscle stem cells
	MyH3	NM_012604.1	Regenerated myofibers
	Hgf	NM_017017.2	Growth factor
	Adam12	XM_017590240.1	Metallopeptidase
	Actn2	NM_001170325.1	Muscle structure
	Des	NM_022531.1	Muscle structure
	Dmd	NM_001005244.1	Muscle structure
	Tpm3	NM_173111.1	Muscle structure
	Tpm4	NM_012678.2	Muscle structure
	Tcap	NM_001271277.1	Muscle structure
	Acta1	NM_019212.2	Muscle structure
	Mybpc1	NM_001100758.1	Muscle structure
	Mybpc2	NM_001106257.1	Muscle structure
	Tmod1	NM_013044.2	Muscle structure
	Ttn	XM_001065955.4	Muscle structure
	Jsrp1	NM_001109591.1	Muscle structure
	Tnnt1	NM_001277260.1	Muscle structure
	Tnnt3	NM_001270665.1	Muscle structure
	MyH1	NM_001135158.1	Muscle structure
	MyH7	NM_017240.1	Muscle structure
	Mylk2	NM_057209.1	Muscle structure
	Sln	NM_001013247.1	Muscle structure
	Wnt7a	NM_001100473.1	Muscle homeostasis
Extracellular matrix	Mmp1	NM_001134530.1	Metalloproteinase
	Mmp8	NM_053963.2	Metalloproteinase
	Mmp13	NM_133530.1	Metalloproteinase
	Mmp2	NM_031054.2	Metalloproteinase
	Mmp9	NM_031055.1	Metalloproteinase
	Timp1	NM_053819.1	Tissue inhibitor of metalloproteinase
	Timp2	NM_021989.2	Tissue inhibitor of metalloproteinase
	Timp3	NM_012886.2	Tissue inhibitor of metalloproteinase
	Timp4	NM_001109393.1	Tissue inhibitor of metalloproteinase
	Ccn2	NM_022266.2	Growth factor
	Pdgfa	NM_012801.1	Growth factor

Table 2.1 List of genes included in custom NanoString panel (continued).

	Pdgfra	NM_012802.1	Growth factor/Receptor
	Dcn	NM_024129.1	Proteoglycan-ECM component
	Tgfb1	NM_021578.2	Growth factor
	Tgfbr1	NM_012775.2	Growth factor/Receptor
	Smad2	NM_001105817.1	Growth factor/Receptor
	Smad3	NM_013095.2	Signal transducer
	Smad4	NM_019275.2	Signal transducer
	Col1a1	NM_053304.1	ECM component
	Col3a1	NM_032085.1	ECM component
	Itga1	NM_030994.2	ECM component
	Itgb1	NM_017022.2	Cell-matrix interaction
	Itga2	XM_345156.6	Cell-matrix interaction
	Vwa1	NM_001013938.1	Cell-matrix interaction
Muscle anabolism and catabolism	Akt1	NM_033230.1	Anabolism/mTOR signaling
	Mtor	NM_019906.1	Anabolism/mTOR signaling
	Rheb	NM_013216.1	Anabolism/mTOR signaling
	Eif2b5	NM_138866.2	Anabolism/mTOR signaling
	Akt2	NM_017093.1	Anabolism/mTOR signaling
	Eif4b	NM_001008324.1	Anabolism/mTOR signaling
	Eif4e	NM_053974.2	Anabolism/mTOR signaling
	Eif4ebp1	NM_053857.1	Anabolism/mTOR signaling
	Eif4g1	XM_213569.6	Anabolism/mTOR signaling
	Grb10	NM_001109093.1	Anabolism
	Rps6ka1	NM_031107.1	Anabolism
	Rps6kb1	NM_031985.1	mTOR signaling
	Gsk3b	NM_032080.1	Anabolism
	Junb	NM_021836.2	Anabolism
	Nol3	NM_053516.2	Apoptosis
	Ikbkb	NM_053355.1	Anabolism
	Nfkbia	XM_001075778.1	Anabolism
	Foxo1	NM_001191846.2	Catabolism
	Foxo3	NM_001106395.1	Catabolism
	Fbxo32	NM_133521.1	Catabolism
	Trim63	NM_080903.1	Catabolism
	Camkk1	NM_031662.1	Catabolism
	Mstn	NM_019151.1	Anabolism
	Ctsl	NM_013156.2	Catabolism
	Prkaa1	NM_019142.2	Catabolism
	Fst	NM_012561.1	Anabolism
	Ccn4	NM_031716.1	Cellular survival
	Has1	NM_172323.1	Cellular survival
	Has2	NM_013153.1	Cellular survival

Table 2.1 List of genes included in custom NanoString panel (continued).

Angiogenesis	Vegfa	NM_031836.2	Growth factor
	Vegfb	NM_053549.1	Growth factor
	Angpt1	NM_053546.1	Growth factor
	Angpt2	NM_134454.1	Growth factor
	Kdr	NM_013062.1	Growth factor/Receptor
	Flt1	NM_019306.1	Growth factor/Receptor
	Nrp1	NM_145098.2	Growth factor/Receptor
	Tie1	NM_053545.1	Growth factor/Receptor
	Fgf2	NM_019305.2	Growth factor/Receptor
	Thsb1	NM_001013062.1	Cell-matrix interaction
	Mmp14	NM_031056.1	Metalloproteinase
Neuromuscular Junctions development and maintenance	Erbb2	NM_017003.2	Growth factor/Receptor
	Nrg1	NM_001271120.1	Growth factor
	App	NM_019288.1	Receptor
	Dvl1	NM_031820.1	Cytoplasmic
	Ptn	NM_017066.2	Growth factor
	Tnc	NM_053861.1	ECM component
	Utrn	NM_013070.1	Cytoskeleton
	Musk	NM_031061.1	Receptor
	Agrn	NM_175754.1	Proteoglycan
	Gphn	NM_022865.3	Cytoskeleton
Housekeeping genes	Ap3d1	XM_001076208.1	
	Hprt1	NM_012583.2	
	Rpl13a	NM_173340.2	
	Rpl32	NM_013226.2	
	Rplp0	NM_022402.2	
	Tbp	NM_001004198.1	

Table 2.2 List of differentially expressed genes for NanoString multiplex gene expression experiment: day 3 post-injection, SKM vs no injection.

Gene	Log2 Fold Change	p-Value
Acta1	-0.66971	0.000192
Actn2	-0.42959	0.001137
Akt2	-0.2893	0.000138
Ccl2	0.7501	0.035643
Ccl3	1.16217	0.039845
Ccl4	0.713829	0.030234
Ccn4	0.542539	0.001107
Ctgf	1.04175	0.00141
Cxcl1	1.31809	0.016552

Table 2.2 List of differentially expressed genes for NanoString multiplex gene expression experiment: day 3 post-injection, SKM vs no injection (continued).

Eif4E	-0.3366	4.62E-07
Emr1 (Adgr1)	1.71537	1.30E-06
Fbxo32	-0.53039	0.000256
Fgf2	-0.34323	0.022601
Il1 Beta	1.34503	0.047804
Il10R Alpha	0.668477	0.002628
Il12B	0.998022	0.001619
Il15	0.332355	0.02373
Il33	0.45802	2.80E-05
Il6	1.25683	0.000601
Irf4	0.480098	0.018731
Irf5	0.365171	0.020936
Musk	0.550579	0.003453
Mybpc1	-0.51843	0.001885
Mybpc2	-0.57281	0.009001
Myf6	-0.31371	0.008819
Myh1	-0.45159	0.004678
Mylk2	-0.54312	0.01118
Nfkbia	0.371676	0.0085
Nkg7	1.1667	0.003063
Nol3	-0.30202	0.004371
Pdgfralpha	0.265979	0.011507
Ptn	-0.27695	0.000558
Rps6Ka1	0.280497	0.013113
Sln	-0.56301	0.000452
Smad3	-0.33853	5.67E-05
Tgfb1	0.319911	0.009011
Timp1	0.520147	0.0222
Tnnt3	-0.59671	0.000549
Trim63	-0.56743	8.58E-05
Vegfa	-0.66269	1.01E-08
Vegfb	-0.49695	0.0006

Table 2.3 List of differentially expressed genes for NanoString multiplex gene expression experiment: day 7 post-injection, SKM vs no injection.

Gene	Log2 Fold Change	p-Value
Ccl2	0.908011	0.00514
Ccr2	0.990182	0.000448
Ccr5	1.1941	0.000675
Col3A1	0.286071	0.016886
Emr1 (Adgr1)	1.3909	0.000419
Fbxo32	-0.39921	0.004941
Gata3	0.550768	0.004535
Hgf	0.385965	0.000396
Il10	0.452325	0.029534
Il10R Alpha	0.467245	0.03599
Il12B	0.946276	0.002946
Il15	0.373096	0.011049
Irf5	0.514656	0.000901
Mmp12	1.14011	0.025262
Mmp14	0.500161	0.001065
Mmp2	0.317444	0.003082
Mmp9	0.384715	0.003672
Mstn	-0.37796	0.045505
Mybpc2	-0.42476	0.044452
Myh1	-0.35796	0.017106
Myh3	0.942842	0.00069
Myh7	0.662287	0.027568
Nkg7	1.1784	0.002743
Pdgfralpha	0.324787	0.001391
Stat1	0.504386	0.005488
Tcap	-0.47188	0.008383
Tgfb1	0.282138	0.021083
Timp3	-0.34996	0.007427
Timp4	-0.55493	0.010304
Tnnt1	0.469103	0.019561
Ttn	-0.44354	0.042758
Vegfr2	0.343954	0.003846

Table 2.4 List of differentially expressed genes for NanoString multiplex gene expression experiment: day 3 post-injection, SKM vs saline.

Gene	Log2 Fold Change	p-Value
Ctgf	0.697289	0.040615
Cxcr2	-0.35439	0.031721
Emr1 (Adgr1)	1.38856	2.31E-05
Il33	0.265186	0.02189
Pparg	0.395146	0.00136
Timp4	0.522308	0.018532

Table 2.5 List of differentially expressed genes for NanoString multiplex gene expression experiment: day 7 post-injection, SKM vs saline.

Gene	Log2 Fold Change	p-Value
Cxcr2	-0.35011	0.042016
Emr1 (Adgr1)	1.10681	0.005519
Il33	0.273073	0.012062
Nfkbia	-0.41266	0.003011
Thsb1	-0.3888	0.025237
Vegfr2	0.292649	0.014203

Figure 2.6 SKM injection stimulates muscle regeneration and immune response related pathways and genes as demonstrated through differential bulk RNA sequencing analysis.

RNA isolated from tongue tissues at day 3 and 7 post-injection of SKM or saline and non-injected tissues – previously used for NanoString multiplex gene expression analysis – underwent bulk RNA sequencing. Volcano plots of differentially expressed genes through comparison of SKM and non-injected tissues at day 3 (A) and day 7 (B) post-injection are shown, alongside their respective gene ontology pathways for up- and downregulated biological processes. Similar volcano plots for differential expression between SKM and saline injected time points at day 3 (C) and day 7 (D) post-injection are shown. n=8 animals analyzed per group.

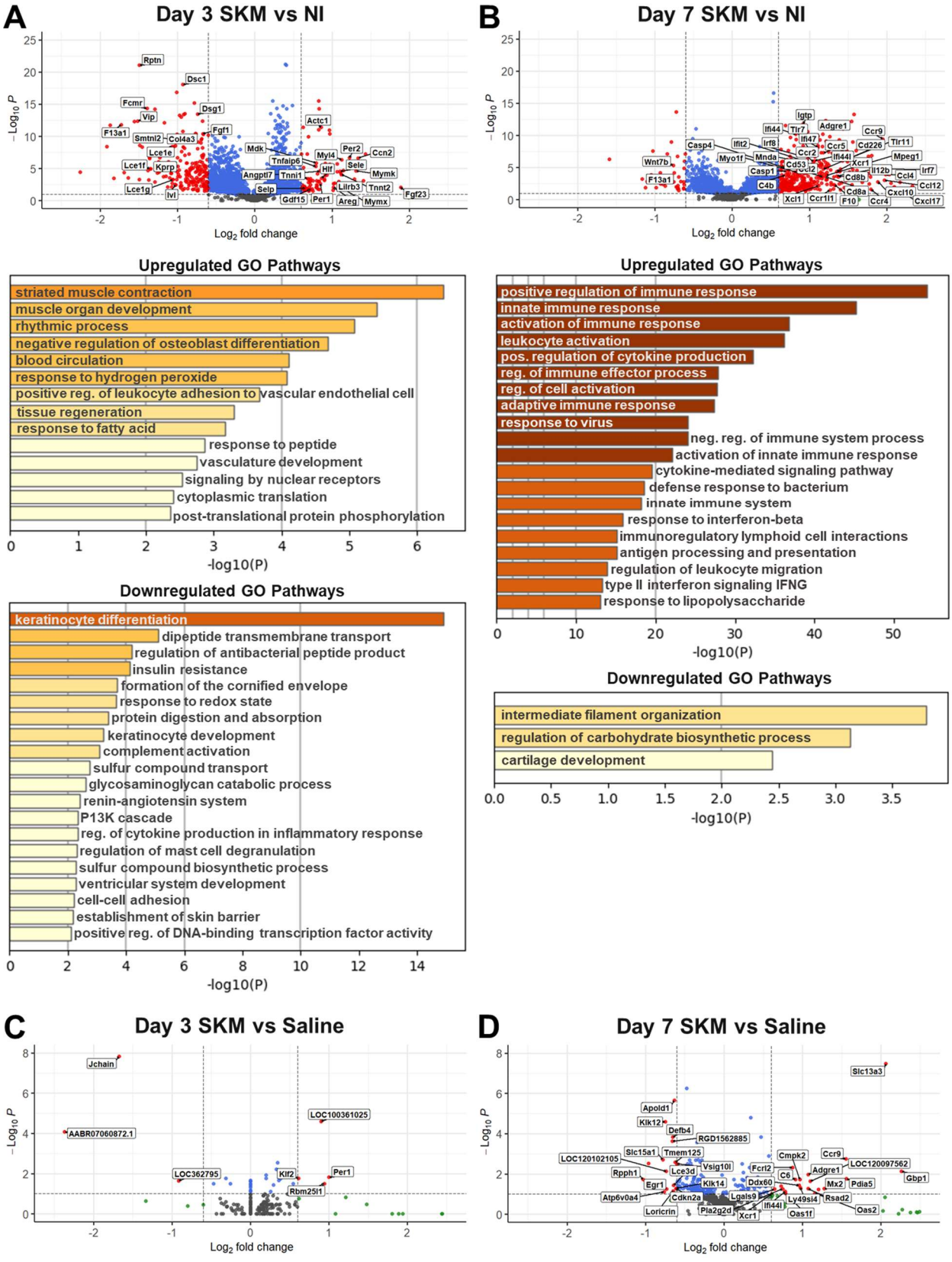

A
Day 3 SKM vs NI
B
Day 7 SKM vs NI
Upregulated GO Pathways
striated muscle contraction
muscle organ development
rhythmic process
negative regulation of osteoblast differentiation
blood circulation
response to hydrogen peroxide
positive reg. of leukocyte adhesion to vascular endothelial cell
tissue regeneration
response to fatty acid
response to peptide
vasculature development
signaling by nuclear receptors
cytoplasmic translation
post-translational protein phosphorylation
-log10(P)
Upregulated GO Pathways
positive regulation of immune response
innate immune response
activation of immune response
leukocyte activation
pos. regulation of cytokine production
reg. of immune effector process
reg. of cell activation
adaptive immune response
response to virus
neg. reg. of immune system process
activation of innate immune response
cytokine-mediated signaling pathway
defense response to bacterium
innate immune system
response to interferon-beta
immunoregulatory lymphoid cell interactions
antigen processing and presentation
regulation of leukocyte migration
type II interferon signaling IFNG
response to lipopolysaccharide
-log10(P)
Downregulated GO Pathways
keratinocyte differentiation
dipeptide transmembrane transport
regulation of antibacterial peptide product
insulin resistance
formation of the cornified envelope
response to redox state
protein digestion and absorption
keratinocyte development
complement activation
sulfur compound transport
glycosaminoglycan catabolic process
renin-angiotensin system
P13K cascade
reg. of cytokine production in inflammatory response
regulation of mast cell degranulation
sulfur compound biosynthetic process
ventricular system development
cell-cell adhesion
establishment of skin barrier
positive reg. of DNA-binding transcription factor activity
-log10(P)
Downregulated GO Pathways
intermediate filament organization
regulation of carbohydrate biosynthetic process
cartilage development
-log10(P)
C
Day 3 SKM vs Saline
D
Day 7 SKM vs Saline
Log2 fold change

Table 2.6 List of differentially expressed genes for bulk RNA sequencing transcriptomics experiment: day 3 post-injection, SKM vs no injection.

Gene	log2 Fold Change	padj
Retn	-0.95746	0.010815
Serpine1	1.142371	2.03E-05
Slc51a	1.013068	0.025522
Tfrc	-0.68644	1.06E-07
Lrrc74b	-0.64219	0.006417
Tmprss11f	-0.77172	0.001459
Hunk	-0.73361	0.000456
Slc15a2	-1.63838	0.000299
Limch1	-0.60137	8.67E-05
Tfcp2l1	-0.97519	5.41E-14
Mbnl3	-0.6812	0.001464
Serpinb7	-0.62513	4.63E-05
Esrrg	-0.62527	0.001073
Ptpn4	-0.62009	4.57E-07
Sele	1.101355	2.78E-05
Areg	1.018507	0.009352
Selp	0.654203	0.011228
Mpz	-0.60982	7.68E-05
Cited1	-0.61849	0.009445
Ltc4s	-1.03066	0.003248
Hs3st3b1	-0.75602	0.00518
AABR07029195.1	1.429484	5.76E-08
Tab3	-0.64792	0.000153
Lrrc52	-0.94868	0.00483
Lpin1	-0.99047	1.02E-10
Fcmr	-1.3925	4.50E-15
Ston2	-0.95163	1.01E-13
Ppargc1a	-0.88491	1.48E-06
Sec14l3	-0.63485	0.001472
Kera	-0.73333	0.001205
Muc15	-1.29065	5.56E-15
Coch	1.314584	0.017685
Car8	-0.65129	0.033037
Abtb3	-0.64848	3.51E-06
Nr4a3	0.650624	0.008541
Spon2	-0.61727	0.005327
Pdpk1	-0.60217	6.50E-11
Mymk	1.306864	2.46E-05

Table 2.6 List of differentially expressed genes for bulk RNA sequencing transcriptomics experiment: day 3 post-injection, SKM vs no injection (continued).

Lrrn3	0.740086	0.01551
Pvalb	0.807515	6.89E-05
Itgb8	-0.67838	4.08E-13
Ryr3	-0.87979	1.44E-06
Padi1	-1.00415	5.09E-11
Hyal4	-0.72752	4.15E-06
Casp14	-0.65146	3.73E-05
Per1	0.84812	0.002273
Ehf	-0.6325	9.86E-06
Prkaa2	-0.71959	8.84E-05
Apold1	0.61525	0.00377
Gsdma	-0.66759	6.34E-08
Galnt14	0.699139	0.034189
Actc1	0.859313	4.14E-12
Crnn	-0.8702	0.000511
Nrk	-1.34764	1.22E-05
Fgf22	-0.96662	0.000184
Elmod1	-0.85051	6.73E-05
Tnni1	0.681479	0.000413
Krt90	-0.62947	5.06E-06
Foxa1	-0.63396	0.008016
Ivl	-1.02165	0.003655
LOC102552326	-1.14742	0.00017
Hcn4	-0.88625	8.97E-05
Pdk4	-0.69754	0.005223
Angptl7	0.842355	2.53E-05
LOC680121	0.829447	5.13E-15
Wee1	0.970117	2.41E-06
Slc7a11	-0.77273	1.44E-06
Cd163	-1.23975	3.68E-05
Elovl7	-0.91824	3.76E-14
Cpa4	-1.05046	3.92E-09
Pnma1	0.719611	0.003577
Zyg11b	-0.74118	7.86E-09
Tmem154	-0.81741	1.14E-05
Krt24	-0.68788	2.38E-10
LOC100362814	-0.97663	1.76E-05
Tenm4	-0.69793	9.88E-10
Cpa3	-1.86817	1.85E-12

Table 2.6 List of differentially expressed genes for bulk RNA sequencing transcriptomics experiment: day 3 post-injection, SKM vs no injection (continued).

Ptpn3	-0.67458	2.18E-07
Slc15a1	-0.62236	0.009888
Fam180a	0.643784	0.006129
Mfap3l	-0.6841	1.02E-06
Rab27b	-0.76909	4.24E-06
Adh6	0.749631	0.000828
Cemip	-0.81345	0.000269
Gan	-0.84046	1.22E-05
C1qb	-0.86853	0.013013
C1qc	-0.80101	0.019074
Efr3b	-0.68809	1.37E-05
Alox5	-0.6018	0.015667
LOC100911681	-0.77802	0.015778
Spink5	-0.69104	3.15E-10
Npas2	-1.17841	0.000187
Crisp3	-0.86633	7.68E-05
Scd	0.929886	0.000112
Fgf1	-0.67187	4.11E-11
Gfod1	-0.74173	8.28E-06
Iqsec3	-1.07297	0.007278
Ccn1	0.714727	0.001186
Bmal1	-1.24251	8.74E-07
Sacs	-0.70847	7.92E-07
Nxnl2	0.670862	0.01396
Aox3	-0.80848	1.71E-06
Hs3st6	-0.60876	0.005255
Slc1a1	-0.81145	0.000904
Ccn2	1.337688	2.32E-07
Prune2	-0.63057	4.67E-05
Smtnl2	-0.86078	5.86E-10
Abca12	-0.7625	3.90E-11
Col4a3	-0.79766	4.71E-10
Tead1	-0.76584	3.35E-11
Slc9a2	-1.00343	2.99E-05
F13a1	-1.72639	1.59E-12
Aqp4	-0.83367	1.68E-05
Plcd4	-0.61247	0.001288
Pla2g2f	-0.73913	1.13E-05
Dsg1	-0.74256	3.49E-14

Table 2.6 List of differentially expressed genes for bulk RNA sequencing transcriptomics experiment: day 3 post-injection, SKM vs no injection (continued).

Fcna	-1.23095	2.26E-07
Slc46a2	-0.89608	0.000472
Tubb2b	0.692537	0.000442
Gja5	0.82735	3.04E-16
Ppargc1b	-0.75281	0.000267
Gpr157	-0.6644	2.65E-06
Mdk	0.791237	1.36E-06
Asprv1	-0.9261	4.55E-09
Cdhr5	0.691568	0.001579
Camk1d	-1.01335	1.42E-17
Ppp1r3c	-0.73654	0.001116
Tpsb2	-1.36113	3.05E-07
Rptn	-1.49424	8.45E-22
Mpp7	-0.66445	5.09E-11
Vip	-1.51259	4.20E-13
Klk5	-0.9982	2.26E-07
Tnnc1	0.832804	0.000899
Cpeb1	0.705538	0.007134
Lipk	-0.66853	0.000615
Lypd5	-0.92932	1.70E-11
Chrnd	0.900156	0.000761
Trpv3	-0.8067	0.001214
Gdf15	0.719217	0.017858
Per2	1.221492	2.07E-07
Fosl1	0.669557	0.020646
Cma1	-1.45772	4.95E-09
Ms4a2	-1.91355	4.08E-09
Sec1	1.110186	5.81E-05
Dbp	0.96742	7.72E-06
Ppara	-0.65855	0.002746
Id1	0.631252	7.72E-06
Klk9	-0.70746	4.99E-06
Ccdc78	-0.78459	0.001069
Esyt3	-0.64641	0.000143
AABR07046657.1	-0.6623	0.00686
Crabp1	0.691392	1.11E-10
LOC103695131	-1.69032	4.44E-05
Zdbf2	-0.61623	0.000193
Tpsab1	-0.995	0.000185

Table 2.6 List of differentially expressed genes for bulk RNA sequencing transcriptomics experiment: day 3 post-injection, SKM vs no injection (continued).

Scel	-0.72756	7.78E-10
Exph5	-0.90223	3.12E-14
Fmo9	-0.72097	2.75E-05
Pla2g3	-1.28009	2.81E-06
Adgrf2	-0.75038	1.24E-06
Yod1	-0.66576	0.000215
Id3	0.625196	4.14E-12
Slc6a19	-1.02762	3.16E-09
Drp2	-0.88147	2.33E-05
Tenm2	-0.66778	9.56E-08
Pnpla1	-0.81791	6.31E-06
Hoxc13	-0.62802	0.011503
Dynapl1	-0.8129	0.001551
LOC120093525	0.821582	0.00114
Kprp	-0.99446	4.75E-06
Slc26a9	-0.85074	3.53E-05
Tspan4	0.969616	4.11E-11
Serpina3a	0.801411	0.003515
Zbtb16	-0.65766	0.006328
Rpl9-ps31	0.719606	0.000398
Nfasc	-0.69926	0.000456
Ankrd52	-0.78207	6.31E-16
Usp13	-0.70231	1.71E-05
Ccl24	-0.79949	9.00E-06
Rpl6-ps1	0.603151	5.51E-08
Rpl39l	0.750416	0.03335
Pdia5	1.03429	0.001944
Krt4	-0.66852	0.004141
Spink7	-0.85203	0.002314
LOC120100586	-1.0111	0.000556
Cfd	-0.70255	0.000576
Col28a1	-0.67683	3.37E-05
Tnnt2	1.118973	8.73E-05
LOC100911055	1.406321	0.000775
Lyc2	-2.25643	3.63E-05
Sectm1b	0.698352	0.027021
Macc1	-0.61938	0.001068
LOC685351	-0.96093	0.005587
C17h6orf52	0.641896	0.017286

Table 2.6 List of differentially expressed genes for bulk RNA sequencing transcriptomics experiment: day 3 post-injection, SKM vs no injection (continued).

Ces1a	0.627971	0.005661
Lce1e	-1.07091	3.73E-09
Dnase1l2	-0.85401	5.95E-08
Mymx	1.078656	0.005851
Accsl	-0.73692	0.02833
Pde4d	-0.61203	4.93E-05
Ciart	0.712384	0.016071
Alpg	-0.62744	0.008482
Fbn2	-0.65623	0.003347
AABR07044301.1	-0.79798	0.00378
Slc41a3	-0.83852	0.000149
Faah	0.616926	0.013488
Syt14	-0.87742	0.000193
AABR07035839.1	-0.60556	0.001467
Lilrb3	1.086129	0.001092
LOC103691629	-1.49534	0.000524
Lyg1	-0.91168	6.66E-09
Cntfr	0.824737	9.59E-12
LOC100909434	-0.8296	0.001153
Acp7	-1.35887	1.83E-07
Dnah5	-1.29092	0.001228
Rps28-ps1	0.605964	0.025334
Rtl9	-0.91019	0.014001
Sall4	-0.64807	0.018173
Dnah3	-0.74499	0.02666
Myl4	1.125288	4.57E-07
Tnfaip6	0.789942	4.80E-06
Kctd4	-0.77595	0.000549
Asb2	-1.11641	9.26E-07
Zfp185	-0.67481	6.03E-09
Zfp106	-0.64723	4.43E-06
Scn1a	-0.956	0.001724
Mcpt1l1	-1.55834	4.72E-13
Rhebl1	0.81283	0.015508
Nccrp1	-0.75195	2.62E-05
Adgra1	-0.93097	0.020068
Hephl1	-1.48839	2.50E-09
Dsc1	-0.92985	8.37E-19
Tchh	-1.44458	1.40E-06

Table 2.6 List of differentially expressed genes for bulk RNA sequencing transcriptomics experiment: day 3 post-injection, SKM vs no injection (continued).

Slc19a3	-1.08524	5.90E-05
Cys1	0.965735	1.11E-11
Krt78	-0.65499	5.72E-06
Cdkn2a	0.613295	0.015667
Rnd1	0.799538	0.000796
Emb	0.803988	0.004707
LOC100360491	0.661118	0.024897
ENSRNOG00000062441	-1.10286	0.000278
LOC688858	-2.50762	3.96E-07
ENSRNOG00000063087	0.697607	0.01754
ENSRNOG00000063139	-1.06579	0.000546
LOC102555814	-0.949	2.21E-08
ENSRNOG00000063787	0.794608	0.008818
LOC120099628	1.018224	0.002468
Kcna1	-0.98821	8.12E-05
ENSRNOG00000064164	-0.84999	0.003877
Stfa2	0.796936	0.009962
ENSRNOG00000064486	-1.16956	7.33E-13
Sorl1	-0.6484	2.06E-05
Rnase3	1.289128	0.000467
ENSRNOG00000064986	-0.62562	0.004678
Obp3	-0.80571	0.018166
Ubxn2a	-0.90421	8.41E-08
LOC102550988	-0.73315	0.015698
Lce1f	-1.35505	1.17E-05
Il22ra1	-0.88138	0.001233
Fgf23	1.885609	0.008317
C4a	0.643229	0.026286
Peg10	-0.88631	2.67E-05
ENSRNOG00000067044	0.829779	0.018478
LOC103690742	0.606137	0.010606
Xkrx	-0.76435	3.67E-05
LOC102552128	-0.82275	0.001253
Hlf	0.861513	0.000321
LOC102549828	-1.08092	5.79E-05
LOC102553726	0.913105	0.000126
Klf2	0.910818	1.70E-06
ENSRNOG00000067970	-1.63164	7.19E-06
LOC102549173	0.617213	0.037378

LOC120103476	-0.60239	0.011721
Klk1	1.064127	1.99E-06
ENSRNOG00000068491	0.898609	0.000472
ENSRNOG00000068511	-0.75743	0.003871
LOC120093742	0.721158	0.000855
Fam210a	-0.70598	6.57E-05
ENSRNOG00000068920	1.064237	3.25E-05
Gng4	-1.37216	0.000624
Tchh	-1.82302	0.000347
Ttn	-0.62034	0.028428
Fam83b	-0.92344	4.94E-09
LOC120100587	-0.89202	0.000933
ENSRNOG00000069536	-1.25823	4.73E-05
ENSRNOG00000069550	-1.12647	0.007799
ENSRNOG00000069899	-10.2376	1.44E-05
Sgpp2	-0.96435	5.65E-07
Ccdc85b	0.674804	5.25E-08
ENSRNOG00000070648	-1.06742	0.001913
Lce1g	-1.05918	0.000524
LOC102551936	-1.38467	2.01E-05

Table 2.7 List of differentially expressed genes for bulk RNA sequencing transcriptomics experiment: day 7 post-injection, SKM vs no injection.

Gene	log2 Fold Change	padj
Ly86	1.069227	1.73E-05
Smpd3	-0.69086	0.000281
Gpsm3	0.641768	0.000133
RT1-Ba	0.717712	0.00954
Tap1	0.623173	1.93E-05
Psmb9	0.660693	0.000905
Prf1	0.872286	0.015869
Ptprc	0.872716	9.92E-05
Selplg	0.688145	0.003524
RT1-S3	0.628486	0.000797
RT1-N3	0.721016	0.000147
Pkib	0.68968	0.001571
Aif1	0.691998	0.003595
Oasl	1.770641	7.60E-05
Trpm2	0.90027	0.006369
Itgb2	0.715238	0.018689
Hvcn1	0.727368	0.000142
Oas1a	1.290162	5.43E-08
Klhl6	0.969139	5.46E-07
Mx1	2.031116	0.000129
Mx2	1.761051	1.73E-07
Stap1	1.123283	0.000426
Slc15a2	-0.92563	0.003524
Ifi47	1.108291	7.26E-09
Rhoh	0.615698	0.018606
Socs1	0.605771	0.000514
LOC24906	1.329552	5.76E-07
Xcl1	1.117234	0.006531
Fcrla	1.164923	5.34E-09
Lgals3bp	0.647705	0.001948
Cxcr3	0.967295	0.004873
Mnda	1.046394	3.31E-06
Cybb	0.889529	0.009465
Kmo	1.118636	0.000208
Tasl	1.161822	0.000524
Rgs18	0.845617	2.76E-05
Tlr7	1.070919	2.28E-07
Ppm1h	0.634659	2.76E-05

Table 2.7 List of differentially expressed genes for bulk RNA sequencing transcriptomics experiment: day 7 post-injection, SKM vs no injection (continued).

Il12b	1.350212	0.000211
Sash3	0.671528	0.008682
Dcstamp	1.681749	0.001949
Plek	0.688739	0.007544
Coch	1.057249	0.002109
Lyz2	0.947877	0.047454
Ccr9	1.946357	3.63E-10
Zbp1	1.22347	0.000735
Rig1	0.79985	4.14E-09
Xcr1	1.349771	4.17E-05
Cry1	-0.72362	2.09E-14
Ccr1l1	1.263656	0.033174
Itk	0.675198	0.005087
Atp6v0d2	1.134634	0.030381
Dock2	0.697194	0.003431
Ncf4	0.753965	0.001142
Arhgap9	0.687546	0.003524
Cd8b	1.374823	0.000274
Ccl2	1.166499	0.000269
Cd8a	1.206627	0.000289
Havcr1	0.647845	0.04401
Rac2	0.796981	0.00041
Casp1	0.703188	4.08E-05
Rsad2	1.572813	5.25E-14
Cyth4	0.703171	0.000355
Cmpk2	1.122283	1.01E-06
Plxnc1	0.627094	0.00043
Slamf9	1.491026	1.28E-06
Parp12	0.651221	1.02E-06
Myo1f	0.835927	5.14E-05
Cadps	-0.66772	0.001494
Slamf8	0.916189	3.16E-05
Gpnmb	0.778146	0.020504
Elmod1	-0.72186	0.009382
C3ar1	0.981131	0.000209
Cnr2	0.776891	0.002849
Ivl	-0.98222	0.014237
Tbx21	0.658154	0.010873
Epsti1	1.137942	8.71E-06

Table 2.7 List of differentially expressed genes for bulk RNA sequencing transcriptomics experiment: day 7 post-injection, SKM vs no injection (continued).

Lck	0.727291	0.016502
Il18	0.656525	0.00199
Wee1	-0.61984	1.02E-06
Clec4a3	0.926756	0.000732
Clec4a	1.14132	0.000277
Cd163	-0.75544	0.001668
Cd180	1.133824	0.000182
Ccr4	1.794222	0.024929
Lcp1	0.669389	0.017
Slc4a5	2.328453	0.007278
Mmp7	2.50559	0.000408
Laptm5	0.686509	0.001218
Ccl4	1.983959	0.000128
Tifab	0.764588	0.000827
Slc25a48	0.737385	0.039636
Spi1	0.615309	0.013039
Lpxn	0.736964	0.000251
Gpr18	1.102681	0.001454
Lgals9	0.914862	4.14E-09
Abca4	1.155436	3.25E-06
Themis2	0.614597	0.005216
Gpr165	-1.1012	0.001442
Npas2	1.142387	4.93E-05
Ptpn18	0.640586	0.000452
Slc6a12	0.788247	0.014909
Trem2	0.717768	0.01255
Fyb1	0.847928	0.000274
Nefm	-0.62795	0.021909
Blnk	0.648397	7.12E-06
Evi2b	1.22773	1.07E-05
Snx20	0.744879	0.00483
Dlgap3	1.155956	0.002849
AC109737.1	0.878531	0.003724
Bmal1	0.690133	0.002007
Slc11a1	0.899459	0.007236
Mcoln3	1.38528	0.003576
Mcoln2	1.094504	0.004645
Apobec1	0.899303	0.00026
Wnt7b	-0.76297	4.43E-06

Table 2.7 List of differentially expressed genes for bulk RNA sequencing transcriptomics experiment: day 7 post-injection, SKM vs no injection (continued).

Adora3	0.94311	0.01007
Cd3g	0.918132	0.002556
F13a1	-0.79939	0.000282
Fcrl2	1.147191	4.54E-08
Ccl17	0.843504	0.037749
Pstpip1	0.673269	0.007216
Serpinb6b	0.949901	0.003277
Cd1d1	0.64853	0.000444
Fam169a	-0.69337	0.037315
Ccl22	0.980159	0.007327
Ankra2	1.099146	4.75E-06
Qprt	0.688949	1.27E-06
AABR07001512.1	-1.12501	0.014195
Irf7	1.794006	1.30E-05
Cd72	0.6184	0.021596
Akr1c14	0.62625	1.01E-27
Unc93b1	0.74033	7.60E-05
Nkg7	1.213488	0.000784
Irf8	0.862706	1.29E-07
Cd53	0.953674	8.12E-05
Itgal	0.93226	0.000452
Cd83	0.609466	0.000678
Dhx58	1.121039	4.92E-06
Tpsb2	-0.70242	0.006445
Jph3	-1.04547	0.000181
Slc13a3	1.799708	1.29E-07
Ctrl	0.632206	5.03E-06
Coro1a	0.658844	0.021013
LOC100910979	1.209078	5.03E-13
Mthfd1l	-0.7082	1.73E-07
Ptpn22	0.769758	0.004726
Spib	1.39627	1.86E-05
Napsa	0.677228	0.012518
Il4i1	0.607144	0.019372
Per2	-0.79044	1.12E-09
Matk	0.60913	0.03535
Map4k1	0.687985	0.003288
Icam5	0.931606	0.025266
Cd37	0.792452	0.000576

Table 2.7 List of differentially expressed genes for bulk RNA sequencing transcriptomics experiment: day 7 post-injection, SKM vs no injection (continued).

Cyb561a3	0.782111	4.45E-12
Tyrobp	0.739925	0.0015
Ms4a7	0.861781	0.007177
Ms4a6a	0.963436	0.021013
Batf2	2.169622	0.001848
Tnfaip8l2	0.801813	0.000434
Fermt3	0.647299	0.005323
Fcgr1a	0.679192	0.008419
Siglec1	0.998456	0.012612
Timd2	1.100578	0.020825
Cd300lf	0.962662	0.014276
Arhgef39	0.670963	0.017601
Siglec5	0.903286	0.001511
Siglech	1.422064	1.68E-08
Nexmif	-0.63057	0.016081
Slc15a3	0.624327	0.007599
Ptprcap	1.071109	3.06E-05
Lat2	0.937258	2.00E-05
Gcsam	0.900991	0.000493
Ifi44	0.821919	6.73E-11
Cxcl9	0.761426	0.028303
Cxcl10	1.882517	0.001639
Lrrc25	0.770685	0.004319
Mettl21cl1	-0.62432	0.004366
Evi2a	1.20912	1.59E-06
Ifit3	0.810022	0.029928
Cd84	1.018529	0.000827
Nfam1	0.720312	0.005789
LOC681325	0.868537	0.024542
Cd96	0.760583	0.014553
Slamf7	0.753734	0.000294
Parp14	0.75341	2.08E-10
Hsh2d	0.946555	0.003916
Skap1	0.628214	0.015327
Herc6	1.235027	9.88E-10
Tpsab1	-0.93197	6.26E-05
Card11	0.842611	9.37E-05
Fcgr3a	2.019952	6.74E-06
Hs3st3a1	1.313844	0.004768

Table 2.7 List of differentially expressed genes for bulk RNA sequencing transcriptomics experiment: day 7 post-injection, SKM vs no injection (continued).

Ly9	0.933529	0.004366
Rnase6	1.557574	1.13E-09
Abca13	1.399189	0.030381
Wdr86	0.743409	0.035534
Myh6	0.894586	0.010152
Cfp	0.60574	0.000356
Txk	1.22577	5.37E-05
Chst13	1.213501	5.27E-06
Ifi27l2b	1.029825	0.001663
Glipr1	0.81195	0.000797
Jaml	0.795567	5.37E-05
RT1-DOa	0.680012	0.005227
Gapt	1.155215	2.76E-06
Igtp	0.917432	1.49E-12
Ctsw	0.688671	0.023981
Lilra5	0.982396	0.002793
Ncf2	0.628322	0.022319
Tmem150b	0.993203	0.003889
Ccl9	0.941538	0.031042
Pld4	0.718157	0.000113
Edar	0.604291	0.012368
Ntsr1	-1.04857	0.000135
Gbp4	1.602941	2.28E-08
Oasl2	1.236784	2.63E-06
Gbp7	1.172518	6.73E-11
Uba7	1.135208	4.77E-10
RT1-N2	0.688615	0.015283
Rnf213	0.724665	2.20E-08
Ccl12	1.967145	0.000955
Zbtb16	-1.02479	2.63E-08
Clec4a2	1.494064	0.000434
Sox11	0.644392	0.00246
Krt10	-0.60892	7.47E-08
Ube2l6	0.709146	6.11E-07
Gzmm	0.720406	0.038414
Samsn1	0.931042	0.001088
Irgm	0.954446	7.48E-10
Trim30c	1.723435	0.00075
Klra2	0.926624	9.40E-05

Table 2.7 List of differentially expressed genes for bulk RNA sequencing transcriptomics experiment: day 7 post-injection, SKM vs no injection (continued).

Gbp2	1.044734	5.03E-06
Cela1	0.774759	0.000507
Cenpa	0.76364	4.89E-07
Gbp5	1.106452	1.27E-10
Bank1	1.279096	0.00234
Tlr11	1.424162	9.72E-07
Capn13	0.786408	0.024718
RGD1559575	0.723159	2.30E-05
RT1-T24-3	0.63863	0.008886
RT1-Bb	0.907925	0.001222
Gpr174	1.223133	0.003944
Oas1f	1.262516	1.48E-10
LOC691141	0.88765	0.007067
F10	1.324158	0.005291
Casp4	0.672811	1.12E-05
Sp110	0.635925	1.47E-06
Plk5	-0.69978	0.018334
Ifit2	0.948192	1.02E-06
Cd7	0.711229	0.000819
Ppp1r27	0.808855	1.38E-06
Itgax	0.741292	0.003524
Spn	0.837421	0.00088
Nckap1l	0.683775	0.000797
Arl5c	0.819159	0.01283
Slfn2	0.729369	1.87E-05
Usp18	1.481967	2.70E-08
Siglec10	1.005129	0.003045
Xaf1	1.214266	7.41E-10
Cd68	0.819202	0.015487
Calhm6	1.064261	0.017314
Cxcl17	2.095159	0.009828
Defb52	2.841906	0.007968
Cd226	1.176186	1.86E-05
Slamf6	1.274474	0.004993
LOC685351	-1.59058	5.46E-07
Hcls1	0.767183	0.001137
MGC105567	1.249487	4.43E-06
RGD1305184	1.467047	0.001176
Ctla2a	0.759508	0.000299

Table 2.7 List of differentially expressed genes for bulk RNA sequencing transcriptomics experiment: day 7 post-injection, SKM vs no injection (continued).

LOC690862	1.27005	2.41E-05
Clec4a1	0.925696	0.000414
Tm6sf2	1.016199	0.022319
Tlr12	1.015375	0.000531
LOC680920	1.010882	0.008965
Trim34	0.629283	1.51E-08
Fcrl5	0.819288	0.02874
LOC100909964	1.306226	0.020903
Gvin1	0.847845	0.000108
Rfx2	-0.75289	6.53E-05
RT1-Ha	0.988235	0.029926
Tlr8	0.705108	0.004392
LOC100909671	0.674339	0.015515
RGD1559482	0.725293	0.002849
Adgre1	1.428378	9.62E-12
Fcgr2a-ps1	0.82046	0.01626
Lilrb3	1.046463	0.00513
Bcl2a1	1.083918	0.000393
Tlr9	0.859014	0.018212
Il2rb	0.687516	0.015056
Traf1	0.605287	0.000784
Ccr5	1.175952	5.21E-08
Oas2	1.514554	5.09E-05
LOC108348047	0.716283	0.00234
Nebl	-0.62694	0.001686
Gzmb	1.610999	2.94E-05
Ifi44l	1.063485	8.68E-07
Ms4a6bl	0.745012	0.006216
Vav1	0.647311	0.015624
Ebi3	0.632042	0.04704
Myl4	0.641827	0.020429
Ctsz	0.772653	0.000429
Cd300c2	0.635601	0.011267
AABR07044397.1	0.734864	0.007603
Cfb	0.921155	0.012766
Clec9a	1.163032	8.09E-05
Parvg	0.798222	0.001875
Btk	0.834368	0.000229
Samd9	1.105808	4.14E-09

Table 2.7 List of differentially expressed genes for bulk RNA sequencing transcriptomics experiment: day 7 post-injection, SKM vs no injection (continued).

AABR07008309.1	0.922375	0.014838
Klri1	0.642358	0.039766
Ly49si4	1.556195	2.01E-05
Lonrf1	-0.62209	1.36E-05
Flt3	0.769554	0.000827
Clec12a	0.95307	0.003277
Lilrb2	0.614919	0.04694
Pou2f2	0.832467	0.014318
Rnf128	0.749309	0.008178
Sla	0.648418	0.007972
LOC100360413	0.627114	0.008145
LOC120097562	1.540564	6.43E-13
Plcb2	0.729327	0.003286
Ly49s7	2.602037	0.000107
Ddx60	1.380654	5.30E-10
Myo1g	0.604125	0.020554
Oas3	0.944556	0.008902
AABR07044383.1	0.623927	0.006119
Clec2d2	0.680744	0.00975
LOC497796	1.738202	0.000199
Klrd1	1.202886	0.00011
Emb	0.623026	0.000489
Psca	0.72329	0.029873
LOC100360491	0.663617	0.008425
Tfec	0.792628	0.01391
Klrk1	0.956306	0.007019
LOC120093104	0.810625	0.000125
RT1-Hb-ps1	0.735063	0.020504
Klra5	1.547767	0.004812
LOC120102105	-0.89571	0.004087
Lilrb3l	0.789685	0.00015
ENSRNOG00000062480	1.018862	0.019756
LOC120100725	1.158229	0.000234
Ccr2	1.047732	1.17E-06
Mpeg1	1.214047	0.000184
Slfn4	0.943988	0.038861
ENSRNOG00000063619	1.056511	0.001581
LOC102549592	0.836131	0.012523
Samd9l	0.825628	4.09E-10

Table 2.7 List of differentially expressed genes for bulk RNA sequencing transcriptomics experiment: day 7 post-injection, SKM vs no injection (continued).

ENSRNOG00000063720	0.629562	0.002529
Tnip3	0.895989	0.030381
Phf11b	2.051061	0.002722
Olr1585	1.125473	9.40E-05
Ly49si2	1.202481	8.87E-06
ENSRNOG00000064682	0.64057	0.019872
ENSRNOG00000065055	3.68011	0.003924
LOC102552940	1.446845	0.01391
Naip5	1.217727	0.000881
LOC102556096	0.93876	1.22E-06
ENSRNOG00000065241	1.024126	0.008202
Or2b4	0.878687	0.018109
Gpr65	0.634386	0.033207
ENSRNOG00000065633	-0.70781	0.021831
LOC120102230	0.687839	2.78E-12
ENSRNOG00000065679	0.605527	0.015257
Il7r	0.611535	0.004141
Klrc3	0.888203	0.000206
Rtp4	1.245342	3.64E-08
RGD1563400	0.621131	0.033125
C4a	0.615374	0.011766
LOC120100584	0.834373	0.04698
ENSRNOG00000066615	1.386869	4.24E-05
ENSRNOG00000066636	1.314339	0.000294
ENSRNOG00000066766	1.178886	6.89E-07
LOC102550999	0.639887	0.048782
Nat8f3	-0.87001	0.007278
Tnfsf10	0.743498	1.74E-07
Gbp6	0.975676	2.62E-11
Eppk1	-1.16719	0.000638
Gbp1	2.971271	2.75E-13
ENSRNOG00000069024	-0.83945	7.72E-08
Isg15	1.787841	0.000295
ENSRNOG00000069681	1.417383	0.00232
LOC108348241	1.01952	0.011373
Mrgprg	5.275402	7.07E-05
Oas1i	1.142434	2.69E-06
ENSRNOG00000069878	1.15791	4.99E-06
Sgpp2	-0.71579	0.011472

Table 2.7 List of differentially expressed genes for bulk RNA sequencing transcriptomics experiment: day 7 post-injection, SKM vs no injection (continued).

LOC103694557	1.77146	0.003635
ENSRNOG00000070285	0.690119	0.032408
C4b	0.685995	0.000146
Gbp6-ps2	3.214223	8.09E-05
ENSRNOG00000070662	5.30664	0.005917
ENSRNOG00000070909	0.710426	0.029533

Table 2.8 List of differentially expressed genes for bulk RNA sequencing transcriptomics experiment: day 3 post-injection, SKM vs saline.

Gene	**log2 Fold Change**	**padj**
Jchain	-1.67467	1.46E-08
LOC100361025	0.899118	2.60E-05
Per1	1.001377	0.015071
RGD1563231	-4.2734	4.56E-14
AABR07060872.1	-2.36921	8.12E-05
ENSRNOG00000063791	-3.38611	6.44E-07
Rbm25l1	0.941758	0.030943
LOC362795	-0.91568	0.02293
Klf2	0.613335	0.017461
ENSRNOG00000067894	-2.9721	0.017461
ENSRNOG00000069088	-3.95058	3.66E-07

Table 2.9 List of differentially expressed genes for bulk RNA sequencing transcriptomics experiment: day 7 post-injection, SKM vs saline.

Gene	**log2 Fold Change**	**padj**
Mx2	1.277872	0.052012
Ccr9	1.55382	0.001773
Xcr1	0.605243	0.096916
Tmem125	-0.62086	0.002637
Rsad2	1.073406	0.053435
Cmpk2	0.966095	0.0187
Apold1	-0.6333	2.20E-06
Slc15a1	-0.77942	0.001923
Lgals9	0.64122	0.057042
Atp6v0a4	-0.7632	0.077948
Defb4	-0.65263	0.000146
Fcrl2	0.874594	0.00473
Pla2g2d	0.747639	0.054751

Table 2.9 List of differentially expressed genes for bulk RNA sequencing transcriptomics experiment: day 7 post-injection, SKM vs saline (continued).

Slc13a3	2.061379	3.29E-08
Egr1	-0.73244	0.054585
Vsig10l	-0.60063	0.003075
C6	0.910593	0.0187
RGD1562885	-0.65643	0.000237
Pdia5	1.561081	0.017154
Oas1f	0.786263	0.093163
Klk14	-0.61087	0.052368
Klk12	-0.74546	2.53E-05
Adgre1	1.072294	0.01074
Oas2	1.15883	0.093323
Ifi44l	0.78139	0.073486
Ly49si4	0.973494	0.04748
Rpph1	-1.03309	0.0187
LOC120097562	1.099259	0.023038
Ddx60	0.959521	0.036988
Loricrin	-0.64772	0.069174
Cdkn2a	-0.61433	0.053939
LOC120102105	-0.73604	0.007405
ENSRNOG00000065952	3.865116	0.0187
ENSRNOG00000066407	-0.96469	0.002979
ENSRNOG00000067018	0.728203	0.040451
Lce3d	-0.64372	0.036818
Gbp1	2.26012	0.007405
ENSRNOG00000069681	1.201767	0.059816
Gbp6-ps2	3.435692	3.29E-08

2.2.5 SKM hydrogel promotes microvasculature development

Gene expression results from both NanoString and bulk RNA sequencing demonstrated upregulation in angiogenic signaling and vasculature development. To further investigate this, tissue sections were assessed for vasculature development 7 days post-injection of either saline or SKM since angiogenic signaling was observed at 3 days post-injection. Additionally, vasculature was assessed at 4 weeks post-injection. Tissue sections were stained against alpha smooth muscle actin and isolectin, and

arteriole size and density were assessed throughout the tissue at the 7 day timepoint, as there was no clear scar delineation at this acute timepoint, and within the scar area at the 4 week timepoint. At 7 days post-injection, SKM demonstrated significantly higher vessel density (Figure 2.7C) and a smaller size distribution of vessels (Figure 2.7D). These trends were maintained at 4 weeks post-injection, but the difference in vessel density was no longer significant (Figure 2.7E), while the difference in vessel sized distribution was maintained (Figure 2.7F).

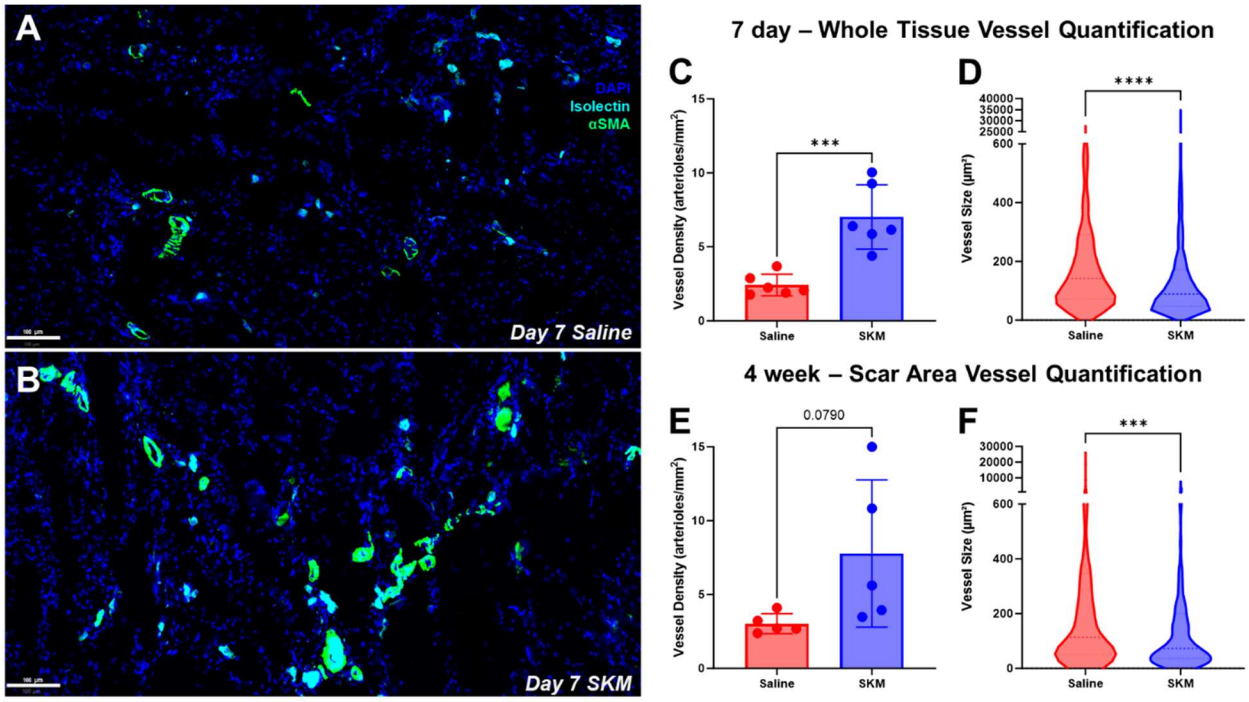


Figure 2.7 SKM injection promotes a transient increase in vasculature development.

Tissue sections were stained against smooth muscle (αSMA, green), endothelial cells (isolectin, cyan), and nuclei (DAPI). Arterioles, double positive for αSMA and isolectin, were counted and assessed for lumen area. Representative images of stained tissue from saline (A) and SKM (B) treated animals at 7 days post-injection are shown. (C) At 7 days post-injection, SKM group demonstrated significantly higher vessel density throughout the whole tissue section. (D) The vessels in SKM injected animals demonstrated a significantly smaller overall size distribution at 7 days post-injection. (F) At 4 weeks post-injection, there was a nonsignificant increase in vessel density within the scar area in SKM injected animals. (F) At 4 weeks post-injection, the smaller size distribution of vessels in the SKM group was maintained. Vessel density was compared with an unpaired t-test, ***$p<0.001$. Vessel size was compared with a Mann Whitney test, ***$p<0.001$, ****$p<0.0001$. n=6 animals per group.

2.2.6 SKM injection leads to increased fibroadipogenic progenitors at 3 days post-injection and encourages myogenic growth

FAPs – a population of mesenchymal stromal cells in the interstitial space[81] – appeared to be involved in the SKM response, based on the differential gene expression results shown above. Therefore, we assessed FAPs at 3 days post-injection within the area of

injury, which was defined by disrupted muscle structure and hypercellularity. Tissue sections from saline and SKM groups were stained against antibodies against PDGFRα, an established marker of FAPs,[82] and α-sarcoglycan, a muscle membrane marker (Figure 2.8A-B). Percentage of PDGFRα$^+$ cells (Figure 2.8C), normalized to the total number of cells within the injured area was compared between groups, and the SKM group demonstrated significantly increased proportion of these PDGFRα$^+$ cells (Figure 2.8D). Additionally, we observed infiltration of PDGFRα$^+$ cells into the SKM scaffold alongside myofibers (Figure 2.8E-F). To further investigate our hypothesis that FAPs were involved in mediating a SKM-driven pro-myogenic response, we stained against embryonic myosin heavy chain, a well-established marker of developing myofibers. We observed embryonic myosin heavy chain positive fibers, localizing alongside FAP cells that had infiltrated the SKM scaffold (Figure 2.8G-H).

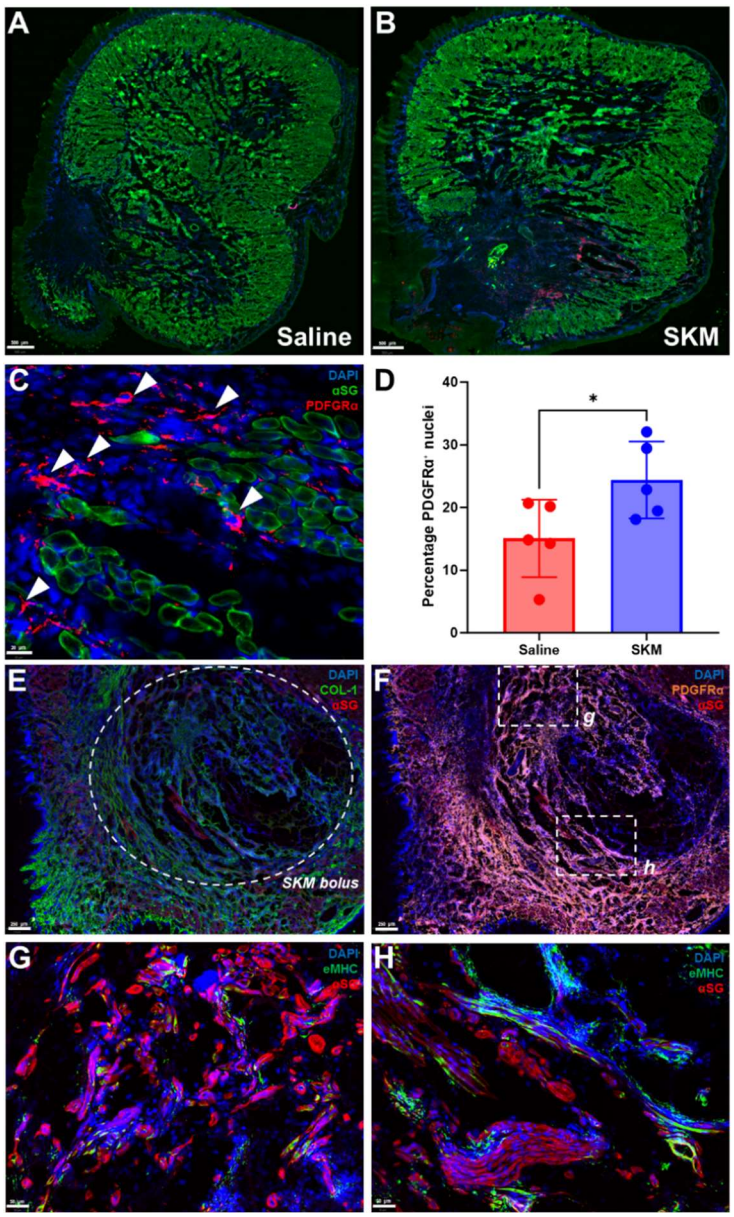


Figure 2.8 Fibroadipogenic progenitors are more prominent in the SKM group 3 days post-injection and are colocalized with developing myofibers within the SKM scaffold.

Tongue tissues harvested 3 days post-injection were stained against skeletal muscle (α-sarcoglycan, green), fibroadipogenic progenitors (PDGFRα, red), and nuclei (DAPI, blue) for both saline (A) and SKM (B) injection groups. PDGFRα$^+$ nuclei (C, white arrows) within the area of injury were normalized to total nuclei within the injury, and SKM demonstrated an increased percentage of PDGFRα$^+$ nuclei (D). SKM bolus was visualized with collagen staining (E, dashed oval), and of PDGFRα$^+$ nuclei (yellow), representing fibroadipogenic progenitors, were observed infiltrating the SKM bolus. Within the bolus, developing myofibers (embryonic myosin heavy chain, green) were observed in regions with high density of fibroadipogenic progenitors (G, H). n=5 animals/group.

2.2.7 SKM injection mitigates area of injury as early as 7 days post-injection

Given positive immune regulation and vasculature development gene expression signaling, as well as improved vascularization in the tissue 7 days post-injection of SKM, we investigated the development of tissue injury at 3 and 7 days post-injection. At these early timepoints, there is not a well-developed scar – instead, the injured area can be defined by damaged tissue and hypercellularity. Tissue morphology was assessed for these characteristics with a hematoxylin and eosin stain, and the region of injury was normalized to total tissue area. Representative tissue sections are shown for saline and SKM injected animals at 3 and 7 days post-injection (Figure 2.9A-B, D-E). At 3 days, there was no difference in injured area between groups (Figure 2.9C), but at 7 days post-injection, the SKM group demonstrated a decreased injured area compared to saline (Figure 2.9F).

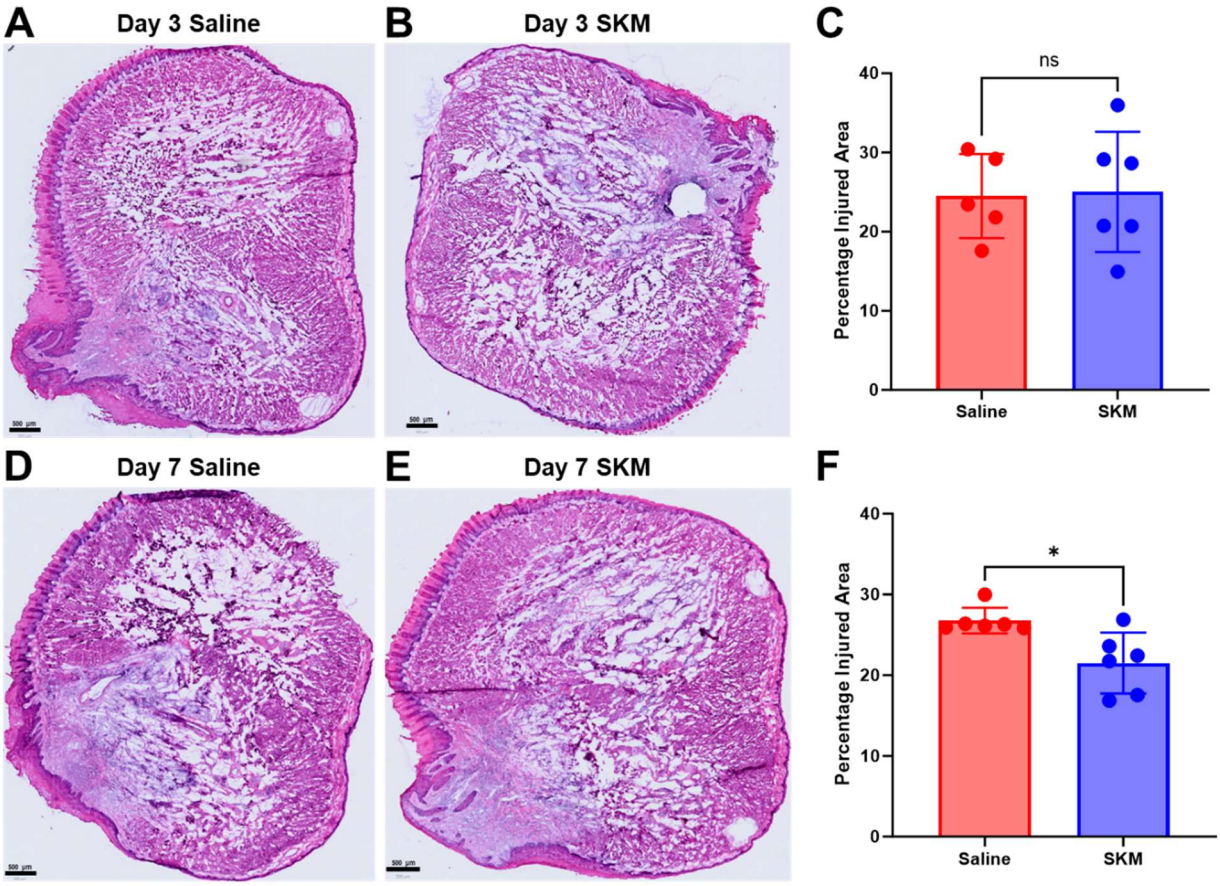


Figure 2.9 SKM injection mitigates area of injury as early as 7 days post-injection.

Tissue sections were stained against hematoxylin and eosin at the 3 day timepoint for saline (A) and SKM (B) treated animals, and the percentage of injured area normalized by the total tissue area was quantified (C). At the 7 day timepoint, representative images for saline (D) and SKM (E) are shown, alongside quantification of injured area (F). Injured area was compared with an unpaired t-test, *p<0.05. n=6 animals per group.

2.3 Discussion

SKM hydrogels have previously demonstrated induction of muscle regeneration, neovascularization, and ECM remodeling in several skeletal muscle conditions, including ischemia reperfusion[42] and birth-related mechanical injuries.[38] Thus, we hypothesized that injection of SKM hydrogel would mitigate scar formation and improve muscle regeneration in an animal model of partial glossectomy, which was previously developed to model pathologies associated with head and neck cancer treatment.[66] In this study, we

demonstrated that injection of SKM two weeks following a partial glossectomy, significantly improved histomorphological properties of the tongue. The active phase of muscle regeneration was completed 4 weeks after injection, as demonstrated by the proportion of muscle fibers with centralized nuclei in the site of injury returning to the healthy baseline,[83] so this timepoint was used for evaluation of histomorphological changes in the tongue. At this timepoint, we found that 300 μL SKM injection reduced scar formation and improved muscle regeneration within the scar region. These data suggest therapeutic efficacy of SKM in promoting constructive remodeling and reversing fibrosis of the tongue consequent to surgical resection. Interestingly, a smaller injection volume of SKM did not significantly reduce scar area as compared to saline controls. This is likely due to the shorter retention time with the smaller volume, which was insufficient to induce a therapeutic effect and consequent histomorphological changes. We further assessed the area of injury at 3 and 7 days post-injection of 300 μL SKM or saline and found that SKM begins to mitigate the area of injury as early as one week post-injection, supporting the improved tissue regeneration outcomes we found at the 4 week timepoint.

Gene expression experiments revealed differences between SKM and non-injected control animals, which were greater than those between SKM and saline groups, which highlights the importance of saline injected control groups, as a significant muscle regeneration cascade can result from injection injury alone. However, we did still observe interesting differential gene expression between the SKM and saline injected groups. Consistent with previous studies on ECM hydrogels,[37,38,84,85] we observed a strong macrophage response following SKM injection. Overall, SKM appears to modulate the injured tissue from pro- to anti-inflammatory immune phenotype; *Pparg* is particularly

associated with muscle repair and M2 macrophages, while *Il33* is associated with Treg recruitment and muscle regeneration.[81,86] The gene expression data, comparing SKM injection to both saline and non-injected controls, suggested involvement of FAP activity as a potential mechanism by which SKM injection yields the observed improvements in muscle regeneration and reduction in scar formation. FAPs are known to be the primary muscle-resident producers of *Il33* in skeletal muscle, which was upregulated at both 3 and 7 days post-injection in the SKM groups.[87] We also found upregulation of *Pdgfra*, a marker of FAPs at both timepoints when comparing gene expression between SKM and non-injected animals. FAP activity was also supported by the transient upregulation of *Il6* at day 3 – a myogenic factor when expressed at early timepoints that is primarily produced by FAPs during muscle regeneration[81] – along with cytokines commonly implicated in the cross-talk between FAPs, macrophages, Tregs, and muscle stem cells (*Il10, Il15)*.[88,89] To support these gene expression data, we demonstrated a significant increase in FAP cell density within the area of injury in the SKM group compared to saline at the 3 day timepoint. Additionally, we found that FAPs are recruited to the SKM bolus alongside newly formed myofibers. We further supported this hypothesis by demonstrating the presence of newly developed (embryonic myosin heavy chain positive) myofibers within the region of SKM hydrogel and co-localizing alongside FAPs. While not observed in other injury models,[38,42,90] SKM injection appears to repair the tongue tissue through FAP-mediated immunomodulatory activity in this injury model. Thus, the data presented here pose an exciting avenue for future research to investigate the precise interactions between ECM hydrogels, FAPs, immune populations, muscle stem cells and myofibers. Additionally, we found that SKM injection upregulated genes involved in angiogenesis,

which is consistent with our previous studies in which SKM induced neovascularization in other skeletal muscle injury models.[42,72]

Results of bulk RNA sequencing affirmed many findings from the NanoString multiplex gene expression panel; when compared to non-injected controls, SKM injection led to significant immunomodulation as well as increases in muscle regeneration and vascularization. Comparison to saline controls revealed fewer differentially expressed genes, but expression was again consistent with previous results. Transcriptomic changes predominately involved the immune system – particularly mitigating pro-inflammatory expression and promoting activity of macrophages and Tregs. Additionally, we observed upregulation of genes involved in muscle regeneration and proliferation in the SKM injected group compared to saline controls, supporting the improved muscle regeneration observed 4 weeks post-injection. Both NanoString and RNA sequencing analyses demonstrated upregulation in vascularization, and indeed we found a transient increase in microvasculature development at the 7 day timepoint with SKM treatment.

One limitation of the partial glossectomy injury model is that while it induces muscle damage and scar formation that mimic the pathologies associated with head and neck cancer treatment, it does not include radiation. Additionally, while substantial histomorphological improvements were observed in both scar formation and muscle regeneration following SKM, we did not observe complete remission of the scar, and while muscle fibers within the scar were larger in the SKM group than saline, they did not return to healthy tongue muscle fiber area distribution. As such, it may be beneficial to investigate the therapeutic efficacy of repeated SKM injections in future studies. Finally, while our preliminary mechanistic insights from this study support the immunomodulatory

effect of SKM, future studies utilizing flow cytometry would be valuable to differentiate and quantify changes in immune and muscle resident cell populations. Flow cytometry would additionally be helpful for further assessing the effect of SKM on FAPs, as using multiple markers to robustly identify this population is preferable to immunohistochemical staining.

Overall, the data support our hypothesis that SKM is a promising therapeutic for the treatment of fibrosis in the tongue. In this rat model of partial glossectomy, we demonstrate significant histomorphological improvements following SKM injection. Our gene expression data suggest immunomodulation towards a pro-regenerative phenotype. This study encourages further investigation of SKM for the regeneration of damaged tongue tissue for the potential treatment of dysphagia.

2.4 Conclusions

In conclusion, our study demonstrates that a cost-effective and easily administered acellular tissue-specific biomaterial significantly reduces scar formation and improves muscle regeneration following partial glossectomy in a rat model. We provide evidence that this biomaterial is immunomodulatory and promotes a pro-reparative phenotype. Overall, this biomaterial, which can be delivered minimally invasively, presents a promising option for future clinical translation in the regeneration of tongue muscle and treatment of dysphagia.

2.5 Materials and Methods

2.5.1 SKM Hydrogel Fabrication

SKM material was fabricated as previously described.[91] Briefly, porcine skeletal muscle was chopped into small cubes before being spun in a 1% sodium dodecyl sulfate detergent solution for 5 days, with daily solution changes. Tissue was thoroughly rinsed in water to remove residual detergent. Decellularized tissue was frozen at -80ºC and then lyophilized for 48 hours, after which the material was milled to a fine powder. This powder was partially enzymatically digested at 10 mg/ml in pepsin (1 mg/mL pepsin in 0.1 M HCl) pepsin for 48 hours, and then pH was neutralized, and ionic concentration balanced. SKM was brought to a concentration of 6 mg mL^{-1}, which was determined as the optimal concentration for skeletal muscle injection.[72]

2.5.2 Partial Glossectomy Model

All procedures were approved by the Institutional Animal Care and Use Committee at the University of California, San Diego. As oropharyngeal cancer is over twice as common in men than in women,[92] male Sprague Dawley rats weighing between 225-250 g (approximately 3 months old) underwent partial glossectomy injury, as previously established.[66] Briefly, animals were anesthetized with isoflurane, and buprenorphine was delivered subcutaneously for pain management. The tongue was retracted out of the mouth with a 4–0 silk suture. A 4mm dermal punch is used to standardize the volume of excised tongue. The dermal punch is applied to the left posterior quadrant of the tongue and inserted to a depth of 4mm, leaving a thin layer of intact ventral tongue so that the defect is not through and through. The volume of removed tongue is placed on a sheet

for visual confirmation of consistency between animals. Silver nitrate chemical cautery was used for hemostasis. The animals were then monitored for 5 days postoperatively; the rats were provided with a soft diet for the duration of the study period. Scar formation at the site of injury occurred over the following 2 weeks,[66] at which time point SKM was injected directly into the tongue.

2.5.3 Reliability of the SKM Injection and Volume Optimization

To enable visualization of SKM *in situ*, SKM was prelabeled with Alexa Fluor™ 568 NHS Ester (Thermo Fisher Scientific, Waltham, MA). SKM was incubated at room temperature for an hour to ensure complete binding. Fluorescently pre-labeled SKM was injected directly into the site of injury, two weeks following a partial glossectomy injury. Injection volumes of 50, 100, 200, and 300 µL were included (n=2 animals per volume); this range was determined based on SKM injections in other skeletal muscle injury models[72] and cell injections in the rat tongue[66]. The rat tongue can only accommodate so much injectate before the tongue swells too much and injectate spills out of the injection site (backflow) once the needle is withdrawn. From our prior experience with an injectate of similar viscosity, 300 µL was determined to be an upper limit of injected volume for the adult rate tongue in this model. Animals were euthanized and tongues were harvested 1 week following injection; cryosectioned and stained with DAPI nuclear counterstain for tissue localization. Tissue cross-sections were then visualized at 20X magnification using a Leica Ariol® fluorescent microscope.

2.5.4 Histomorphological Assessment of SKM Therapeutic Efficacy

2.5.4.1 Quantification of scar area

Two weeks following partial glossectomy injury, SKM or saline were injected into the injury site. Based on the injection volume optimization study, the 200 and 300 μL demonstrated good retention and spread in the tongue tissue. Thus, experimental groups included 200 μL SKM, 300 μL SKM, and 200 μL saline (n=6/group). Animals were euthanized 4 weeks following injection and tongues were harvested and cryosectioned. Masson's Trichrome (Polysciences, Warrington, PA) stain was used to identify collagen and muscle, and tissue sections were visualized using a Leica Aperio ScanScope ® CS2. For quantification of the scar area from the Masson's Trichrome stained tissue sections, Aperio ImageScope software was used to trace the border of the scar region, as defined by the blue collagen stain. The outer edge of the tongue cross-section was traced, and the area of the scar was normalized to total tongue area for each section. All sections containing the scar were analyzed, and normalized scar area data were averaged per animal.

2.5.4.2 Quantification of muscle fiber area and centralized nuclei

For this analysis, age-matched healthy control animals were euthanized (n=6) to assess muscle fiber area. For assessment of muscle regeneration within the scar area, fibrosis was identified with an anti-collagen I antibody (Bio-Rad, Hercules, CA, 1:200) with an Alexa Fluor™ 488 secondary (Invitrogen, Carlsbad, California, 1:500) secondary and myofiber membranes were identified with anti-α-sarcoglycan antibody (Leica Biosystems, Wetzlar, Germany, 1:200) with an Alexa Fluor™ 568 secondary (Invitrogen, Carlsbad,

California, 1:500). Tissue sections were visualized using a Leica Ariol® fluorescent microscope. For quantification of muscle fibers from immunohistochemical staining, the scar region (collagen I) and cross-sectional muscle fibers (α-sarcoglycan) within the scar region were identified, and myofiber cross-sectional areas were quantified. For healthy controls, sections were selected from the location in tongue where the scar was present in injured animals, and a circular region of interest was drawn in the left anterior tongue at these locations to match the site of injury. For the healthy animals, all muscle fibers within the selected region of interest were analyzed. Muscle fibers with centralized nuclei (DAPI) were also identified. Numbers of fibers were normalized to scar area, and the numbers of centrally nucleated fibers were normalized to muscle fiber counts within the scar. All sections containing scar were analyzed, and data were averaged per animal.

2.5.4.3 Quantification of arteriole density

For evaluation of vascularization, blood vessels were identified with a co-stain of an anti-αSMA antibody (Agilent, Santa Clara, California, 1:75) with an Alexa Fluor™ 568 secondary (Invitrogen, Carlsbad, California, 1:500) and anti-isolectin B4 antibody conjugated to fluorescein (Vector Laboratories, Newark, California, 1:75), alongside an anti-collagen I antibody with an Alexa Fluor™ 647 secondary (Invitrogen, Carlsbad, California, 1:500). Tissue sections were visualized using a Nikon Eclipse Ti2-E fluorescent microscope. For quantification of vessels, arterioles were identified by a positive co-stain of both αSMA and isolectin B4, and only arterioles with clearly defined and cross-sectional lumens were quantified. Arteriole density was quantified with respect to the scar area per tissue section, and arteriole lumen area was traced using the interior

border of endothelial stain for each vessel. All tissue sections containing scar were analyzed, and data were averaged per animal.

2.5.5 RNA Isolation, Nanostring Multiplex Gene Expression Analysis, and Bulk RNA Sequencing

2.5.5.1 Study design and RNA isolation

Two weeks after partial glossectomy injury, either 300 µL of SKM or Saline was injected into the injury site (n=6/group). 300 µL injection volume was chosen based on histological data, and the control saline injection was increased to 300 µL to match SKM. An injured non-injected group was used as an additional control to further evaluate potential effects of the injection itself. At 3 and 7 days post-injection, physiologically relevant timepoints for the immune response and early muscle regeneration, tongues were harvested and submerged in RNAlater™ (Thermo Fisher Scientific, Waltham, MA, then stored at 4°C overnight before being transferred to −80°C to preserve tissues for RNA isolation. For RNA isolation, tongue specimens were thawed and tissue was trimmed to isolate the scar region. Isolated scar region was divided in half, to accommodate spin column capacity, and homogenized (TissueRuptorII, Qiagen, Germantown, Maryland), and RNA was isolated with RNAeasy Fibrous Tissue Mini Kit following manufacturer instructions (Qiagen, Germantown, Maryland).

2.5.5.2 NanoString multiplex gene expression analysis

As previously described,[38] we used a NanoString nCounter ® MAX Analysis System with an nCounter® custom CodeSet of 145 genes involved in pathways relevant

to skeletal muscle regeneration.[38] Briefly, RNA concentration was measured using a Qubit 3.0 Fluorometer with a Qubit™ RNA HS Assay kit. The hybridization buffer (70 µL) was then mixed with the Custom Reporter CodeSet solution, and 8 µL of this master mix was then added to 50-100 ng of RNA per tissue sample, and RNA-free water up to 13 µL total. Then, 2 µL of Capture ProbeSet was added to the mixture, thoroughly mixed and placed on a thermocycler at 65°C for 16-48 hours and then maintained at 4°C for less than 24 hours. Using a two-step magnetic beads purification, probe excess was removed in PrepStation and target/probe complexes were bound on the cartridge. The data were collected by the digital analyzer (NanoString nCounter® Digital Analyzer) with images of immobilized fluorescent reporters in the sample cartridge. Results of barcode reads were analyzed by nSolver™ Analysis Software 4.0, and differential expression analysis was done with a custom R script.

The NanoString data were analyzed using ROSALIND, a cloud-based software pipeline supported by NanoString for analysis of nCounter data. Comparisons between SKM and saline, and SKM and non-injected groups were analyzed for each timepoint, with addition of covariate analysis for assay run data as necessary. Data were visualized with volcano plots using the EnhancedVolcano package in R.

2.5.5.3 Bulk RNA Sequencing

Purified mRNA was analyzed using a TapeStation 2200 with a high-sensitivity RNA ScreenTape. After the RNA-integrity number (RIN) was confirmed to be adequate, the RNA was processed using the Illumina Stranded mRNA kit. Libraries were quantified via a Qubit 3.0 and fragment size was determined using a TapeStation 2200 with a D5000

ScreenTape. Libraries were then sequenced on a NextSeq 2000 at depth of 75 x 2. Differential expression analysis was done using the Bioconductor DESeq2 pipeline.

2.5.6 Histological Characterization at Early Timepoints Post-Injection

2.5.6.1 Hematoxylin & Eosin staining of early timepoint tissues.

Two weeks after partial glossectomy injury, either 200 or 300 µL of SKM was injected into the injury site. At 3 and 7 days post-injection, tongue tissues were harvested and cryosectioned. Tissue sectioned were stained with hematoxylin & eosin to assess area of injury, defined by hypercellularity and muscle damage. The area of injury was outlined and normalized to the total tissue area for the section; this percentage of injured area was then compared between groups.

2.5.6.2 Quantification of arteriole density.

Tissue sections from 7 days post-injection for SKM and saline groups were stained against an anti-αSMA antibody and anti-isolectin B4 as previously described (Section 5.4.3). One tissue section was assessed per animal, chosen as the most injured section defined by greatest cellularity. Arteriole density was defined as number of arterioles normalized by the total tissue area and was statistically compared between groups with an unpaired t-test. Furthermore, the distribution of arteriole lumen areas between groups was compared.

2.5.6.3 Immunohistochemical staining of fibroadipogenic progenitors and developing myofibers

To assess FAP localization in the context of scar area, myofibers, and SKM bolus, an anti-PDGFRα antibody (R&D Systems, Minneapolis, MN, 1:100) with Alexa Fluor™ 568 secondary (Invitrogen, Carlsbad, California, 1:500) was used alongside an anti-collagen I antibody (AF488 secondary), anti-α-sarcoglycan antibody (AF647 secondary), and DAPI as previously described. To assess new and developing myofibers, an anti-embryonic myosin heavy chain antibody (Developmental Studies Hybridoma Bank, Iowa City, Iowa, 1:200) with Alexa Fluor™ 488 secondary was used alongside an anti-α-sarcoglycan antibody (AF568 secondary) and DAPI as previously described. Tissue sections were visualized using an Olympus VS200 fluorescent microscope. To assess density of FAPs within the injured area, which was defined as the region demonstrating disrupted muscle and hypercellularity, the QuPath positive cell detection tool was used to detect cells and define a positive cell as one containing PDGFRα signal within the cytoplasm area of a cell. The number of PDGFRα$^+$ cells was normalized by the total number of nuclei within the injured area.

2.5.7 Statistical Analysis

The initial SKM dosing study was a pilot study that did not aim to achieve statistically significant differences, so n=2 animals per injection volume were used for this initial investigation. For the investigation of histomorphological changes following SKM injection, sample size was based on a previous study of SKM for muscle regeneration in a model of hindlimb ischemia;[42] using G*Power, 6 animals/group were needed to achieve

90% power and a significance of 0.05. For gene expression studies, preliminary data with qRT-PCR were used to calculate the sample size; 11 animals/group/timepoint were necessary to achieve 80% power and a significance of 0.05. Data that followed a parametric distribution were compared using a Student's t-test, or a one-way analysis of variance followed by Tukey's post hoc pairwise comparisons. Data that did not follow a parametric distribution (skeletal muscle cross-sectional fiber area, arteriole lumen area) were analyzed by Mann-Whitney test.[38] Data were analyzed using GraphPad Prism v8.0, San Diego, CA. Gene expression normalization and differential expression was analyzed using the ROSALIND pipeline, with a fold-change cutoff of 1.2 and p-value cutoff of 0.05. For bulk RNA sequencing, differentially expressed genes were identified as average absolute logFC > 0.6 and adjusted p-value < 0.1.

2.6 Acknowledgements

This research was funded in part by the Galvanizing Engineering in Medicine funding through UC San Diego's Altman Clinical and Translational Research Institute and the Institute of Engineering and Medicine. The authors would like to thank the Stem Cell Genomics Core at the Sanford Stem Cell Institute for providing sequencing services.

Chapter 2, in part, is a reprint of the material as it appears in Bioactive Materials 2024. Emma I. Zelus, Aaron Panduro, Isha Deshmukh, Jacqueline Grime, Marianna Alperin, Andre M. Vahabzadeh-Hagh, Karen L. Christman. The dissertation author was the primary researcher and author of this paper.

Chapter 3: Development of a Translationally Relevant Preclinical Model of Stress Urinary Incontinence and Preliminary Investigation of Extracellular Matrix Hydrogel Treatment

3.1 Introduction

Stress urinary incontinence (SUI) is defined as the involuntary loss of urine due to increased intrabdominal pressure, typically manifesting as an involuntary leak in response to a cough, sneeze, laugh, jump, or other similar events. Approximately 25-50% of women are affected by SUI in their lifetime,[93–95] and SUI is known to have a profound negative effect on women's quality of life.[96] Despite the widespread incidence and severe impact to quality of life of SUI, there are currently no treatments that address the underlying pathophysiology of SUI.

It has been well established that vaginal delivery, especially multiple vaginal deliveries, are one of the primary risk factors for developing SUI, alongside age and obesity.[97] Approximately 1/3 of women develop SUI within 1 year after vaginal delivery, and while some of these women may recover urethral function, they are still at risk for development of chronic SUI later in life.[98–102] In fact, the 15 year cumulative incidence of SUI after the first vaginal delivery is approximately 34%. The voluntary urethral continence mechanism relies upon the function of the external urethral sphincter (EUS) comprised of skeletal muscle, the pelvic floor muscles that support the urethra, and the associated nerves.[103,104] Multiple studies have established that damage to the EUS during vaginal delivery is the primary initial cause of SUI.[105–107] However, the mechanisms by which vaginal delivery-induced birth injury damage the EUS and compromise urethral incontinence are complex and multifaceted. Different groups have demonstrated that

vaginal delivery leads to mechanical overstretching of skeletal muscle fibers within the EUS, a hypoxic environment due to compression of the urethral structures by the fetal head, and nerve damage. In particular, our lab has previously demonstrated that in a rat model of simulated birth injury (SBI, Figure 3.1A), which is well established to mimic the pathophysiologic changes in the pelvic floor that occur as a result of childbirth injury, birth injury leads to disruption of muscle fiber organization and architecture (Figure 3.1B) as well as sarcomere hyperelongation (Figure 3.1C).[108]

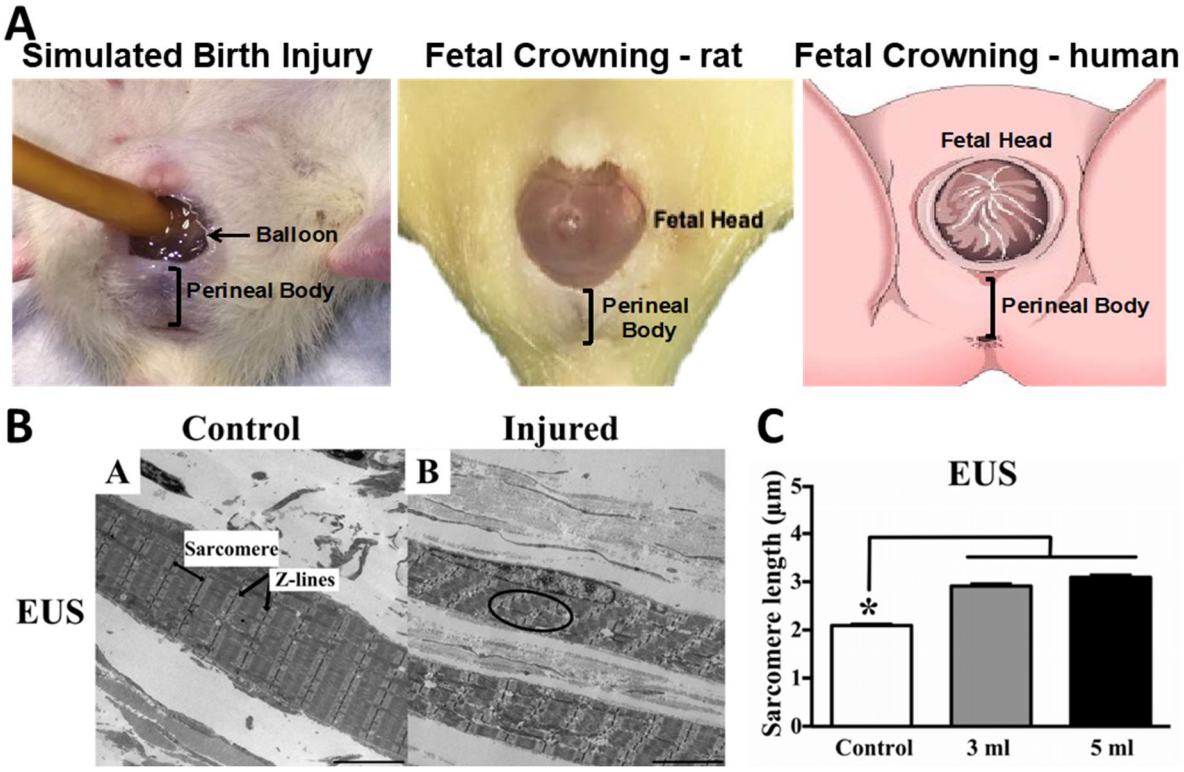


Figure 3.1 Vaginal distention simulates childbirth injury and results in damage to the external urethral sphincter

(A) Visualization of simulated birth injury (SBI) procedure, mimicking fetal crowning, which causes the greatest strains to the pelvic floor and resulting childbirth injury. (B) Transmission electron micrograph showing disruption of skeletal myofibril organization within the external urethral sphincter (EUS) after SBI. (C) SBI with a vaginal distention of either 3 or 5 mL leads to sarcomere hyperelongation in the EUS, indicating overstretch injury of the EUS muscle resulting from childbirth injury.
Figure adapted with permission from Duran et al. *Neurourol Urodyn.* 2019.

Despite the body of research demonstrating that skeletal muscle injury due to vaginal delivery is one of the primary drivers of SUI development, current treatments are compensatory in nature and do not address the underlying pathophysiology of SUI. Procedural interventions, such as midurethral slings, are invasive in their approach and only serve to supply external pressure on the urethra. Urethral bulking injections (Bulkamid®, Contigen®, Macroplastique®, and others) are synthetic or bovine collagen materials that are delivered via periurethral injection to the proximal urethra and bladder neck region in order to narrow the urethral opening and improve urethral closure pressures. As a regenerative intervention approach, injections of mesenchymal, adipose, and muscle-derived stem cells have been tested both preclinically and clinically for restoration of EUS to improve urethral function.[109,110] These studies have shown some promising results, demonstrating the potential for EUS regeneration to treat SUI, but pose significant translational and manufacturing challenges.

The current standard of care for SUI clinically has demonstrated safety and feasibility of periurethral injections, and stem cell injections, while early in development, have shown that targeting the EUS with a tissue regenerative therapeutic can yield improvements in EUS and urethral function. As an alternative to the biomaterials and cell therapies currently in use and under investigation, we propose to utilize a decellularized extracellular matrix (ECM) hydrogel for regeneration of the EUS and restoration of continence in application for SUI.

The use ECM hydrogels, which are known to induce immune modulation, cellular recruitment and differentiation, neovascularization, and ECM remodeling, has been explored as a therapeutic in numerous disease phenotypes.[25] The ECM is a complex

network of proteins and polysaccharides vital for structural support and cell signaling; when a whole tissue is decellularized, the ECM remains as an acellular biomaterial with tissue regenerative properties.[25] Additionally, due to their thermoresponsive properties, ECM hydrogels, formed via partial enzymatic digestion of decellularized ECM, can be delivered minimally invasively via injection, and after exposure to physiologic conditions, the liquid forms a scaffold comprised of a nanofibrous ECM network.[68] With sufficient decellularization, the acellular xenogeneic ECM hydrogels are biocompatible and have been utilized in large[69,70] and small animal models,[71] as well as a human Phase 1 clinical trial that assessed safety and feasibility for intervention in subacute and chronic myocardial infarction.[26] We have previously demonstrated that a decellularized porcine skeletal muscle ECM hydrogel (SKM) increased vascularization, enhanced the recruitment and differentiation of muscle progenitors, and reduced muscle atrophy and cell death in an ischemic injury model.[35,42,68] SKM has further been shown to prevent skeletal muscle atrophy and mitigate fibrotic degeneration, as well as modulate the immune response after mechanical muscle injury in pelvic floor muscles.[38] Thus, we hypothesize that the SKM hydrogel will stimulate tissue regeneration of the EUS and restore urethral function to treat SUI.

3.2 Results

3.2.1 Single SBI model of SUI

To assess the therapeutic potential of SKM injection for regeneration of the EUS and improvement of urethral function, it was first necessary to establish a suitable preclinical and translational model of SUI in the rat. Our lab previously demonstrated that a longitudinal study design, in which young female rats underwent a single SBI and were

followed up for urethral function measurements via LPP for up to 4 weeks, produced a consistent deficit in urethral function and model of SUI due to birth injury in the rat. With the goal of assessing the SKM hydrogel as a therapeutic, we first aimed to validate this single SBI model of SUI.

In the first two rounds of study, for which the timelines are shown in Figure 3.3A, the experimental protocol previously established in the lab was repeated. 3 month old female Sprague Dawley rats underwent LPP testing to establish a healthy baseline urethral functional measurement for each animal. Immediately after, animals underwent SBI with a vaginal distension volume of 5 mL for two hours. After completing SBI, LPP was again tested to find the acute post-SBI urethral functional measurement, and follow-up LPP measurements were taken for each animal weekly out to 4 or 5 weeks post-SBI. Results for each individual animal's LPP measurements at each timepoint are shown as lines with different colors in Figure. 3.3C and D. Of the 7 animals tested in the first two rounds of study, only 4 maintained a deficit in urethral function and thus constituted a model of SUI.

This study was repeated with a slightly different experimental scheme, described in Figure 3.3B, in which baseline LPPs were taken the day prior to SBI, and the acute LPP was taken the day following SBI. This timeline was shifted to more accurately reflect the urethral function in LPP measurement, as the SBI can cause exaggerated responses, and to enable a more efficient experiment and higher sample sizes. LPP data for this new experimental scheme is shown in Figure 3.3F, in which each colored line represents a different animal subject. In this round, all animals displayed a significant decrease in LPP compared to their healthy baseline even out to 8 weeks post-SBI, representing successful

establishment of a model of SUI. While the results of this final round of study were encouraging, when taking all three rounds together, as shown in Figure 3.3F, it is evident that the single SBI model is inconsistent in producing a SUI phenotype in rats.

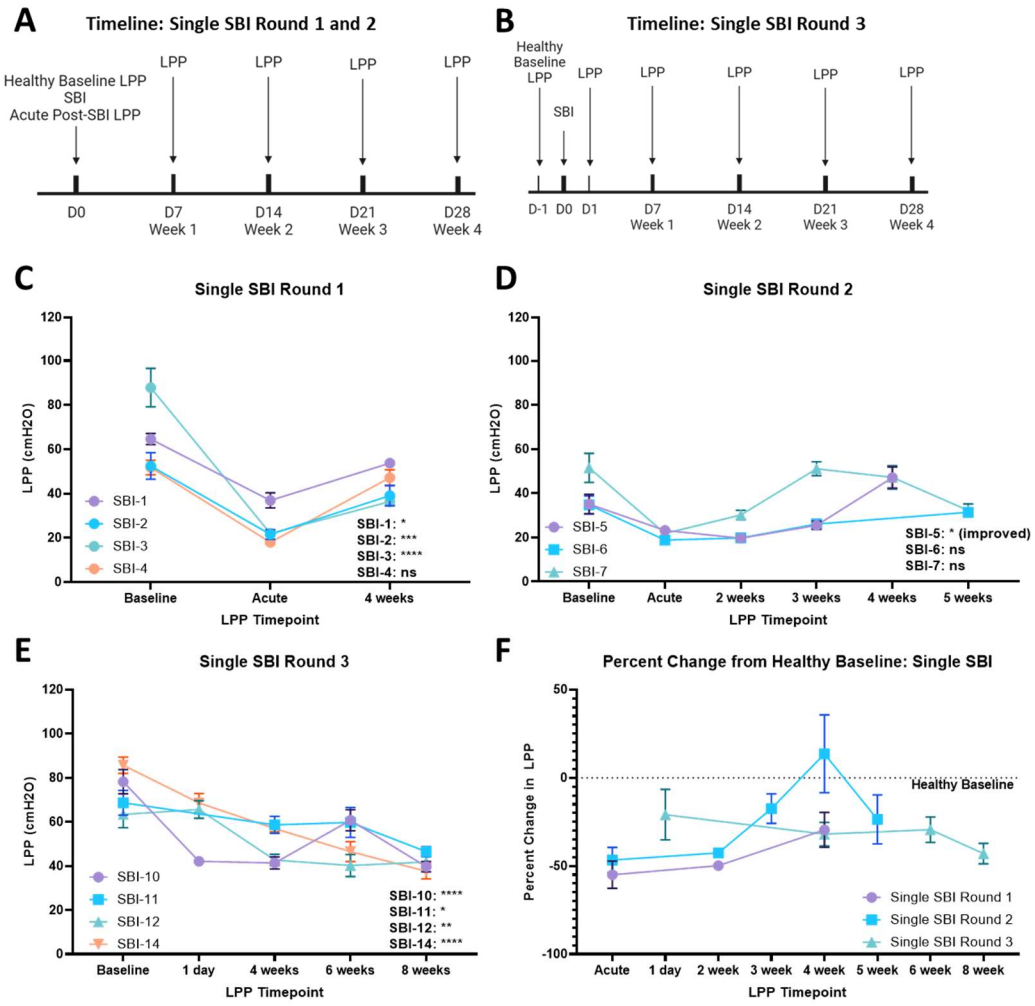


Figure 3.2 Single SBI injury model produces divergent results, with inconsistent establishment of urethral function deficit.

Experimental timelines for single SBI model of SUI are shown for rounds 1 and 2 (A) and round 3 (B). LPP data for all timepoints shown are shown, with each colored line representing a different animal, for round 1 (C), round 2 (D), and round 3 (E). Results of statistical comparison between the endpoint LPP measurement and healthy baseline LPP measurement are shown for all animals. (F) For all animals, data were normalized as a percentage change in LPP from their healthy baseline. Summarized data across all timepoints and for all 3 founds of study are shown.

3.2.2 Repeated SBI model of SUI

With previous results showing that the single SBI model does not produce a consistent SUI phenotype in rats, we sought to establish a more severe or consistent model of SUI while remaining within physiologically relevant parameters. As multiparity is known to be a significant risk factor for development of SUI, we tested a repeated SBI model in the rat, which consisted of 3 SBIs taking place over a course of 6 weeks. As shown in the timeline in Figure 3.4A, LPP measurements were taken 1 day prior to and 1 day following each SBI, and after the final SBI, LPP measurements were taken weekly for an additional 4 weeks.

In Figure 3.4B, each colored line represents the LPP measurements at each timepoint for an individual animal. By the final timepoint, 4 weeks after the 3rd SBI, only 3 of the 5 animals maintained a significant deficit in urethral function; there was a 40% recovery rate in these animals. The overall trend in urethral function of these animals, shown in Figure. 3.4C, was not notably different from the single SBI model shown previously despite the notable increase in injury stimulus.

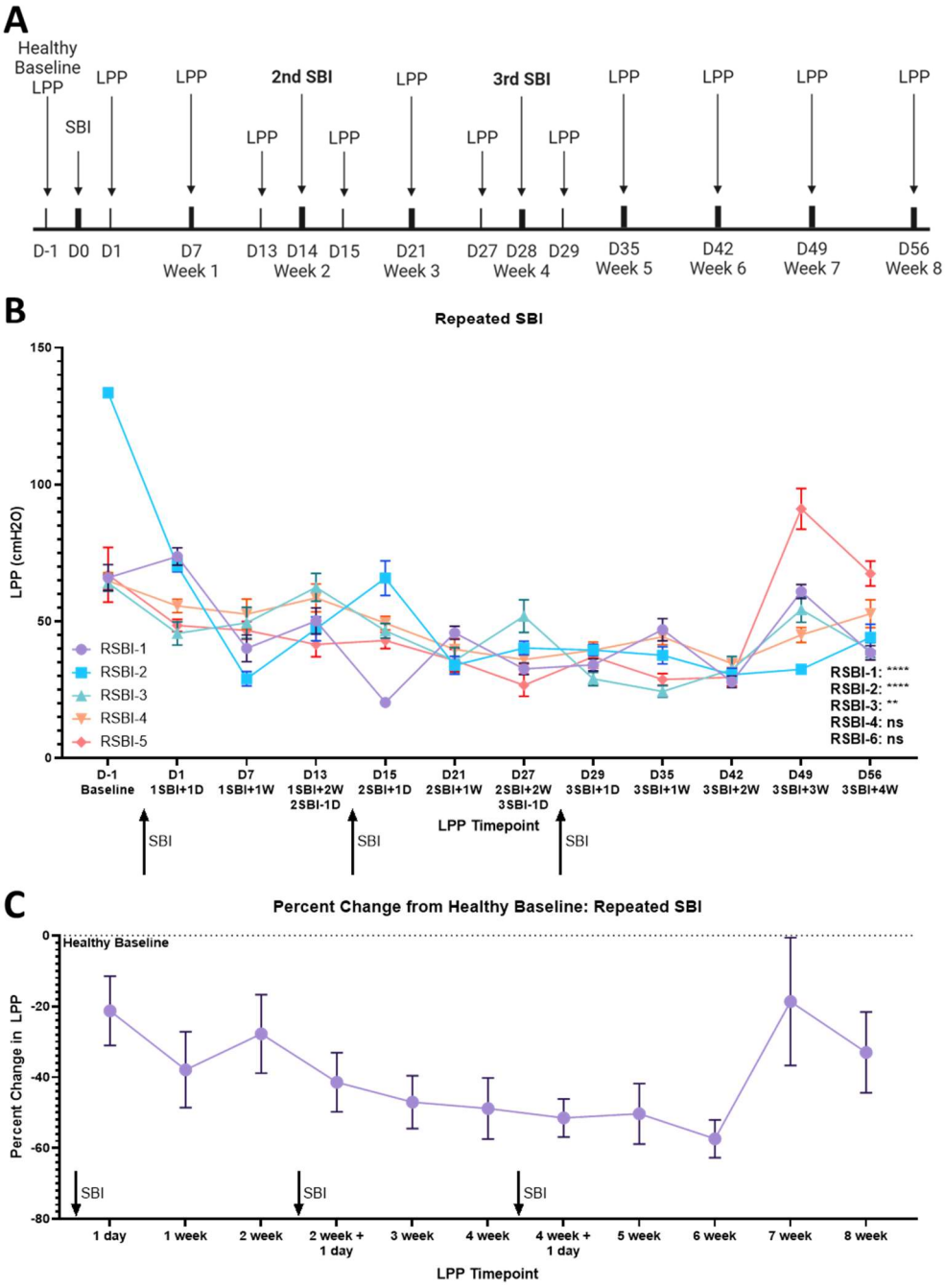


Figure 3.3 Repeated SBI injury model does not produce consistent urethral function deficit

(A) Experimental timeline for repeated SBI model of SUI. (B) LPP data for individual animals are shown as different colors. Results of statistical comparison between the endpoint LPP measurement and healthy baseline LPP measurement are shown for all animals. (C) For all animals, data were normalized as a percentage change in LPP from their healthy baseline, and the summarized data were graphed across all timepoints.

3.2.3 Retired Breeder model of SUI

As neither single nor repeated SBI models produced a consistent phenotype of SUI in young female rats, we pursued a model utilizing retired breeder rats. These rats are aged, approximately 7-9 months, and have undergone multiple pregnancy and birth cycles, which would physiologically emulate the clinical population of aged multiparous women who experience SUI. As shown in the timeline in Figure 3.5A, retired breeder rats underwent baseline LPP measurements 1 day prior to SBI, and additional LPP measurements were taken 1 day as well as 1, 2, 3, and 4 weeks post-SBI.

In Figure 3.5B, each colored line represents the LPP measurements at each timepoint for an individual animal. At 4 weeks post-SBI, all but 1 animal had recovered to their baseline healthy LPP values, giving this model an 80% recover rate. This is further shown in Figure 3.5C, in which the general trend of urethral function returns to healthy baseline values. As such, the retired breeder SBI model was deemed ineffective for eliciting a SUI phenotype in rats.

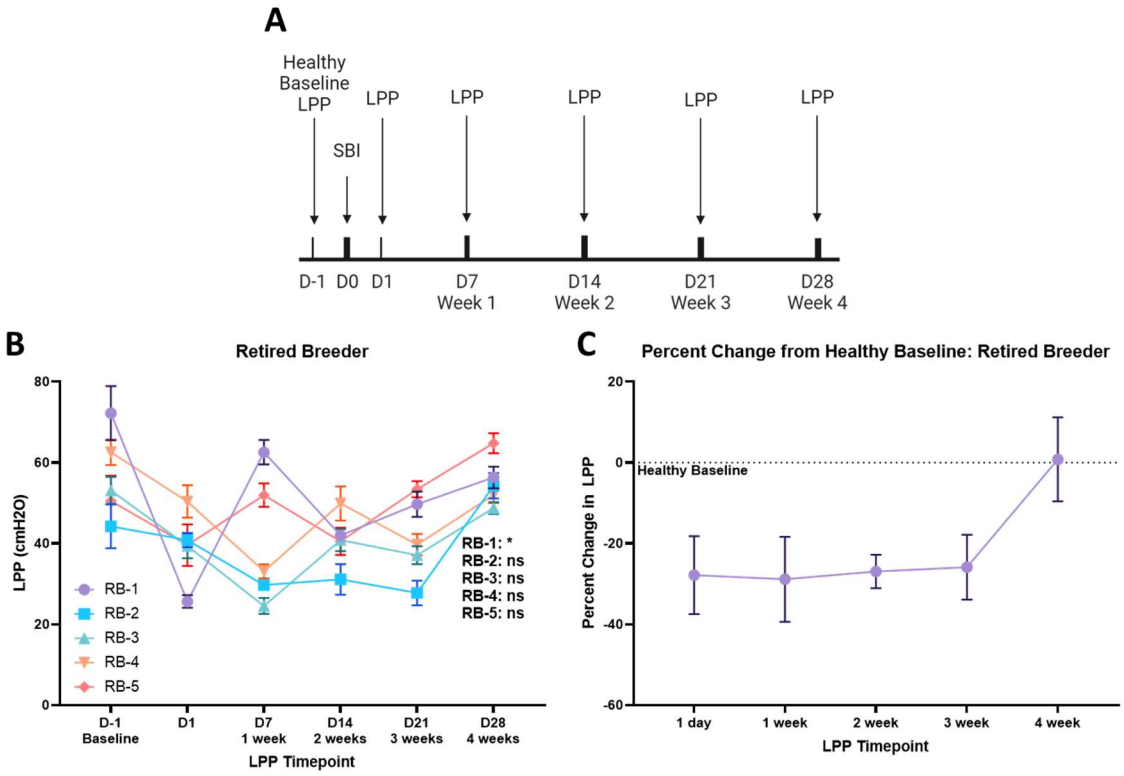


Figure 3.4 Retired Breeder injury model is insufficient for establishing stress urinary incontinence phenotype

(A) Experimental timeline for retired breeder model of SUI. (B) LPP data for individual animals are shown as different colors. Results of statistical comparison between the endpoint LPP measurement and healthy baseline LPP measurement are shown for all animals. (C) For all animals, data were normalized as a percentage change in LPP from their healthy baseline, and the summarized data were graphed across all timepoints.

3.2.4 Ovariectomy model of SUI

As previous literature has suggested a combinatorial effect of menopause and multiparity on development of SUI, we explored the combination of ovariectomy and SBI for establishing a model of SUI in the rat. As shown in the timeline in Figure 3.6A, young female Sprague Dawley rats underwent ovariectomy to produce a surgical model of menopause, and baseline healthy LPPs were acquired two weeks post ovariectomy. Animals then underwent SBI and follow-up LPPs at 1 day and 1, 2, 3, and 4 weeks post

SBI. At the 4 week timepoint, it was determined that animals had already recovered to baseline LPP values; as such, an additional SBI was performed at the 4 week timepoint to increase the injury stimulus. Animals were followed up for LPP measurement 6 weeks after the 2nd SBI, and the data for each animal is shown in a different color in Figure 3.6B. While the sample size for this group was smaller, even with ovariectomy and two SBI, we observed a 33% recover rate for this model. The data combined, as shown in Figure 3.6C, again do not show substantial differences from the original single SBI model in terms of consistency or severity of SUI phenotype.

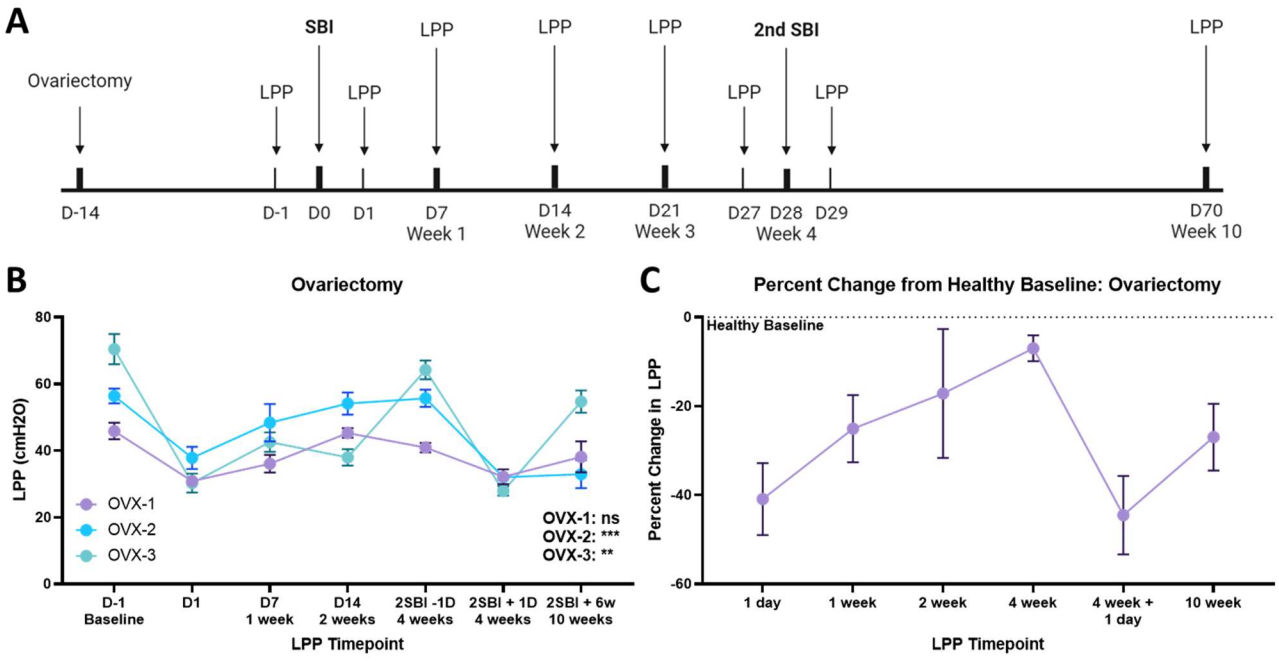


Figure 3.5 Ovariectomy with repeated injury produces a relatively more consistent model of urinary incontinence at the cost of experimental duration

(A) Experimental timeline for ovariectomy model of SUI. (B) LPP data for individual animals are shown as different colors. Results of statistical comparison between the endpoint LPP measurement and healthy baseline LPP measurement are shown for all animals. (C) For all animals, data were normalized as a percentage change in LPP from their healthy baseline, and the summarized data were graphed across all timepoints.

3.2.5 Correlation of functional data with skeletal muscle sphincter morphology in models of SUI

For all models of SUI tested thus far (single SBI, repeated SBI, retired breeder, and ovariectomy), urethral tissues were fixed, frozen, and cryosectioned for histomorphological analysis. Specifically, the skeletal muscle sphincter area was assessed, as literature suggests that the external urethral sphincter (EUS) is primarily injured during vaginal delivery and may contribute to the development of SUI in parous women. For all SUI model groups as well as healthy control animals, five sections containing the EUS were analyzed per animal. Tissue sectioned were stained against myofibers, and the area of the EUS was normalized to the area of the urethral lumen for each section. As shown in Figure 3.7A, both the retired breeder and ovariectomy groups demonstrated significantly higher EUS areas compared to controls, while single and repeated injury were no different from controls. As a further validation of this measurement, the area of positively stained myofiber signal was normalized to the lumen area for each section. In this analysis, only the ovariectomy group demonstrated significantly higher skeletal muscle area as compared to controls, while all other groups were not significantly different from controls (Figure 3.7B). The discrepancy between these analyses may be explained by the reduced EUS myofiber density, as shown in Figure 3.7C, in which the retired breeder group demonstrates a nonsignificant decrease in the percentage of EUS area which is occupied by myofibers.

These histological results demonstrate that there is no decrease in EUS or skeletal muscle area in the urethra in any of the SUI models tested; in fact, some groups have an even larger EUS or skeletal muscle area compared to controls. The functional data

acquired, shown in Figure 3.7D, demonstrates that single SBI, repeated SBI, and ovariectomy models all resulted in similar functional deficits, while the retired breeder group recovered to healthy baseline. When correlating these functional and histological findings (Figure 3.7E), we find that although some groups – specifically the single and repeated SBI – cluster together in their relationship between LPP measurements and skeletal muscle sphincter area, there is overall no relationship between urethral function and EUS area. A linear regression was applied to these data, and the slope was determined to be not significantly nonzero, with an overall extremely weak correlation coefficient of 0.122. These data, while surprising, suggest that, at least in the rat, urethral functional measurements do not correlate with EUS morphology.

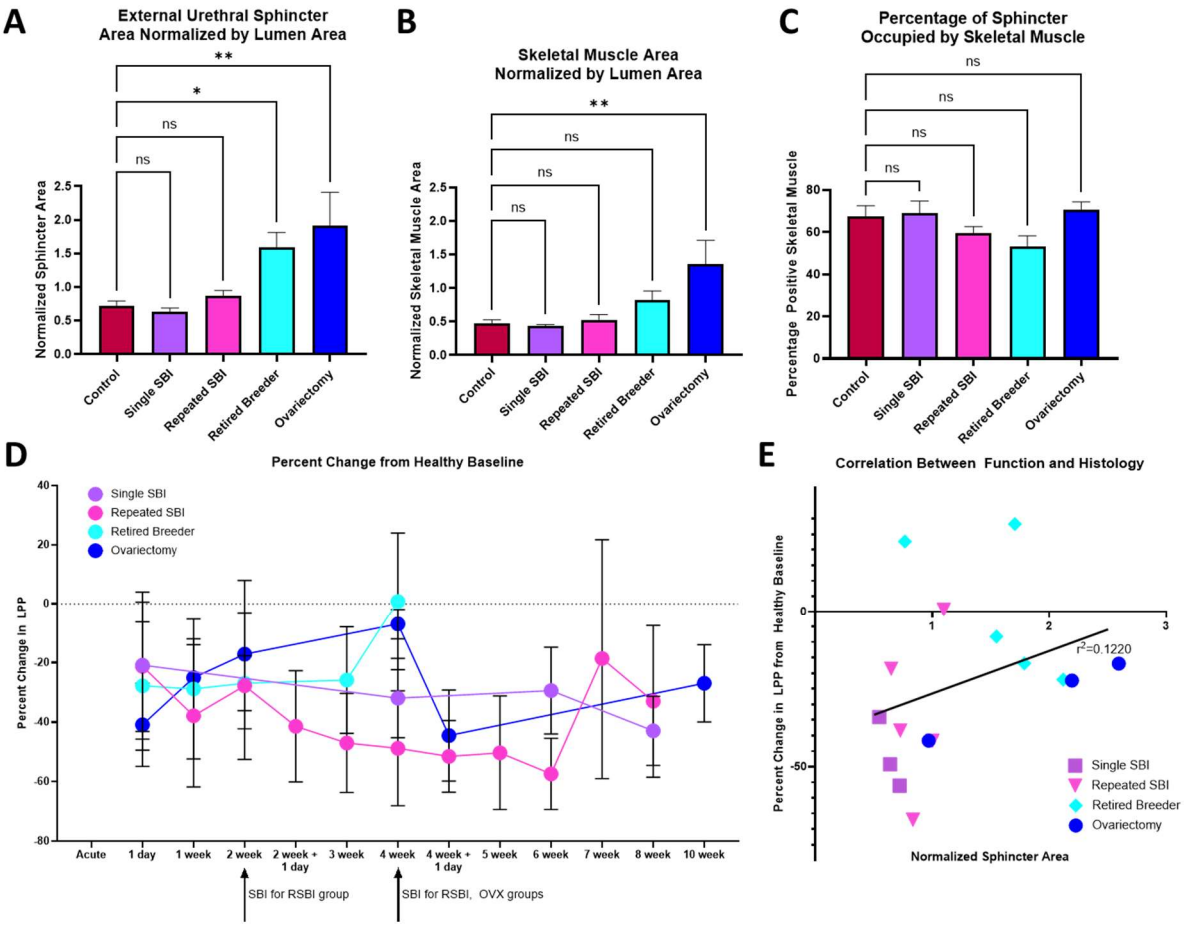


Figure 3.6 Histological assessment of external urethral sphincter and correlation between histological and functional data in models of stress urinary incontinence

(A) For all SUI model groups and an additional healthy control group, 5 sections from all animals were assessed for EUS area, which was normalized by lumen area per section. Results per section were averaged to produce a data point for each animal. (B) Similarly, area of positively stained skeletal muscle was assessed for each section and normalized by lumen area. (C) The density of skeletal muscle within the EUS was quantified by normalizing the area of positively stained skeletal muscle by the EUS area. (D) LPP data, represented as percent change in LPP from the healthy baseline per animal, among all SUI model groups was combined, demonstrating urethral function trends. (E) For each animal, the percent change in LPP from healthy baseline at the final timepoint was plotted against that animal's normalized EUS area to assess whether there was a correlation between urethral function and EUS morphology.
EUS morphological data were collected by Danna Du.

3.2.6 Choosing a model of SUI for evaluation of potential therapeutics

With our ultimate goal being to design an acellular biomaterial therapeutic for treatment of SUI, we assessed all the models studied thus far for their potential in preclinical therapeutic studies. As shown in Table 3.1, the single SBI and ovariectomy model groups had similar recovery rates – 36% and 33% respectively – with the repeated SBI group not much higher at a 40% recovery rate. The retired breeder model was by far the least effective model for SUI, with an 80% recovery rate. Among the other three models, which had similar consistency in establishing the SUI phenotype in rats, the single SBI model is the most cost-effective and least laborious model. Thus, for subsequent studies investigating the therapeutic efficacy of an SKM hydrogel injection for treatment of SUI, we utilized the single SBI model to establish SUI.

Table 3.1 Summary of SUI models tested and their recovery rates

Rat Vendor and Strain	Condition	# SBIs	# Animals Recovered % Recovery
Envigo Sprague Dawley	Young adult	1	4/11 36%
Envigo Sprague Dawley	Young adult	3	2/5 40%
Envigo Sprague Dawley	Retired Breeder	1	4/5 80%
Charles River Labs Sprague Dawley	Ovariectomized	2	1/3 33%

3.2.7 Optimization of EUS injection volume and retention of SKM in the EUS

The literature for delivery of injectable materials (biomaterials, cells, etc.) to urethral tissues in the rat is extremely divisive and variable, with groups describing injection volumes ranging from 10 µL (SOURCE) to 300 µL (SOURCE). The rat urethra

is an extremely delicate and small tissue, with a length of approximately 15 mm and a typical urethral wall thickness of less than 500 μm. Thus, we deemed it necessary to first conduct an experiment to assess the maximal safe and feasible injection volume targeting the urethral EUS.

In young female uninjured Sprague Dawley rats, 20 μL injections were performed twice (total injection volume of 40 μL, one on each side of the urethra, delivering either saline, collagen, or SKM to the urethral EUS (n=3/injection group). Additional animals received a “dry” injection, in which the injection procedure was identical but not material was delivered through the syringe (n=3). Animals were survived for one week post-injection and observed for adverse events. In all injection groups (saline, collagen, and SKM), adverse events were observed, including blood in the urine, sediment in the urine, swelling of the urethra and/or bladder, or bladder stones. No adverse events were observed in the dry injection group.

At the one week post-injection timepoint, animals were euthanized, and urethral tissues were harvested for histomorphological analysis. As expected, based on the adverse events observed, the urethral tissues of all groups (saline, Figure 3.7B; collagen, Figure 3.7C; and SKM, Figure 3.7D) that received a 20 μL injection demonstrated aberrant morphology in comparison to the dry injection (Figure 3.7A) which was no different from uninjured control tissues (not pictured). Aberrant morphological features included hypercellularity, significant swelling of the urethral wall, and unusual distortion of tissue structure (particularly in collagen, Figure 3.7C). Based on these observations, we concluded that the 20 μL injection volume was not safe or feasible.

We next tested injection volumes of 10 and 15 μL, each of which were administered twice, once on each side of the urethra, for a total volume of 20 or 30 μL, respectively. For this experiment, only SKM was tested, as it was determined previously that there was no difference in adverse effects or histomorphology between SKM, collagen, and saline injected groups. The SKM material was fluorescently pre-labeled, with a different fluorophore used for each injection side, to enable assessment of material retention. Animals were survived for one week post-injection of either 10 or 15 μL SKM (n=3/group). No adverse events were observed in animals from either group. Urethras were harvested and assessed for tissue morphology with H&E, and both 15 μL SKM (Figure 3.7E) and 10 μL SKM (Figure 3.7F) groups demonstrated normal urethral morphology, no different from dry injection or healthy and unperturbed controls.

Urethral tissues from 15 μL (Figure 3.7G) and 10 μL (Figure 3.7H) SKM injection groups underwent immunohistochemical staining against skeletal muscle (green) and nuclei (blue). The fluorescently prelabeled SKM from both injection sides (red and cyan) is observed directly adjacent and within the urethral EUS, demonstrating good localization and targeting of the SKM via injection. Additionally, both injection volumes demonstrated good retention at the one week post-injection timepoint. Given these observations, the 15 μL injection volume was chosen to proceed with a pilot efficacy study in order to maximize dosage of SKM and the potential therapeutic response.

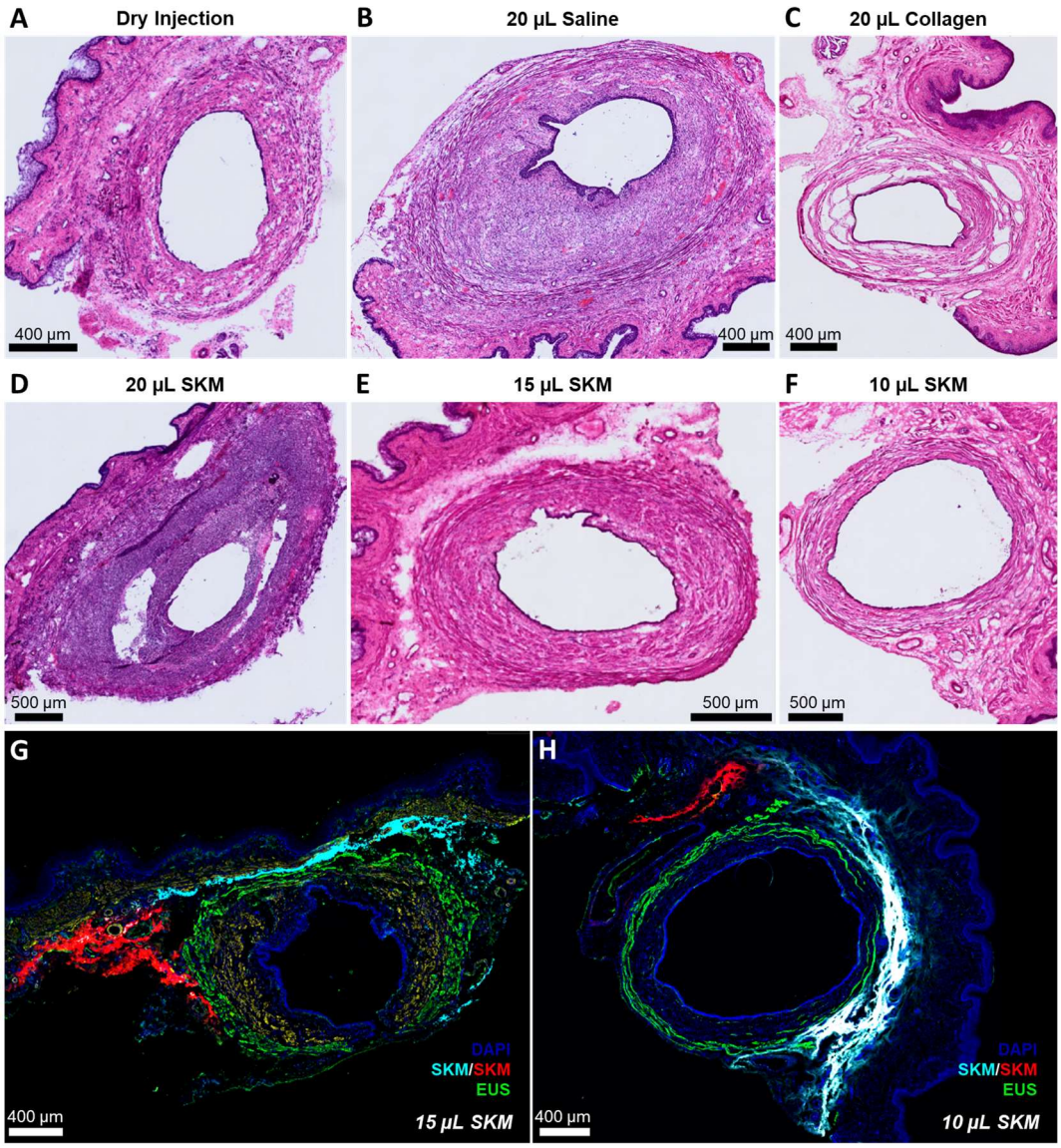


Figure 3.7 Urethral morphology after injection of different materials to the EUS and retention of SKM in the EUS

Healthy, unperturbed young female Sprague Dawley rats underwent urethral injections of various materials and urethral tissues were harvested 1 week post-injection for evaluation of urethral histomorphology via hematoxylin and eosin staining. Representative images are shown for injection of no material (A), 20 µL saline (B), 20 µL collagen (C), 20 µL SKM (D), 15 µL SKM (E), or 10 µL SKM (F). Fluorescently prelabeled SKM (cyan, red) was injected to the EUS, and urethral tissues were harvested 1 week post-injection and stained for nuclei (blue) and skeletal muscle (green) to visualize SKM localization and retention for 15 µL (G) and 10 µL (H) injection volumes.
EUS morphological images and injection optimization were performed by Danna Du.

3.2.8 Injection of SKM hydrogel delivered to the EUS does not restore urethral function

In the single SBI model, we observed a more consistent deficit in urethral function after SBI alongside a smaller EUS area compared to other model groups, such as retired breeder and ovariectomy. This supports clinical studies, which have observed deficits in EUS muscle function through EMG in women following vaginal childbirth, and other studies have demonstrated the relationship between EUS muscle function and incidence of SUI (REFERENCE). Thus, we aimed to test the therapeutic potential of SKM hydrogel delivered via injection to the EUS for aiding muscle regeneration after SBI and improving urethral function.

Young female Sprague Dawley rats underwent LPP testing to establish healthy baseline urethral function, and the next day, all animals underwent SBI procedure, as seen in the timeline in Figure 3.8A. Two weeks after SBI, animals underwent LPP testing to assess the functional deficit; if the LPP at this timepoint was not significantly different from the healthy baseline for each animal, that animal was deemed recovered and excluded from further study. For those that did not recover, on the following day, animals were randomly assigned to receive EUS injections of 15 µL (for each side of the urethra) of either SKM (n=7) or saline (n=6). Additional follow-up LPP measurements were done for each animal at 2, 4, and 6 weeks post-injection (4, 6, and 8 weeks post-SBI).

LPP data for individual animals over the course of the study are shown for the saline group (Figure 3.8B) and SKM group (Figure 3.8C), which each colored line representing a different animal. In the saline group, all 6 animals demonstrated a significant deficit in urethral function at 6 weeks post-injection, 8 weeks post-SBI. In the SKM group, 5 of the 7 animals demonstrated a significant deficit in urethral at 6 weeks

post-injection, 8 weeks post-SBI; thus, 2 of the 7 animals demonstrated recovery of urethral function following injection. When considering injection group trends, in which each animal is normalized to its own health (Figure 3.8D) or injured (Figure 3.8E) baseline, there are no significant differences in urethral function recovery change between injection groups.

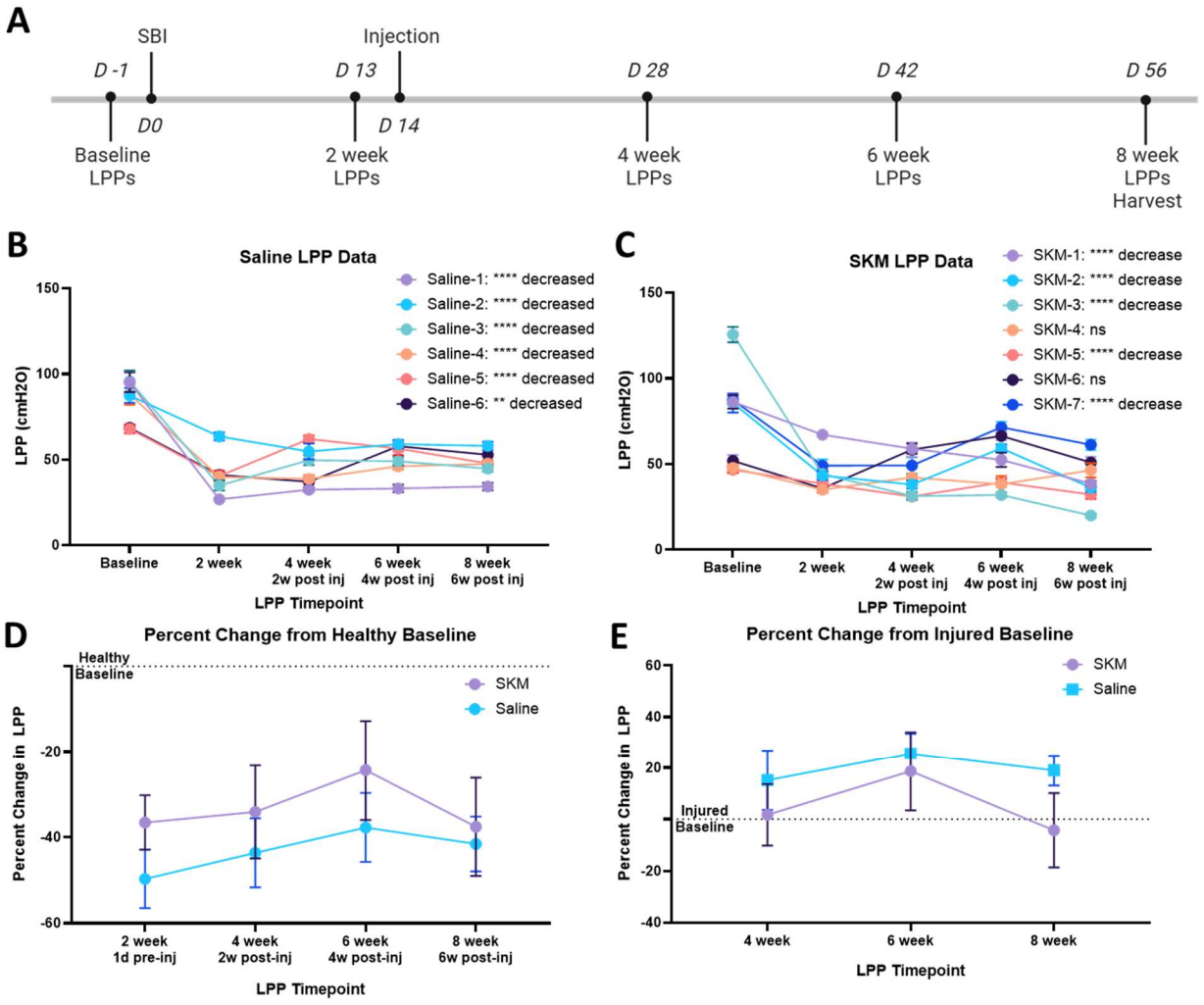


Figure 3.8 Urethral function following SKM or saline injection

(A) Experimental timeline for preliminary treatment study utilizing SKM or saline control injection in a model of SUI. LPP data for individual animals are shown as different colors, and results of statistical comparison between the endpoint LPP measurement and healthy baseline LPP measurement are shown for all animals from either saline injection group (B) or SKM injection group (C). (D) For all animals, data were normalized as a percentage change in LPP from their healthy baseline, and the summarized data were graphed across all timepoints for SKM and saline groups. (E) Similarly, LPP data for each animal were normalized as a percentage change in LPP from their injured (pre-injection) baseline, and the summarized data were graphed across all subsequent timepoints for SKM and saline groups.

3.2.9 Investigating the effect of SKM injection on EUS morphology

After the final LPP timepoint at 8 weeks post-SBI, urethral tissues were harvested, sectioned, and stained against nuclei (DAPI) and skeletal muscle (myosin heavy chain, MHC) to assess EUS morphology. Representative images for SKM (Figure 3.9A) and saline (3.9B) injected animals are shown, and quantitative comparison between groups yielded no significant differences in EUS area (Figure 3.9C).

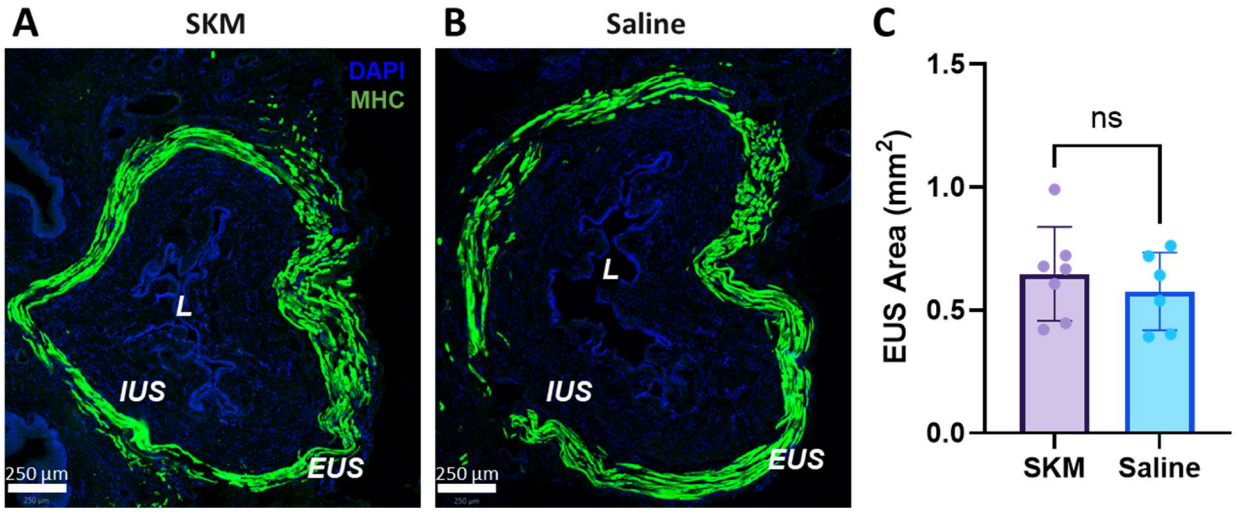


Figure 3.9 Skeletal muscle sphincter histomorphology following SKM or saline injection

Urethral tissues were isolated after the 8 week LPP timepoint, sectioned, and stained against skeletal muscle (MHC, green) and nuclei (DAPI, blue). Representative tissue sections, including labels for the urethral lumen (L), smooth muscle internal urethral sphincter (IUS), and skeletal muscle external urethral sphincter (EUS) are shown for SKM (A) and saline (B) injected groups. (C) Results for quantitative comparison of EUS area between groups.

3.3 Discussion

SUI is highly prevalent in woman who have undergone vaginal delivery, with both age and multiple deliveries increasing the risk of developing SUI. While the current body of research demonstrates that the likely mechanism underpinning the relationship

between birth injury and development of SUI, current treatments of SUI do not address this pathophysiology; instead, treatments are compensatory and only serve to increase urethral pressure. Some groups have investigated injection of various stem cell populations delivered to the EUS and demonstrated promising results, but cell therapies pose significant cost, manufacturing, and translational challenges. Thus, we aimed to investigate the therapeutic potential of a decellularized ECM hydrogel derived from skeletal muscle, previously used for tissue regeneration in a variety of skeletal muscle injury models, to regenerate the EUS and restore urethral function in a rat model of SUI.

However, the literature has demonstrated surprising inconsistencies in establishing a rat model of SUI which produces a deficit in urethral function at long time points. While our group and others have previously demonstrated sustained deficits in urethral function after single SBI, other groups have demonstrated that urethral function recovers within 4 weeks post-SBI. Indeed, our results show that approximately 30-40% of rats recover urethral function, determined by LPP, to healthy baseline after 4 weeks. More recent publications have demonstrated the potential of repeated birth injuries or a combinatorial model using both SBI and ovariectomy, yet the literature is still inconclusive. Upon testing models which replicated physiologic conditions under which women develop SUI – repeated SBI representing multiparous women, retired breeder representing the combination of age and birth injury, and ovariectomy representing the combination of menopause and multiparity – we found that none of these models demonstrated a consistent and sustained deficit in urethral function. Indeed, even the most reliable models – single SBI, repeated SBI, and ovariectomy – still had a 30-40% recovery rate. To develop novel tissue regenerative therapeutics for the treatment of SUI, it is vital to

have a preclinical model which reliably replicates the clinical pathophysiology of SUI – particularly, a chronic decrease in urethral function. As such, these data are vital for the scientific community, demonstrating the inconsistency of rat models of SUI and indicating the need for development of a more reliable model which yields a sustained deficit in urethral function.

Injections of materials, both acellular and cellular, in the rat urethra is subject to similar inconsistencies in the literature. For example, one group reports injection of 400 µL adipose-derived stem cells into the urethra,[111] while another group reports injection of 10 µL muscle-derived cells into the EUS.[112] Upon optimizing urethral injection volumes, for a scheme of two injections to the EUS on either side of the urethra, we found that anything above 15 µL for a single injection (30 µL total delivered to the EUS) caused significant negative outcomes in rats which were survived up to one week. Regardless of injection material (saline, collagen, or SKM), we found that two 20 µL injections resulted in urethral or bladder swelling, blood in the urine, sediment in the urine, or development of large bladder stones. These observations are typically associated clinically with urethral obstruction, leading us to conclude that injection volumes of more than 30 µL total delivered to the urethra are not safe or feasible for the rat.

Having established that all the tested models of SUI were similarly inconsistent, we proceeded with the single SBI model as a preclinical model of SUI in which to test our potential therapeutic, the SKM hydrogel. To address the poor reliability of the SUI model, animals were assessed for urethral recover relative to their healthy baseline at 2 weeks post-SBI, and if they recovered function, they were excluded from the present study. Given that two 15 µL injections yielded no adverse events and displayed similar

histomorphology to two 10 µL injections, we proceeded with the 15 µL volume to maximize potential therapeutic effect. In other applications in which SKM injection has been used to induce tissue regeneration following skeletal muscle injury, the SKM degrades over a period 3 weeks, and therapeutic outcomes are typically assessed 4-6 weeks following SKM injection. We assessed LPP of animals which received SKM or saline injection at 2, 4, and 6 weeks post-injection and found that SKM did not significantly improve urethral function recover as compared to saline. We additionally assessed EUS morphology at 6 weeks post-injection and found that SKM injection did no impact EUS area. Thus, SKM at this injection volume does not significantly improve urethral function in a rat model of SUI, and it does not significantly improve EUS regeneration.

The poor reliability of the animal model is a limitation of the current study, and further research must be done to establish a more consistent model of SUI. Additionally, the means of assessing urethral function in this study – LPP – may be less reliable than more recent methods that have been developed, such as urethral pressure profiling. In addition to inconsistencies within the literature regarding SUI model development in the rat, it is evident that there is conflicting information regarding the volume of material which is appropriate for injection in the EUS. While our initial study demonstrated no adverse events in the double 15 µL injection scheme, it is possible that this injection volume is deleterious to urethral continence mechanisms. As such, future studies should conduct additional assessments of the therapeutic efficacy of a double 10 µL or even 5 µL injection scheme. Additionally, the therapeutic efficacy of repeated EUS injections could be assessed.

3.4 Conclusion

In this study, we demonstrated that various models of SUI, which incorporate physiologically relevant variables such as birth injury, age, and menopause, are similarly inconsistent in induction of urethral function deficits in the rat. We additionally demonstrated that more than 30 µL volume injection delivered to the EUS is not safe or feasible for rats. Finally, we conducted a pilot study to assess the therapeutic potential of a decellularized skeletal muscle derived ECM hydrogel in a preclinical rat model of SUI and found that SKM did not restore urethral function or impact EUS morphology.

3.5 Materials and Methods

3.5.1 Animal Use Approval Statement

All procedures in this study were approved by the Institutional Animal Care and Use Committee at the University of California San Diego and performed according to guidelines from the Association for the Assessment and Accreditation of Laboratory Animal Care.

3.5.2 Leak Point Pressure Measurement

The LPP experimental setup, displayed in Figure 3.9, comprises a syringe pump (MANUFACTURER) that acts on a 15 mL syringe, which is connected to a system of stopcocks and diaphragms (ADInstruments). The central distensible diaphragm is secured to a pressure transducer (ADInstruments) such that any changes in pressure within the system cause distension of the diaphragm, which in turn is detected by the pressure transducer. The signal from the pressure transducer is first received and processed by a bridge amplifier (ADInstruments), after which the signal is received by

PowerLab (ADInstruments) and observed on a connected computer with LabChart (ADInstruments) software.

Before each LPP experiment, the system was calibrated. The diaphragm was filled with water, after which an air-filled syringe and pressure manometer (ADInstruments) were connected via stopcock. A two point calibration was set using the LabChart software, utilizing the known pressure of the system from the pressure manometer. After calibration was completed, the air-filled syringe and manometer were disconnected, and a water-filled syringe was connected instead. Additionally, approximately 8” length of PE-50 tubing (BD Intramedic) was inserted onto a 21G needle (BD Medical) to create a water-tight fit. This needle was then secured onto the stopcock on the other side of the diaphragm and pressure transducer as seen in Figure 3.9. The entire system was then filled with water and all bubbles were removed.

To undergo LPP measurement, animals were first anesthetized under 3% isoflurane. The urethra were then catheterized by approximately 17.5 mm of PE-50 tubing, such that the catheter passes the bladder neck but does not touch the bladder wall, as shown in Figure 3.9. After catheterization, data recording began using LabChart software to measure pressure within the bladder.

Before leak measurement, animal bladders were first acclimated with a 900 µL fill volume at a rate of 83 µL/min, previously established in the literature.[113] Once filling completed (approximately 11 minutes), the rats were left to acclimate for an additional 20 minutes, after which the bladder was completely emptied through a credé maneuver, or abdominal pressure applied above the bladder. The bladder was then filled to slightly less than half capacity – 400 µL – to prepare for LPP measurements. Once filling was

completed, a credé maneuver was applied slowly, with increasing pressure, until a leak was observed, after which pressure was immediately removed. An example pressure trace is shown in Figure 3.9; to compute leak point pressure, the baseline pressure before beginning the credé maneuver was subtracted from the peak pressure during the credé maneuver. This procedure was repeated 5-8 times to find an average LPP value for the animal at the given timepoint. Animals were then removed from anesthesia and observed until mobile.

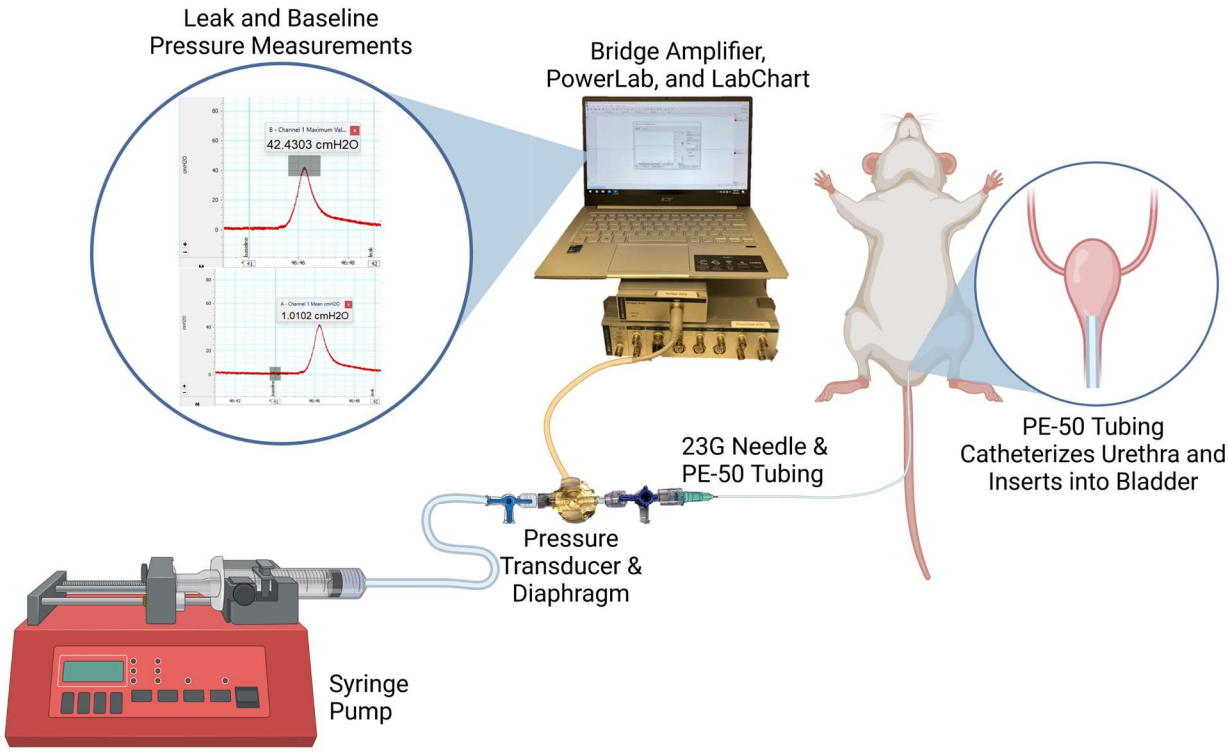


Figure 3.10 Diagram of leak point pressure experimental setup

3.5.3 Animal models of SUI

3.5.3.1 Single SBI Model

This model included 3 rounds of study with differing experimental timelines.

In the first two rounds, young (~3 month old) female Sprague Dawley rats underwent LPP measurements to first establish their healthy baseline values. Immediately following baseline LPP measurement, the rats underwent SBI procedure, in which a 12 French Foley catheter (Bard Medical) was inserted into the vagina, assisted by water-soluble lubricant. The catheter was secured in place with suture then filled with 5 mL water. The rats underwent SBI with a distension volume of 5 mL for 2 hours, after which the inflated catheter balloon was removed. The animals then immediately underwent an additional LPP measurement to determine urethral function acutely post-SBI. Animals were removed from anesthesia and observed until mobile. The sample size for these two rounds of study combined was n=7 (n=4 for round 1, n=3 for round 2), with each animal undergoing baseline LPP, SBI, and acute post-SBI LPP procedures done on the same day. Follow-up LPPs were performed at 4 weeks post-SBI for each animal (round 1) or at 2, 3, 4, and 5 weeks post-SBI for each animal (round 2).

In the third round, to expedite experimental progress, the baseline LPP, SBI, and acute post-SBI LPP procedures were separated into subsequent procedural days to enable higher throughput and larger sample size for future studies. Young (~3 month old) female Sprague Dawley rats underwent LPP measurements to establish their healthy baseline values (n=4). The next day, all 4 animals underwent SBI procedure as previously described, and on the day after SBI, all 4 animals underwent LPP testing. Additional LPP follow-up measurements were made weekly at 4, 6, and 8 weeks post-SBI.

3.5.3.2 Repeated SBI Model

Young (~3 month old) female Sprague Dawley rats underwent LPP measurements to establish their healthy baseline values (n=5 animals). The next day, all 5 animals underwent SBI procedure as previously described, and on the day after SBI, all 5 animals underwent LPP testing. Additional SBIs, including 1 day pre-SBI and 1 day post-SBI LPP measurements, were performed at 2 and 4 weeks after the first SBI. Follow-up LPP measurements were taken at 1, 3, 5, 6, 7, and 8 weeks after the first SBI.

3.5.3.3 Retired Breeder Model

Retired breeder Sprague Dawley female rats were ordered, which were approximately 7-8 months of age with a history of several pregnancies and litters. These rats underwent LPP measurements to establish their healthy baseline values (n=5 animals). The next day, all animals underwent SBI procedure as previously described, and on the day after SBI, animals underwent follow-up LPP testing. Additional follow-up LPP measurements were taken 1, 2, 3, and 4 weeks post-SBI.

3.5.3.4 Ovariectomy Model

Young (~3 month old) female Sprague Dawley rats underwent bilateral ovariectomy procedure and were delivered 2 weeks after ovariectomy. These rats underwent LPP measurements to establish their healthy baseline values (n=3 animals). The next day, all animals underwent SBI procedure as previously described, and on the day after SBI, animals underwent follow-up LPP testing. Additional follow-up LPP measurements were taken 1, 2, 3, and 4 weeks post-SBI. At the 4 weeks post-SBI timepoint, it was observed that LPP values had returned to baseline healthy value for these animals; thus, in efforts to establish a more severe SUI phenotype, a 2nd SBI was

performed. Follow-up LPP measurements were taken for these animals 1 day and 6 weeks after the 2nd SBI.

3.5.4 Histological assessment of EUS morphology in SUI models

For all animals from the SUI model groups (single SBI, repeated SBI, retired breeder, and ovariectomy), urethral tissues were harvested and fixed in 4% PFA for approximately 1 hour before being transferred to a 30% sucrose solution for 48 hours. Tissues were then submerged in OCT (Tissue-Tek) and frozen in liquid nitrogen chilled 2-methylbutane. Tissues were cryosectioned at a 10 μm thickness, with tissue sections taken at locations 500 μm apart spanning the entire length of the urethra. For evaluation of EUS morphology, tissue sections were stained against skeletal muscle myofibers (A41025, Abcam) with Alexa Fluor 647 goat anti mouse secondary antibody (Invitrogen) as well as DAPI to stain nuclei. The area of EUS, defined by the outer and innermost border of skeletal muscle, was traced, as was the interior lumen diameter. Additionally, the area of positively stained skeletal muscle myofibers within the EUS area was obtained through uniform thresholding of all samples. To assess EUS morphology, the area of EUS or the area of skeletal muscle myofibers were both normalized to the lumen area for that section, and five sections were analyzed per animal. Additionally, the density of skeletal muscle sphincter in the EUS was defined as the area of skeletal muscle myofibers divided by the area of the EUS.

3.5.5 SKM Hydrogel Fabrication

SKM material was fabricated as previously described.[91] Briefly, porcine skeletal muscle was chopped into small cubes before being spun in a 1% sodium dodecyl sulfate detergent solution for 5 days, with daily solution changes. Tissue was thoroughly rinsed

in water to remove residual detergent. Decellularized tissue was frozen at -80ºC and then lyophilized for 48 hours, after which the material was milled to a fine powder. This powder was partially enzymatically digested at 10 mg/ml in pepsin (1 mg/mL pepsin in 0.1 M HCl) pepsin for 48 hours, and then pH was neutralized, and ionic concentration balanced. SKM was brought to a concentration of 6 mg mL^{-1}, which was determined as the optimal concentration for skeletal muscle injection.[72]

3.5.6 Optimization of SKM injection volume

As urethra injection volumes within the literature vary wildly, we first conducted a series of experiments to optimize the injection volume and delivery of SKM to the EUS. For all injection optimization experiments, SKM was fluorescently prelabeled with a NHS Succinimidyl Ester tag, with either a 568 or 647 fluorophore tag (Invitrogen).

To prepare for injection, animals were first anesthetized under 3% isoflurane. Urethral EUS injections were performed first by exposing the bladder and proximal urethral via laparotomy. The bladder was sutured with 4-0 suture (Ethicon) to enable articulation of the bladder. The suture was utilized to pull the bladder and reveal the mid urethra. SKM was loaded into a 100 µL Hamilton syringe with a 30G needle, and the needle was inserted into the most superficial portion of the mid urethra with the needle bore oriented towards the urethral wall. The needle was then pushed further down the length of the urethra, approximately 5 mm, while maintaining a parallel orientation of the needle. The syringe plunger was slowly and steadily depressed while retracting the needle to the insertion point, evenly dispersing the injection volume (either 10, 15, or 20

μL) over the length of the mid urethra. A total of two such injections were performed, on the left and right sides of the urethra.

For optimization of the injection procedure, urethral tissues were harvested, fixed, and frozen as previously described immediately after the injection procedure. Additional studies were conducted in which animals were survived for 1 week post-injection to assess material retention in the EUS.

3.5.7 Assessing effect of SKM injection on urethral function

As both 10 and 15 μL were determined to be suitable and nondestructive injection volumes for delivery of materials to the EUS, the 15 μL injection volume was chosen for an initial pilot study assessing the therapeutic potential of SKM for restoring urethral function. Animals underwent LPP testing to establish a healthy baseline value, and on the following day, animals underwent SBI procedure. Two weeks after SBI, LPP measurements were taken for each animal to test for recovery to the healthy baseline; if the two week post-SBI LPP measurement was not significantly different from the healthy baseline, the animals were excluded from study. The following day, a total of 13 animals underwent EUS injection procedure and were randomly assigned to receive 15 μL of either SKM (n=7) or saline (n=6) injection. Additional follow-up LPP measurements were taken 2, 4, and 6 weeks post-injection (4, 6, and 8 weeks post-SBI). At the final timepoint, urethral tissues were fixed and frozen as previously described.

3.5.8 Histological assessment of the effect of SKM injection on EUS morphology

Urethral tissues were sectioned at 10 μm thickness and stained against skeletal muscle and nuclei as previously described (Section 3.5.4). Similarly, 5 sections per animal were assessed for EUS area and lumen perimeter for normalization.

3.5.9 Statistical analysis

All statistical analysis was completed utilizing GraphPad Prism version 10.2. For LPP comparisons to healthy baseline for each animal, a one-way ANOVA with multiple comparisons to the healthy baseline was used, with Dunnett's post-hoc correction. For comparison of EUS area between SUI model groups, a one-way ANOVA with multiple comparisons to healthy/unperturbed controls was used, with Dunnett's post-hoc correction. For comparison of EUS area between SKM and saline injection groups, an unpaired t-test was used.

3.6 Acknowledgements

This research was funded in part by the NIH. The author would like to thank Danna Du for her work on optimizing EUS injection methodology and volume, conducting histomorphological analysis of EUS in various models of SUI, and general assistance and support for the work presented in this chapter.

Chapter 3, in part, is currently being prepared for submission for publication of the material. Emma I. Zelus, Danna Du, Marianna Alperin, Karen L. Christman. The dissertation author was the primary researcher and author of this material.

Chapter 4: Development of a Novel Vaginal Extracellular Matrix Hydrogel for Combating Genitourinary Syndrome of Menopause

4.1 Introduction

Genitourinary syndrome of menopause (GSM) refers to the pathological changes in the vulvovaginal and lower urinary tract tissues as a result of the hypoestrogenemia in perimenopausal and menopausal women.[114] Up to 85% of women over 40 years of age are affected by some form of GSM, with 30-60% of women with GSM suffering from vaginal pruritis and irritation.[114] Not surprisingly, women with GSM report that this condition negatively affects their sexual activities and ability to be intimate, interferes with their enjoyment of life and sleep, and hinders traveling, work, and athletic and social activities.[115] Given that over 1.3 million women become menopausal every year and that the expected lifespan is continuously increasing, this population is rapidly expanding.[116] As such, GSM represents a major public health issue, making it imperative to design affordable, accessible, and effective treatments for this morbid condition.

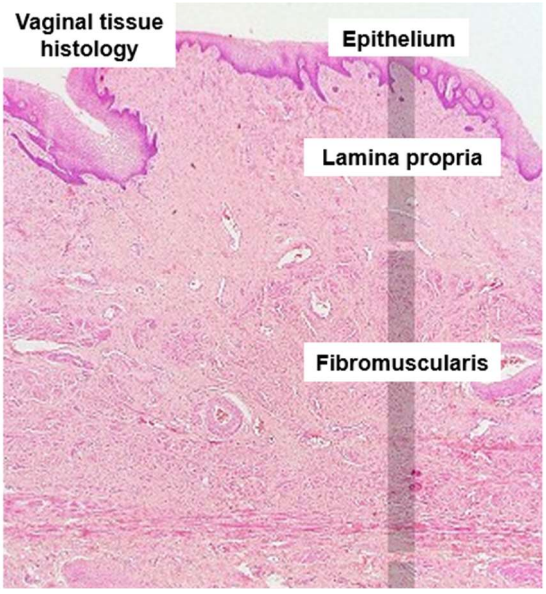


Figure 4.1 Histology of vaginal tissue layers.

GSM is initiated by the hypoestrogenic state consequent to the cessation of ovarian function, defined as menopause.[114] Estrogen deprivation results in decreased proliferation and differentiation of vaginal epithelial cells.[117] Normally, vaginal epithelium (Figure 4.1) undergoes terminal differentiation to cornified cells filled with glycogen that support lactobacilli and associated low vaginal pH.[118] Following estrogen deprivation, the epithelium atrophies and the vaginal rugae (or invaginations) begin to disappear, leaving a thin and vulnerable layer of basal epithelium.[117,119] This results in a cascade of events which increases the overall vaginal pH, allowing bacterial dysbiosis and inflammation. Further pathological changes include diminished vascularization and smooth muscle content and contractility within the fibromuscularis, with consequent impairment of vaginal elasticity.[120,121] Additionally, ECM within the lamina propria and fibromuscular layer (Figure 4.1) undergoes pathological changes, including a decrease in ECM content, higher collagen I:III ratio, and increased stiffness. Lastly, it is known that immune cells of the female reproductive tract are responsive to estrogen; in the hypoestrogenic state, increased expression of pro-inflammatory cytokines and a reduction in important immune populations, including T-regulatory cells, are hallmarks of the GSM phenotype.[122] The immune system is intricately involved with ECM remodeling,[123] and both immune

activation and ECM remodeling within vaginal tissues are impacted by estrogen deprivation in menopause.[124]

Considering the complex cascade of events consequent to the hypoestrogenic state, it is very difficult for GSM treatments to initiate comprehensive regeneration. In fact, such treatments as lubricants provide no therapeutic benefit to the atrophied vaginal tissue; they solely serve to temporarily relieve the pain and discomfort related to vaginal dryness.[125] Moisturizers are another self-applied treatment; they are bioadhesives that modulate vaginal pH and benefit the epithelium, but their efficacy is mild and not suitable for more severe cases of GSM.[125,126] Low-dose vaginal estrogen therapy is the gold-standard GSM treatment, as it addresses the root cause of vulvovaginal atrophy and is highly effective at restoring epithelium and lamina through estrogen-sensitive immunomodulation pathways.[125] Despite these benefits, women and clinicians often reject this treatment because it can be prohibitively expensive and can increase the risk of hormone-sensitive cancers, when administered systemically.[115] Furthermore,

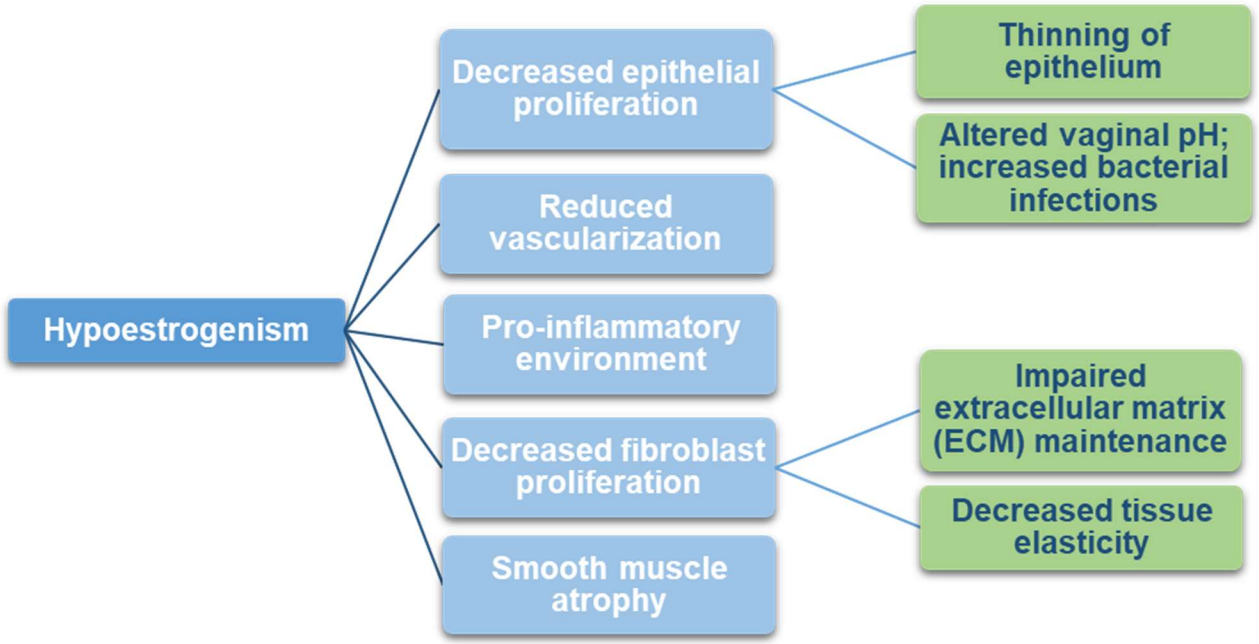


Figure 4.2 Downstream effects of hypoestrogenism in vaginal tissues

therapeutic benefit of locally delivered estrogen is limited to the epithelium and lamina propria and fails to improve the fibromuscular phenotype.[127] Selective estrogen receptor modulators are targeted agonists or antagonists for estrogen receptors and can be used as non-hormonal alternative to estrogen; however, there is considerable potential for off-target effects, and efficacy is inconsistent.[126,128] Lastly, laser therapy has shown some efficacy for repairing the fibromuscularis, but side effects of epithelial burns, scarring, and chronic pain incited a recent FDA warning against this treatment.[126–128] Importantly, only 35% of women suffering from GSM are satisfied with their treatment, whether prescribed or over-the-counter.[115] Overall, it is evident that there is a paucity of GSM treatments that address the underlying pathophysiology while remaining affordable and safe.

In response to the above clinical need, a recent preclinical study explored intravaginal administration of an acellular therapeutic, specifically a recombinant collagen-derived adhesion protein delivered within a vehicle substrate, to improve the atrophic vaginal phenotype observed in a ovariectomy rat model of GSM.[129] This recombinant protein-based vaginal wash promoted proliferation and differentiation of vaginal epithelial cells, improving epithelial thickness and restoration of ECM in the lamina propria.[129] This study demonstrated the potential of an acellular biomaterial as a nonhormonal and effective alternative to current treatments for GSM. Our lab previously demonstrated that collagen-based biomaterials are inferior in inducing regeneration compared to a tissue-specific ECM biomaterial.[35] Furthermore, unpublished preliminary data suggest that collagen alone has an inhibitory effect on proliferation of smooth muscle

cells (Figure 4.2), an integral component of the vaginal fibromuscular layer.

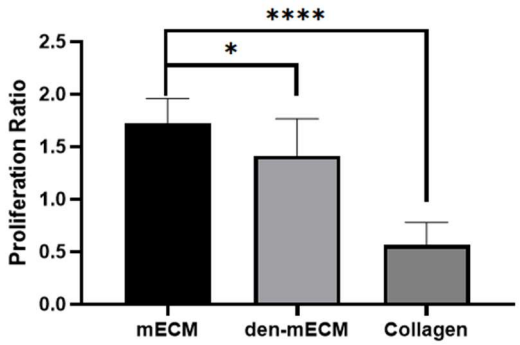


Figure 4.3 Cellular proliferation assay performed with mouse vascular smooth muscle cells.

Mouse vascular smooth muscle cells were cultured with mECM (a skeletal muscle derived ECM), denatured mECM, collagen, or PBS control doped into the media. Proliferation was assessed via PicoGreen assay and normalized to the PBS control, and mECM demonstrated improvement of cell proliferation compared to denatured mECM and collagen.

Here, we propose the use of a decellularized tissue-specific ECM hydrogel for the treatment of GSM. ECM hydrogels have been extensively investigated in various tissue engineering applications. The ECM is a complex network of proteins vital for structural support and cell signaling; when a whole tissue is decellularized, the ECM remains as an acellular and highly biocompatible material with tissue regenerative properties.[25] Previous studies showed that the decellularized porcine skeletal muscle ECM harnesses the regenerative potential of the host tissue by increasing vascularization, enhancing the recruitment and differentiation of muscle progenitors, and reducing cell death.[42] ECM biomaterials have tissue-specific therapeutic benefits due to the diverse biochemical nature of different tissues.[25] For example, our lab has previously shown that in a rat hindlimb ischemia model, the tissue-specific skeletal muscle ECM hydrogel (mECM) significantly enhances myoblast proliferation and differentiation, vascularization, and cellular metabolism as compared to collagen.[35,68] Additionally, across several different

animal models using tissue-specific ECM hydrogels, we have observed modulation of the immune response via macrophage polarization from pro-inflammatory to pro-regenerative phenotype. These tissue-specific biomaterials have demonstrated constructive ECM remodeling in a variety of disease models.

Our lab has extensively studied the fabrication, characterization, and application of tissue specific ECM hydrogels. The fabrication of our ECM hydrogel consists of mincing porcine tissue and spinning the tissue in a detergent to remove cellular content. After several days, the tissue is lyophilized, milled into a uniform powder, and digested with pepsin to obtain a solubilized material. The digested ECM ionic concentration is adjusted to correlate with physiological conditions. At last, the soluble ECM is re-lyophilized and stored at -80C for long-term use. The ECM is a thermo-responsive material; after being reconstituted in sterile water, it will form a hydrogel at physiologic temperature. Porcine tissue is the most translationally relevant source for our hydrogels given the large quantities, the potential for prion disease with bovine tissue, and the high variability and age related changes of human ECM.[130,131] Importantly, porcine-derived materials do not induce an aberrant immune response as long as they are appropriately decellularized.[130] ECM hydrogels are highly biocompatible with a great potential for clinical translation; in fact, a fabricated porcine derived myocardial ECM hydrogel finished a Phase I Clinical trial (clinicaltrial.gov NCT02305602) for the treatment of myocardial infarction.[26] Taken together, the above led to our overall theoretical framework for a high impact, minimally invasive, and accessible intervention for GSM that capitalizes on the pro-regenerative

impact of the ECM hydrogels on the host tissues.

4.2 Results

4.2.1 Fabrication and characterization of vaginal ECM (vECM) hydrogel

As no group has published on a decellularized vaginal tissue derived ECM hydrogel, we first underwent extensive optimization of a new decellularization protocol, informed by the successful decellularization framework that has produced decellularized skeletal muscle and cardiac ECM hydrogels within the lab. Table 4.1 provides a breakdown of the decellularization conditions tested. In summary, the first conditions tested were based on the decellularization protocols for skeletal and cardiac muscle ECM hydrogel production: 1% SDS rinse for 5 days, and 1 day water rinse. These decellularization conditions did not result in successful gelation of the material; rather, it was necessary to utilize a much lower concentration of SDS for a shorter duration – 0.1% for 3 days – with a longer water rinsing period of 3 days to remove residual SDS. This is likely due to the considerable differences in tissue structure between vaginal and skeletal or cardiac muscle tissues. While skeletal and cardiac muscle are largely composed of tightly packed muscle fibers – large amounts of cellular material with thin layers of ECM interspersed – the vaginal tissue has much less cellular content and is largely composed of ECM with relatively little composition of epithelial and smooth muscle cells. Thus, vaginal tissue required a gentler decellularization and more through water rinse to preserve ECM structure and sufficiently remove residual detergent.

Table 4.1 vECM batches and processing variables

Batch	Tissue Processing	Decellularization	Water rinse	Gelation?
vECM-A	Hand-chopped	1% SDS 5 days	1 day	No
vECM-B	Hand-chopped	1%, 0.5%, or 0.1% SDS 3 days	3 days	Yes at 0.1% SDS only
vECM-C	Meat grinder	0.1% SDS 3, 4, or 5 days	3 days	Yes at 3 days only
vECM-D	Meat grinder	0.1% SDS 3 days	3 days	Yes

The final decellularization protocol is depicted in Figure 4.3. In brief, porcine vaginal tissue is isolated and frozen before being processed (Figure 4.3A). The tissue is minced using a commercial meat grinder (Figure 4.3B) and then spun in 0.1% SDS for 3 days and water for an additional 3 days, with daily solution changes (Figure 4.3C). The decellularized tissue is then lyophilized (Figure 4.3D) and milled to a fine powder that is passed through a #60 filter (Figure 4.3E). The milled vaginal ECM (vECM) is partially enzymatically digested for 48 hours in pepsin suspended in HCl (Figure 4.3F). The suspension is then pH and salt balanced, needle sheared through a 27G needle, and incubated at 37°C to form a hydrogel at 4, 6, or 8 mg/mL (Figure 4.3G).

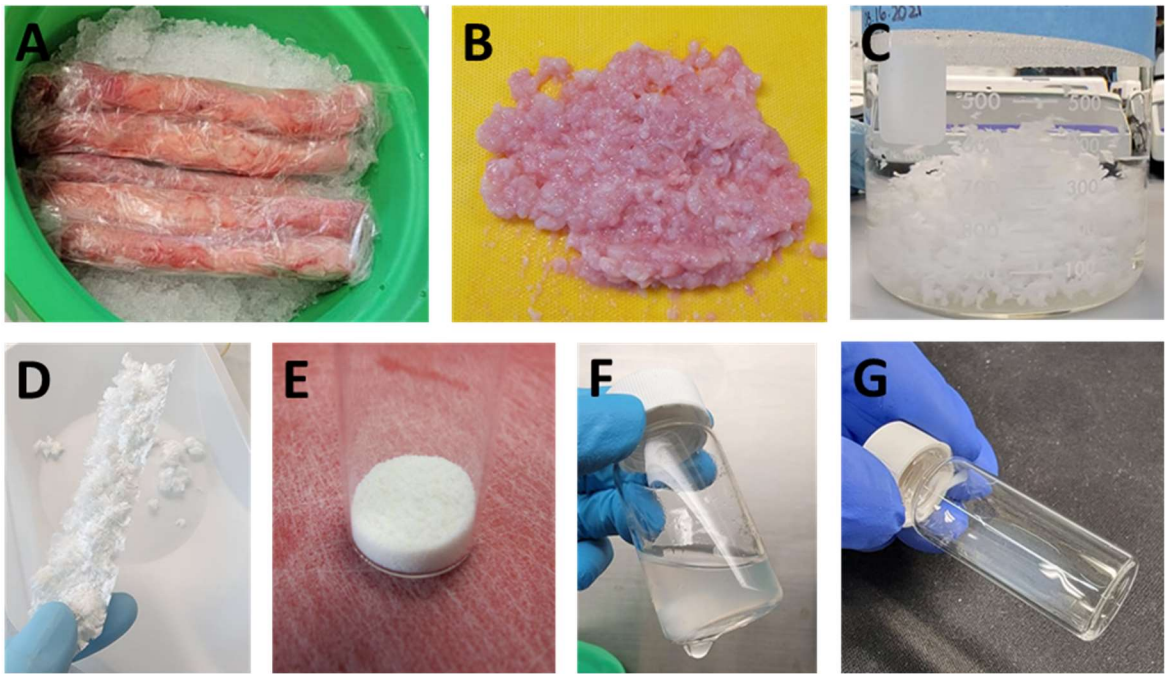


Figure 4.4 Production of a porcine vaginal tissue derived ECM hydrogel

Porcine vaginal tissues were cleaned and frozen (A) before being minced with a commercial meat grinder (B) then spun in SDS to decellularize the tissue (C). Decellularized tissue was lyophilized (D) and milled to a fine and unform powder which was passed through a #60 filter (E). Decellularized vECM powder was partially enzymatically digested with pepsin (F) then pH and salt balanced before incubating at 37°C to form a stable hydrogel (G).

Upon creating a decellularized vaginal ECM hydrogel that successfully formed a hydrogel, we proceeded to characterize the material for ECM structure, residual nuclear material, sulfated glycosaminoglycan content, endotoxin content, and cytocompatibility. During processing, samples were taken from fresh vaginal tissue or vaginal tissue after 1, 2, or 3 days of decellularization. Samples were frozen, cryosectioned, and stained with H&E to visualize tissue structure and nuclear material, as shown in Figure 4.4. Throughout the decellularization process, the stripping of nuclear material is evident first through the smearing of purple stain (hematoxylin, which stains cell nuclei) and then

complete removal of purple staining. Despite the thorough decellularization, it is further evident that the structure and integrity of the tissue is maintained.

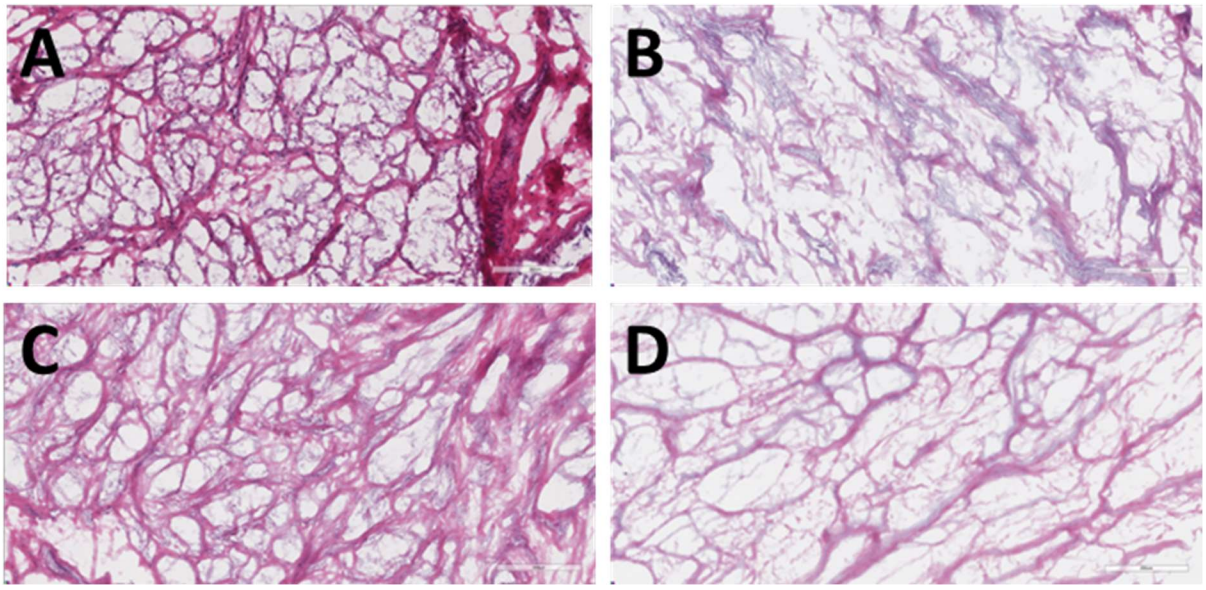


Figure 4.5 H&E staining of porcine vaginal tissue throughout the decellularization process Samples of vaginal tissue were taken from fresh tissue (A) or tissue after either 1 (B), 2 (C), or 3 (D) days of decellularization. Tissue samples were cryosectioned and stained with hematoxylin and eosin to demonstrate removal of nuclear material (purple) and retention of tissue structure (pink).

vECM material was then characterized for residual double stranded DNA, endotoxin content, sulfated glycosaminoglycan content, and cytocompatibility. Residual double stranded DNA, measured through a PicoGreen assay, was used to assess residual nuclear content as a metric for complete decellularization and removal of antigenic components. Endotoxin was assessed through a limulus amebocyte lysate assay as the vaginal tissue may be exposed to bacteria, and retention of endotoxin could be harmful in application of vECM as a therapeutic. Sulfated glycosaminoglycans were quantified with a 1,9-dimethylmethylene blue assay to ensure the tissue was not over-decellularized, resulting in removal of ECM components that are vital for therapeutic

function, such as sulfated glycosaminoglycans. For all three of these assays, vECM was within expected specifications, as listed in Table 4.2.

Table 4.2 Material characterization assays performed on vECM

Characterization	Average Amount	SD	Standard Range
Residual Double Stranded DNA	0.4 ng dsDNA/mg ECM	0.5	<50 µg dsDNA/mg ECM
Endotoxin	0.18 EU/mL	0.01	<0.25 EU/mL
Sulfated Glycosaminoglycans	10.6 µg sulfated glycosaminoglycan/mg ECM	0.2	5-15

Lastly, vECM was tested for cytocompatibility through coculture encapsulation assays with L929s (mouse fibroblasts) and HUVECs (human umbilical vein endothelial cells) to represent two abundant cell populations within the vaginal tissue. Both cell types were mixed with vECM suspension at an 8 mg/mL concentration then pipetted onto tissue culture plates and incubated to form 3D hydrogel-cell structures. Cells were monitored over a period of 48 hours, and robust cell expansion and motility were observed (Figure 4.5). Cells were observed to actively digest the ECM scaffold, indicating that cells were actively interacting with the vECM, as expected from prior studies with ECM hydrogels. Thus, in addition to the material characterization assays performed, the vECM hydrogel was deemed to be cytocompatible.

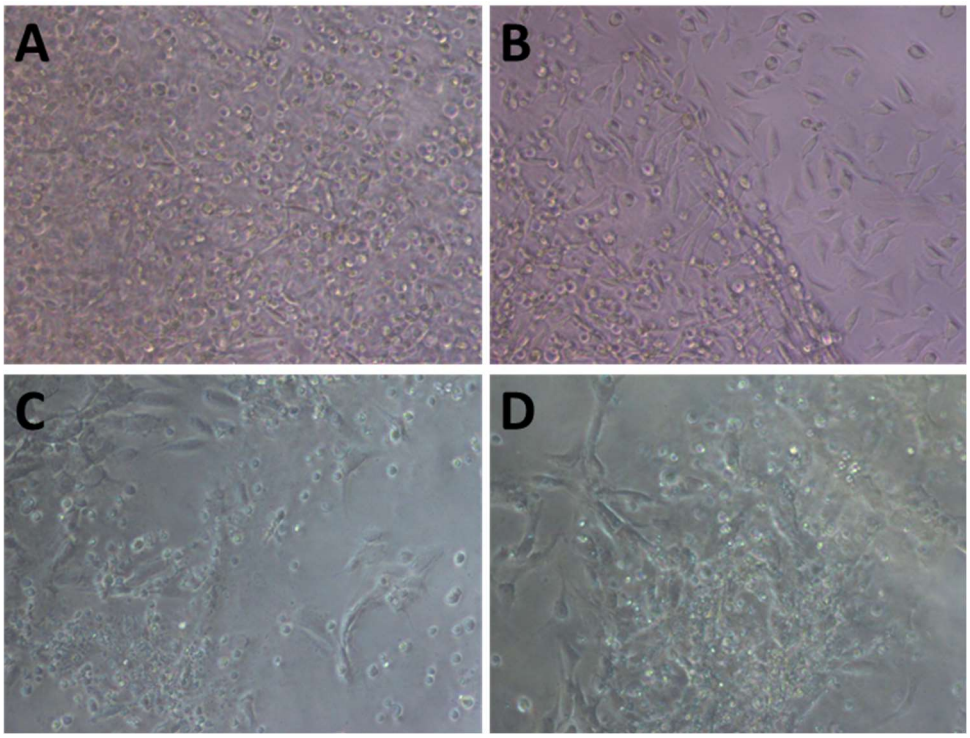


Figure 4.6 Encapsulation of L929 and HUVEC cells in vECM to assess cytocompatibility

Rat fibroblast (L929) or human umbilical vein endothelial (HUVEC) cells were encapsulated in vECM. The vECM-cell suspensions were then pipetted in the middle of a tissue culture well. vECM-cell suspensions were incubated at 37°C for 1 hour to form stable hydrogels, after which the hydrogel was submerged in cell growth media. Cells were imaged under a microscope 48 hours later to assess cell viability, migration, and interaction with the vECM. Both L929 (A-B) and HUVEC (C-D) cells displayed robust cell morphology within the gel, migration within and out of the hydrogel, and digestion of the surrounding ECM.

4.2.2 vECM improves epithelial thickness and morphology in ovariectomized rats

For a first assessment of the therapeutic potential of vECM, we utilized a well-established model of menopause in the rat involving bilateral ovariectomy. In this model, vaginal tissue phenotype models the GSM condition by two weeks post-ovariectomy. Therefore, as shown in the timeline in Figure 4.6A, our treatment began two weeks post-ovariectomy with daily intravaginal administration for a period of two weeks of saline, vECM at two concentrations (6 mg/mL and 8 mg/mL), and a non-tissue specific ECM

control, collagen. Following the two weeks of treatment, animals were euthanized on the following day, and vaginal tissues were frozen for histological assessment. Additional age-matched healthy (non-ovariectomized) controls were used for comparison.

The primary treatment outcome of interest was epithelial thickness, as epithelial atrophy is a main symptom of GSM that contributes to vaginal pain and discomfort. Tissue sections were stained with hematoxylin and eosin (H&E) to assess epithelial thickness. Representative tissue sections for healthy, saline, collagen, vECM 6 mg/mL, and vECM 8 mg/mL groups are shown in Figure 4.6B-F. As shown in the summary of data in Figure 4.6G, the vECM 8 mg/mL group demonstrated significantly greater epithelial thickness compared to saline, collagen, and vECM 6 mg/mL groups; however, vECM 8 mg/mL did not fully return the epithelial thickness to healthy values. These results indicate that vECM has a dose dependent and significant effect on restoration of epithelium in menopausal rats.

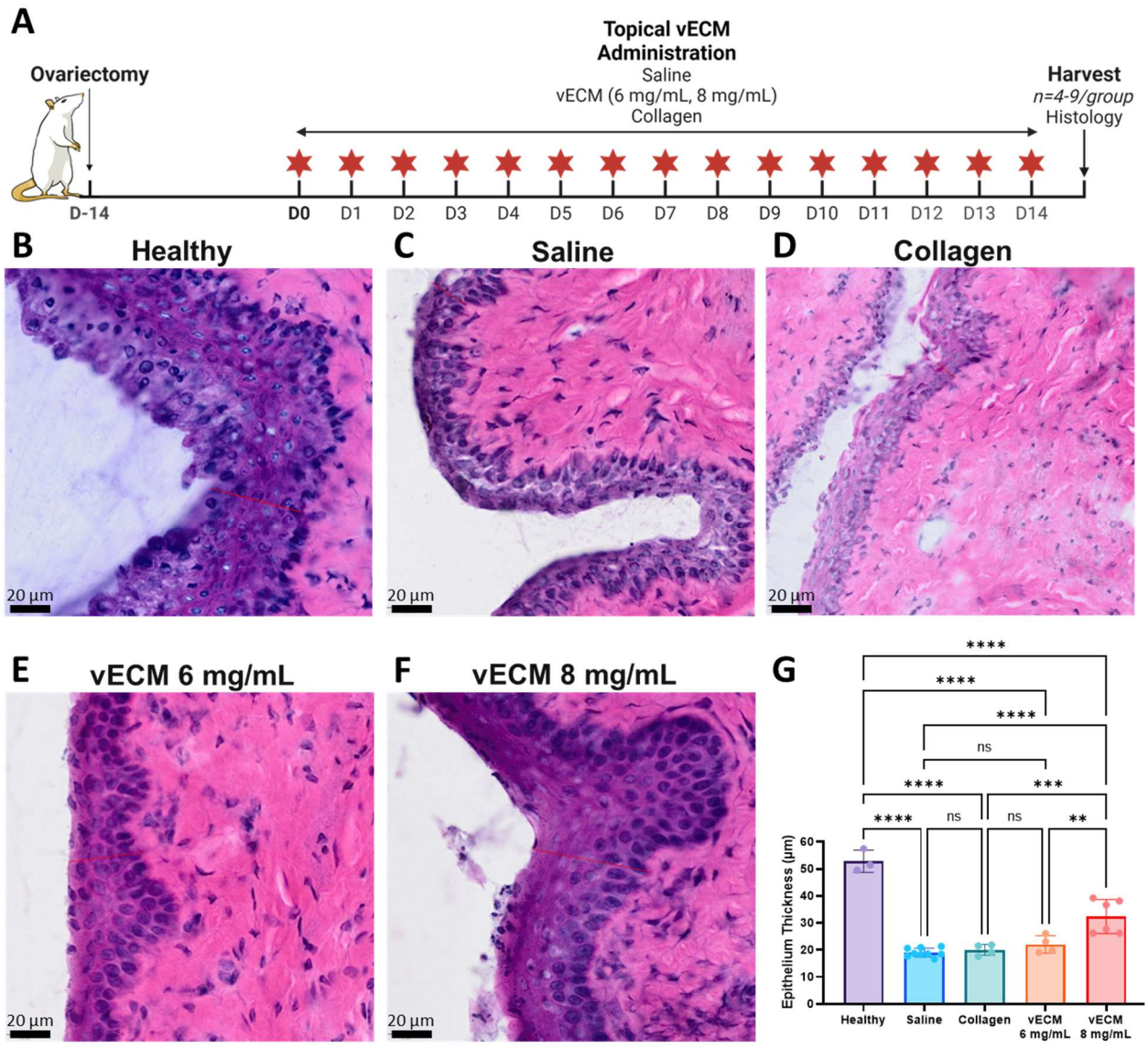


Figure 4.7 Evaluation of vECM efficacy in restoring vaginal epithelium in menopausal rats

(A) Experimental timeline to assess therapeutic efficacy of intravaginal administration of vECM, alongside saline and collagen, in a rat model of surgical menopause via ovariectomy. After treatment, vaginal tissues were isolated, sectioned, and stained with hematoxylin and eosin to assess vaginal epithelial thickness. Representative images are shown for healthy (unperturbed) controls (B) and ovariectomized rats treated with saline (C), collagen (D), vECM 6 mg/mL (E), or vECM 8 mg/mL (F). Data for epithelial thickness were averaged per animal and compared among groups with a one-way ANOVA (G).

We next conducted immunohistochemical staining to assess the epithelial phenotype and particularly the behavior of epithelial stem cells. Tissue sections from

healthy animals as well as ovariectomized animals that received saline or vECM 8 mg/mL treatment were stained against p63, a marker for epithelial stem cells, as well as filaggrin, a vaginal epithelial marker. The epithelial atrophy associated with menopause is due to a decrease in vaginal epithelial stem cell proliferation and differentiation;[119] while these stem cells persist throughout the menopausal condition, their proliferation and differentiation is slowed so much that they are only able to replenish their population but not maintain several layers of stratified differentiated epithelium.

This can be seen in the differences between healthy (Figure 4.7A) and saline (Figure 4.7B) representative images. In healthy animals, the $p63^+$ stem cells reside in the basal epithelium but constitute a relatively small portion of the total epithelium, indicated in green. Conversely, in ovariectomized and saline treated animals, the $p63^+$ stem cells occupy almost the entirety of the vaginal epithelium, with very little differentiated epithelium present. Ovariectomized animals treated with vECM at 8 mg/mL conversation do, however, present an overwhelmingly healthy-appearing vaginal epithelium phenotype. vECM and healthy groups are similar and significantly different than saline group in metrics of nuclei density (number of nuclei normalized by epithelial area, Figure 4.7D), $p63^+$ nuclei density (number of epithelial stem cell nuclei normalized by epithelial area, Figure 4.7E), and proportion of $p63^+$ nuclei (number of epithelial stem cell nuclei normalized by total number of nuclei, Figure 4.7F). These analyses characterize the epithelial morphology and phenotype, demonstrating that vECM treated animals display similar vaginal epithelial activity to healthy animals and suggesting that vECM enables epithelial stem cells to proliferate and differentiate as they would in healthy animals.

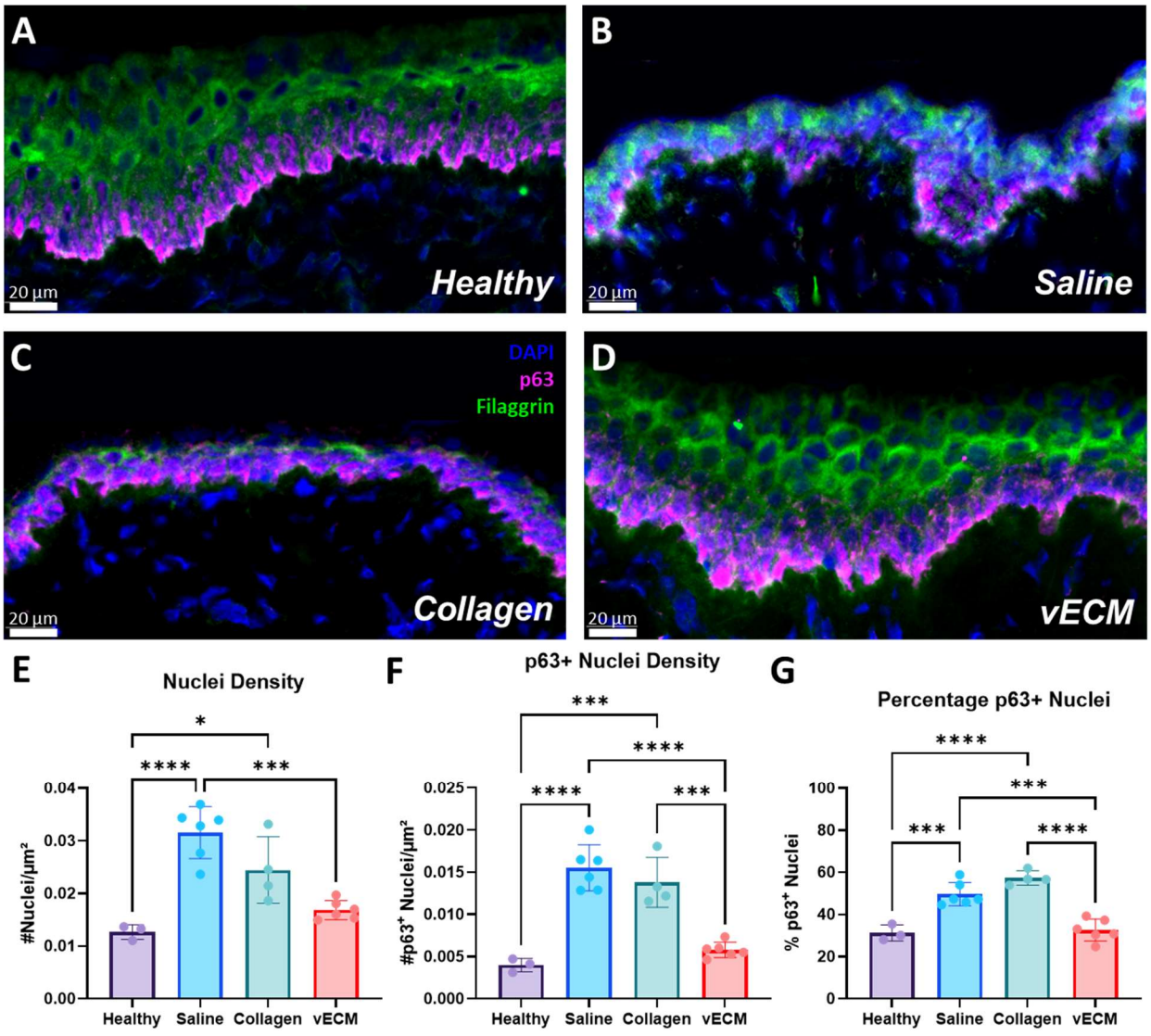


Figure 4.8 Characterization of vaginal epithelial phenotype in vECM treated animals

Vaginal tissue sections were stained against nuclei (DAPI, blue), an epithelial stem cell transcription factor (p63, magenta), and an epithelial membrane marker (filaggrin, green) to assess epithelial stem cell activity and phenotype. Representative immunofluorescent images are shown for healthy (unperturbed) controls (A) and ovariectomized rats treated with saline (B) or vECM 8 mg/mL (C). Vaginal epithelium was assessed for nuclei density (D), $p63^+$ vaginal epithelial stem cell nuclei density (E), and percentage of nuclei within the epithelium which were $p63^+$ vaginal epithelial stem cells (F).

4.2.3 vECM improves smooth muscle thickness and modulates smooth muscle proliferation

In addition to epithelial atrophy, smooth muscle atrophy is a notable consequence of the hypoestrogenic state; this can negatively impact the biomechanics of the vaginal tissue, leading to reduced contractility. Thus, we conducted immunohistochemical staining against alpha smooth muscle actin (αSMA) to assess the smooth muscle layer thickness in all treatment groups. Representative immunohistochemical staining for healthy, saline, collagen, vECM 6 mg/mL, and vECM 8 mg/mL groups are shown in Figure 4.9A-E, and quantitative comparison of these groups is shown in Figure 4.9F. vECM at the 8 mg/mL concentration demonstrated significantly greater smooth muscle thickness as compared to saline, collagen, and vECM 6 mg/mL groups, with no significant differences as compared to the healthy controls.

Tissue sections were additionally stained against the nuclear proliferation marker Ki67 alongside αSMA in order to assess the amount of proliferating smooth muscle cells. Representative immunohistochemical staining for healthy, saline, collagen, and 8 mg/mL vECM groups are shown in Figure 4.10A-D, and quantitative comparison of these groups is shown in Figure 4.10E-F. vECM treatment significantly improved both the density of nuclei within the smooth muscle layer (Figure 4.10E) and the percentage of proliferating nuclei within the smooth muscle (Figure 4.10F) compared to saline and collagen treatment, and vECM was not significantly different from healthy controls in either measurement. These data suggest that vECM treatment improves smooth muscle regeneration and induces a healthy smooth muscle phenotype.

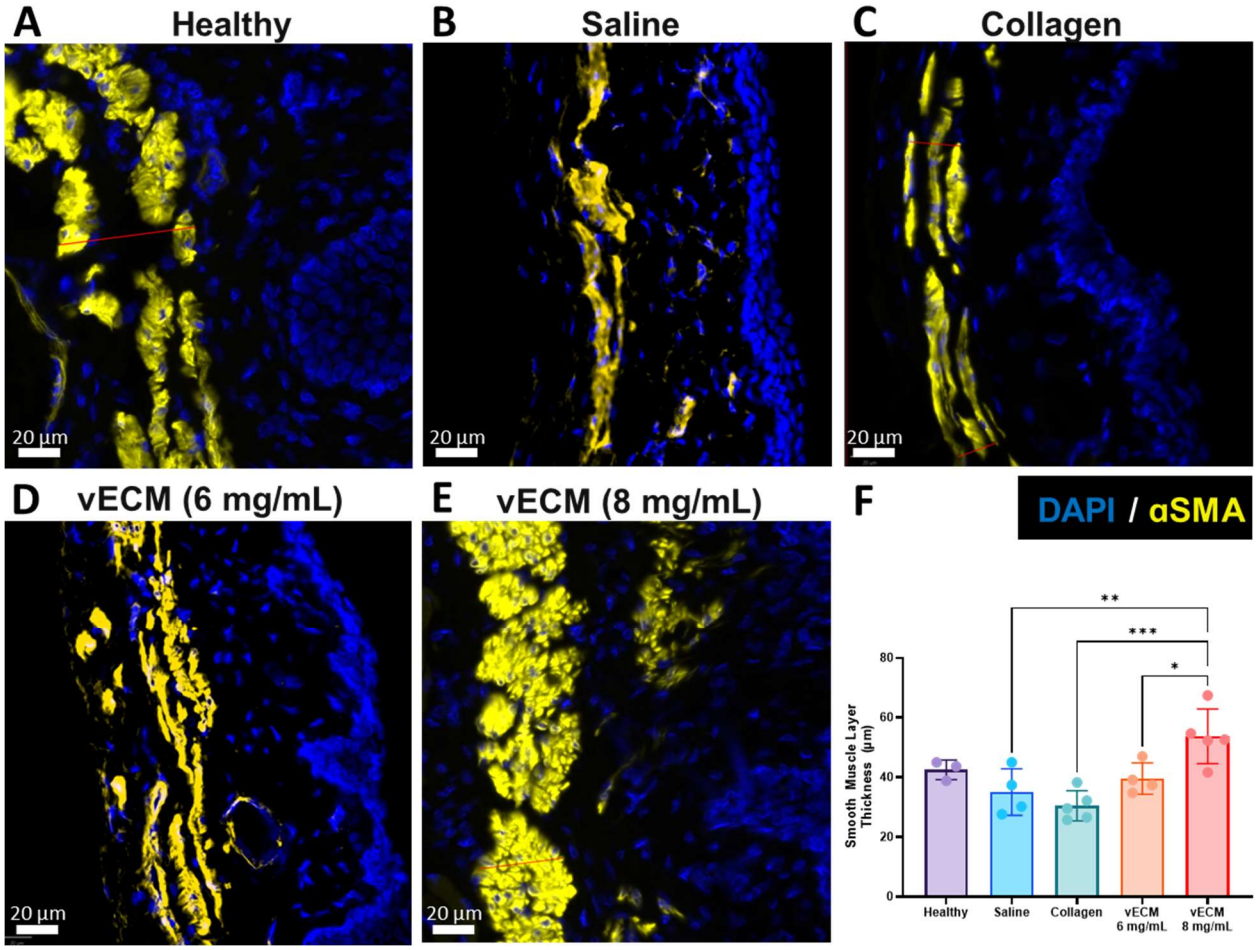


Figure 4.9 Evaluation of vECM efficacy in restoring vaginal smooth muscle in menopausal rats

Vaginal tissue sections were stained against nuclei (DAPI, blue) and smooth muscle (αSMA, yellow). Representative immunofluorescent images are shown for healthy (unperturbed) controls (A) and ovariectomized rats treated with saline (B), collagen (C), vECM 6 mg/mL (D), or vECM 8 mg/mL (E). Data for smooth muscle thickness were averaged per animal and compared among groups with a one-way ANOVA (F).

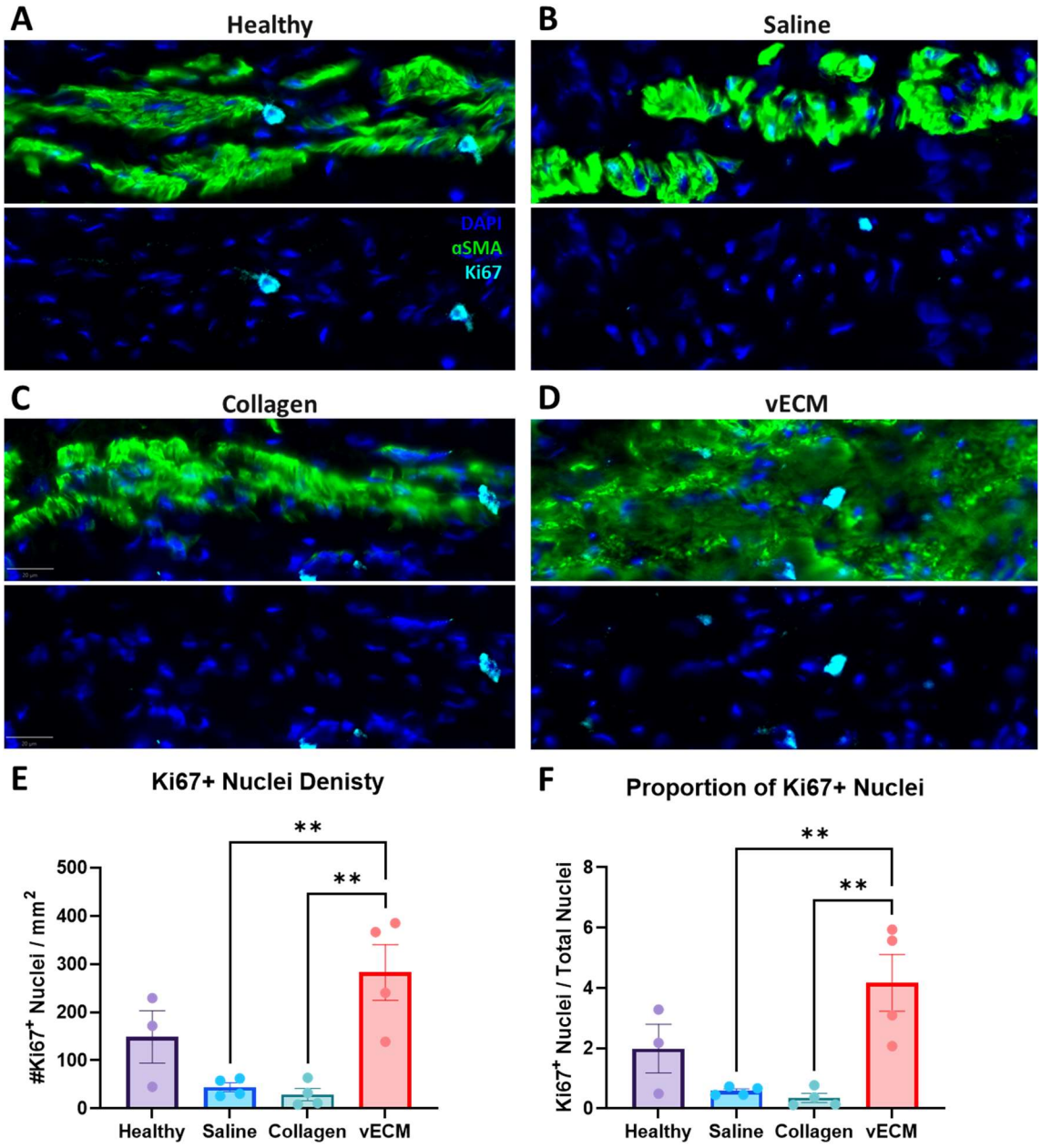


Figure 4.10 Assessment of vaginal smooth muscle cell proliferation following treatment

Vaginal tissue sections were stained against nuclei (DAPI, blue), smooth muscle actin (αSMA, green), and a nuclear marker of proliferating cells (Ki67, cyan). Representative immunofluorescent images are shown for healthy (unperturbed) controls (A) and ovariectomized rats treated with saline (B), collagen (C), or 8 mg/mL vECM (D). Groups were assessed for $Ki67^+$ nuclei density within the smooth muscle layer (E), and proportion of $Ki67^+$ nuclei over total nuclei within the smooth muscle layer (F).

4.2.4 Cells, particularly macrophages, are observed localizing to vECM in the vaginal lumen and fibromuscularis

Surprisingly, we observed that vECM at the higher concentration improved smooth muscle regeneration despite being administered intravaginally. To further investigate this outcome, ovariectomized rats underwent intravaginal administration of fluorescently prelabeled vECM at 8 mg/mL concentration and were euthanized for tissue harvest either 1, 2, or 3 days after injection (n=3/timepoint).

First, retention of vECM within the vaginal lumen was first assessed. Representative images from vaginal tissues 1, 2, or 3 days after intravaginal administration of vECM are shown in Figure 4.11A-C. At all timepoints, vECM is well spread throughout the vaginal lumen, but retention of the material does decrease each day. Higher magnification images, in Figure 4.11 D-F, show cellular localization to vECM within the lumen; this is particularly striking given that there we have not observed cellularity in the vaginal lumen in ovariectomized rats. At days 2 and 3 post-administration, some vECM is observed spanning the epithelial border, and some of the cells localizing to vECM display costaining of CD68 and CD163, which are membrane markers that, in combination, are characteristic of M2 (pro-regenerative/anti-inflammatory) macrophages.

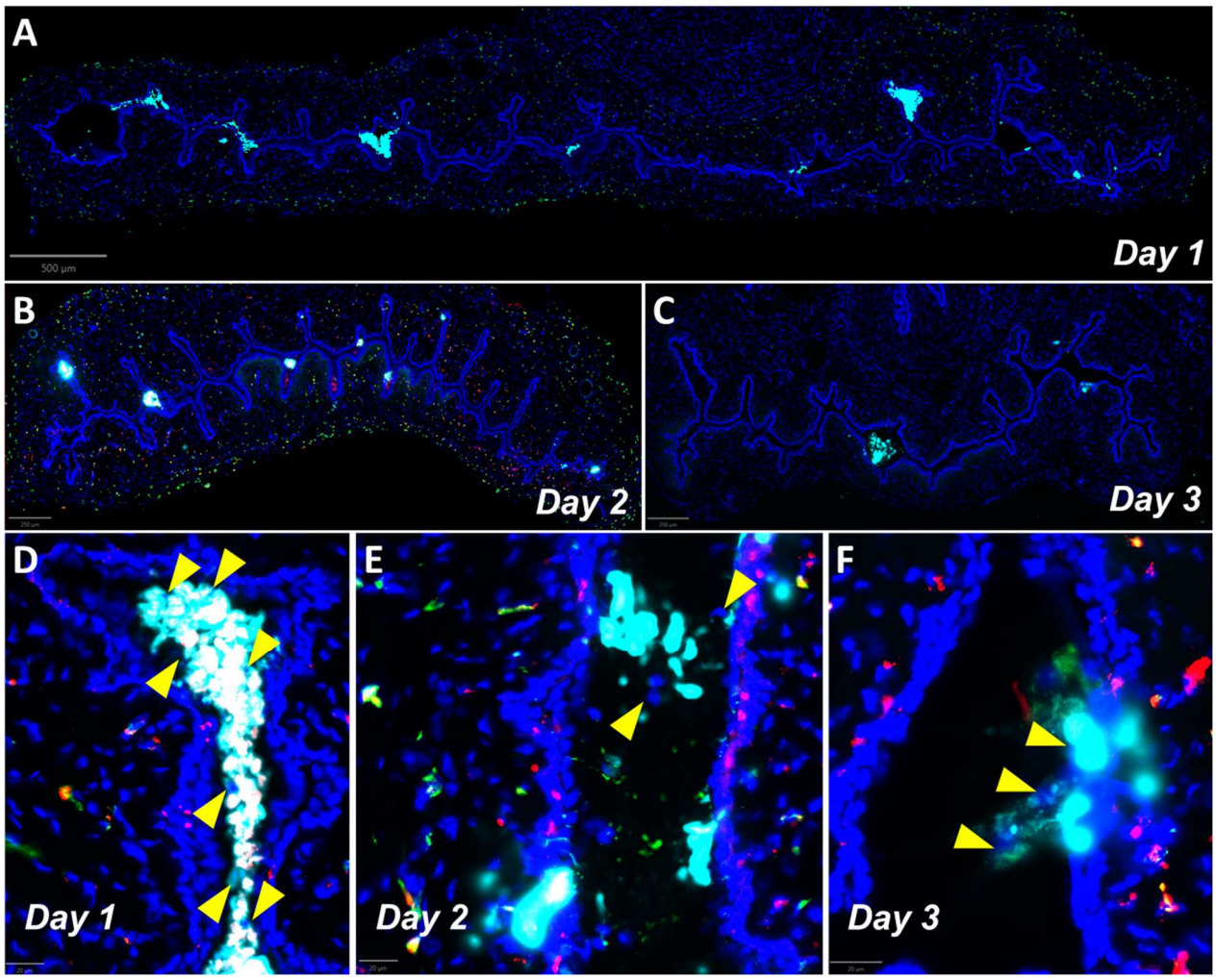


Figure 4.11 Retention of and cellular interaction with vECM at 1, 2, and 3 days post administration

Vaginal tissues were harvested within 3 days post intravaginal administration of fluorescently prelabeled vECM (cyan). Tissue sections were stained against nuclei (DAPI, blue) to assess retention and localization of vECM throughout the vaginal lumen at 1 (A), 2 (B), or 3 (C) days post-administration. Tissue sections were also stained against a pan-macrophage marker (CD68, red) and an anti-inflammatory/pro-regenerative macrophage marker (CD163, green). Cells were observed localizing to vECM in the vaginal lumen, and by 2 and 3 days post-administration, macrophages in particular were observed localized to vECM. Representative fluorescent images are shown for 1 (D), 2 (E), or 3 (F) days post-administration.

Interestingly, we additionally observed vECM localized in subepithelial and fibromuscular vaginal tissues (Figure 4.12). In all events where vECM was observed in

subepithelial tissue, it was directly localized with nuclei, and in almost all of these observations, the nuclei were also colocalized with positive CD68/CD163 staining, indicating that these cells were M2 macrophages. As vECM is too large to passively pass through the vaginal epithelium, and all observations of subepithelial vECM were colocalized with cells – mostly M2 macrophages – it seemed that vECM was being trafficked from the vaginal lumen by cell populations, likely immune.

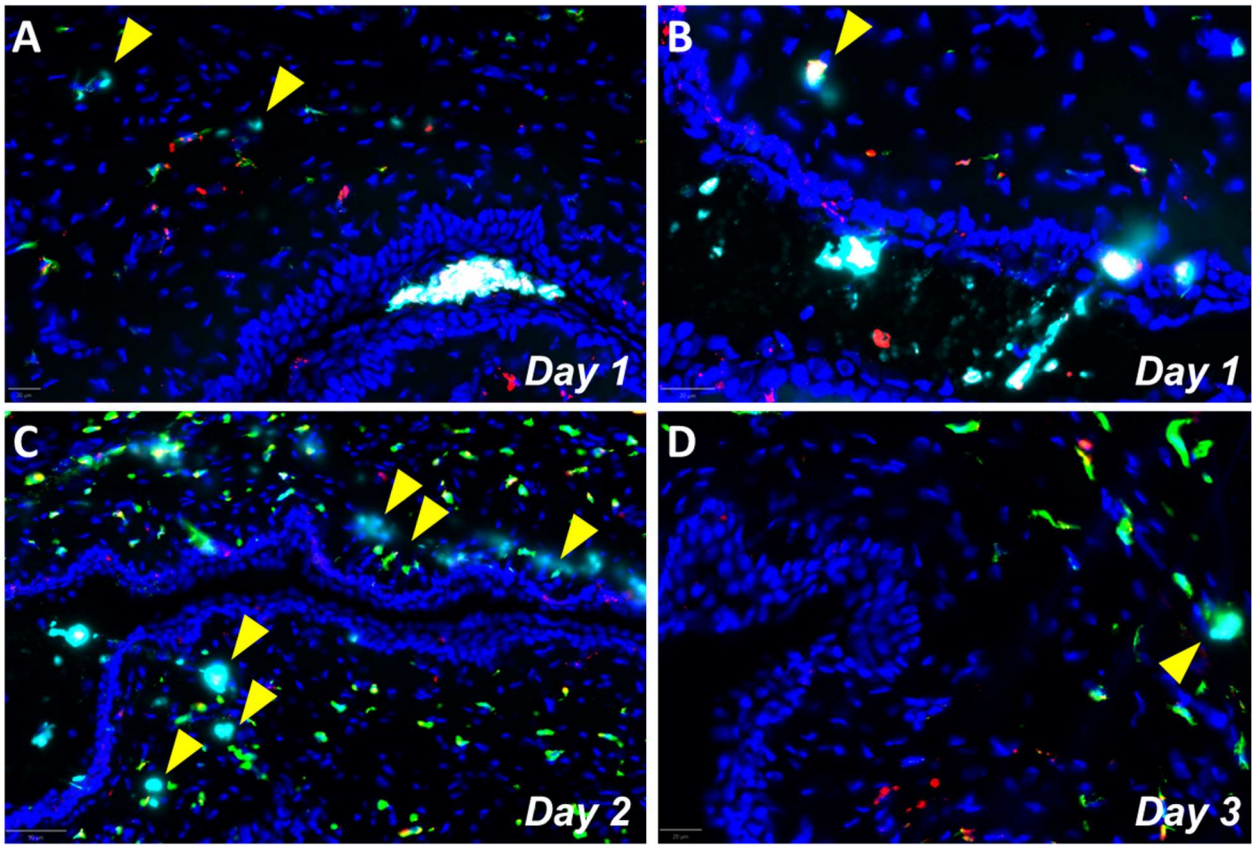


Figure 4.12 vECM is observed colocalized with M2 macrophages and other cells in the vaginal fibromuscularis

Vaginal tissue sections were stained against nuclei (DAPI, blue), a pan-macrophage marker (CD68, red), and an anti-inflammatory/pro-regenerative macrophage marker (CD163, green). vECM (cyan) was observed in subepithelial and fibromuscular tissues, colocalizing with cells and particularly macrophages at 2 and 3 days post-administration. Representative fluorescent images are shown for 1 (A-B), 2 (C), and 3 (D) days post-administration.

To further investigate this observation, tissue sections stained against CD68 and CD163 containing fluorescently prelabeled vECM underwent confocal imaging to assess vECM and macrophage colocalization in higher resolution and determine whether vECM may be intracellular. Confocal imaging of vECM and M2 macrophage colocalization in both the vaginal lumen and fibromuscularis is shown in Figure 4.13. As seen in Figure 4.13A-B, vECM (red) is observed with congregating M2 macrophages (CD163 membrane marker, green) in the vaginal lumen. vECM is further observed in the lamina propria (Figure 4.13A and E) and the fibromuscularis (Figure 4.13D) and is always colocalized with nuclei. Interestingly, vECM appears to be intracellular, bounded by M2 macrophage membrane marker and adjacent to nuclei. In other cases, vECM appears to be colocalized with non-M2 macrophage cells. These confocal images suggest that cells, particularly M2 macrophages, may be involved in the movement of vECM from the vaginal lumen, where it is delivered, to the vaginal lamina propria and fibromuscularis.

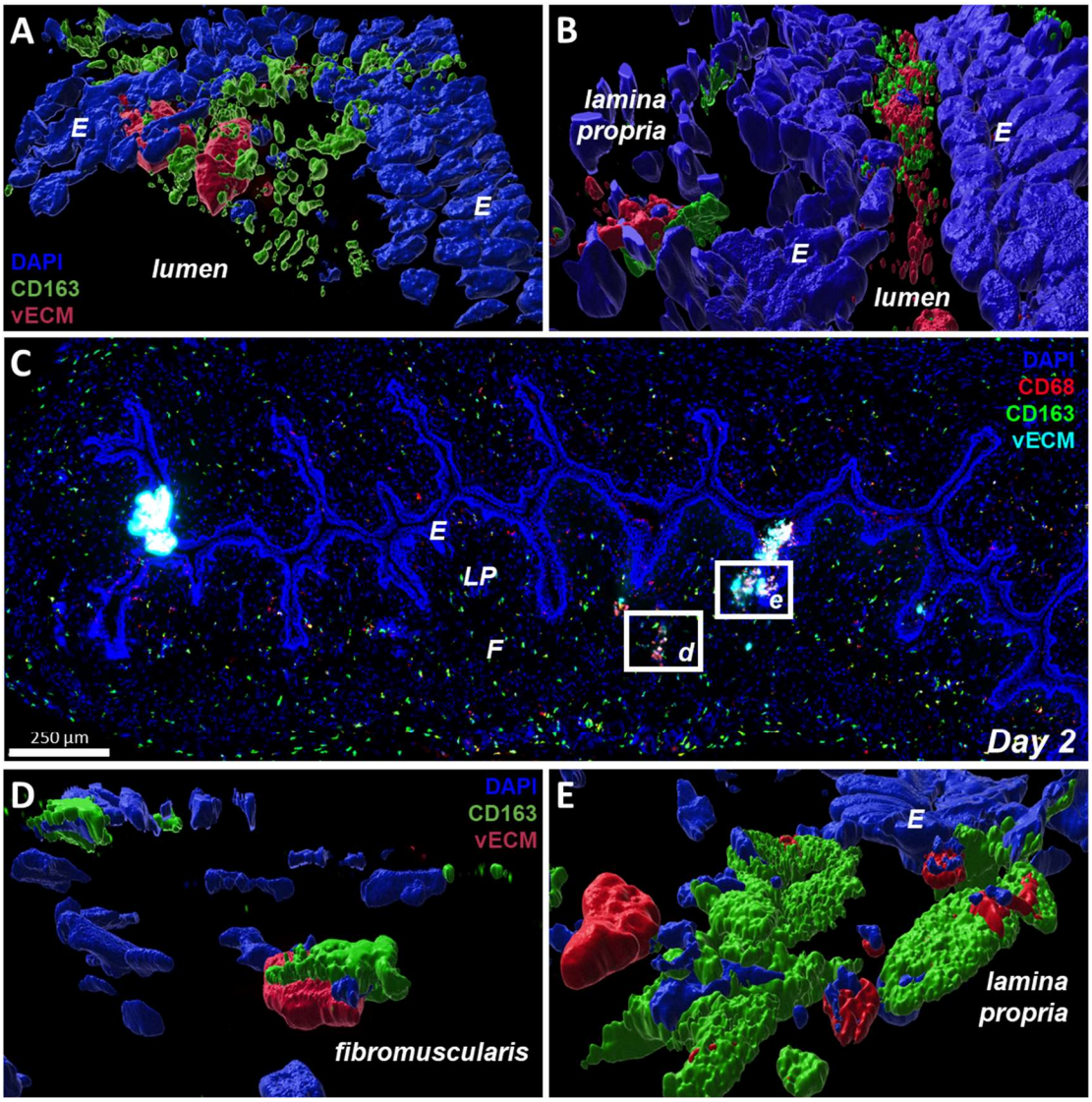


Figure 4.13 Confocal imaging of M2 macrophages with vECM in vaginal lumen and fibromuscularis

Vaginal tissues stained against DAPI (blue), CD68 (red), and CD163 (green) were imaged under confocal microscopy to assess macrophage interactions with vECM (red or cyan [C only]). (A) M2 macrophages ($CD163^{+}$) are observed surrounding vECM in the vaginal lumen. (B) M2 macrophages are again observed surrounding vECM in the vaginal lumen. Additionally, vECM is observed in the lamina propria, appearing to be intracellular – with nuclei embedded in the vECM and M2 macrophage membrane marker surrounding the vECM. (C) Lower magnification immunofluorescent image showing the subepithelial regions where vECM is observed in D and E. (D) vECM is observed in the fibromuscularis, apparently attached to a M2 macrophage membrane. (E) vECM is observed in the lamina propria, with vECM appearing both intracellularly and attached to M2 macrophage membranes.

4.2.5 vECM treatment recruits macrophages to vaginal tissues

Vaginal tissues from the treatment study discussed in sections 4.2.1-3 underwent staining against CD68, a pan-macrophage marker, and CD163, an anti-inflammatory M2 macrophage marker, to assess changes in immune infiltration following treatment. Representative immunofluorescent images for healthy animals (Figure 4.14A) and ovariectomized animals treated with saline (Figure 4.14B), collagen (Figure 4.14C), or 8 mg/mL vECM (Figure 4.14D) are shown. Tissue sections were assessed for density of nuclei, $CD68^+$ nuclei, and $CD163^+$ nuclei within the vaginal lamina propria and fibromuscularis. There was no significant differences among groups in nuclei density (Figure 4.14E), but the vECM group demonstrated significantly greater proportion of macrophages (Figure 4.14F) and M2 macrophage (Figure 4.14G) compared to saline and collagen treatment groups, and vECM was not significantly different from healthy controls in either metric. These data indicate that vECM treatment modulates the immune response in vaginal tissues to a more healthy phenotype.

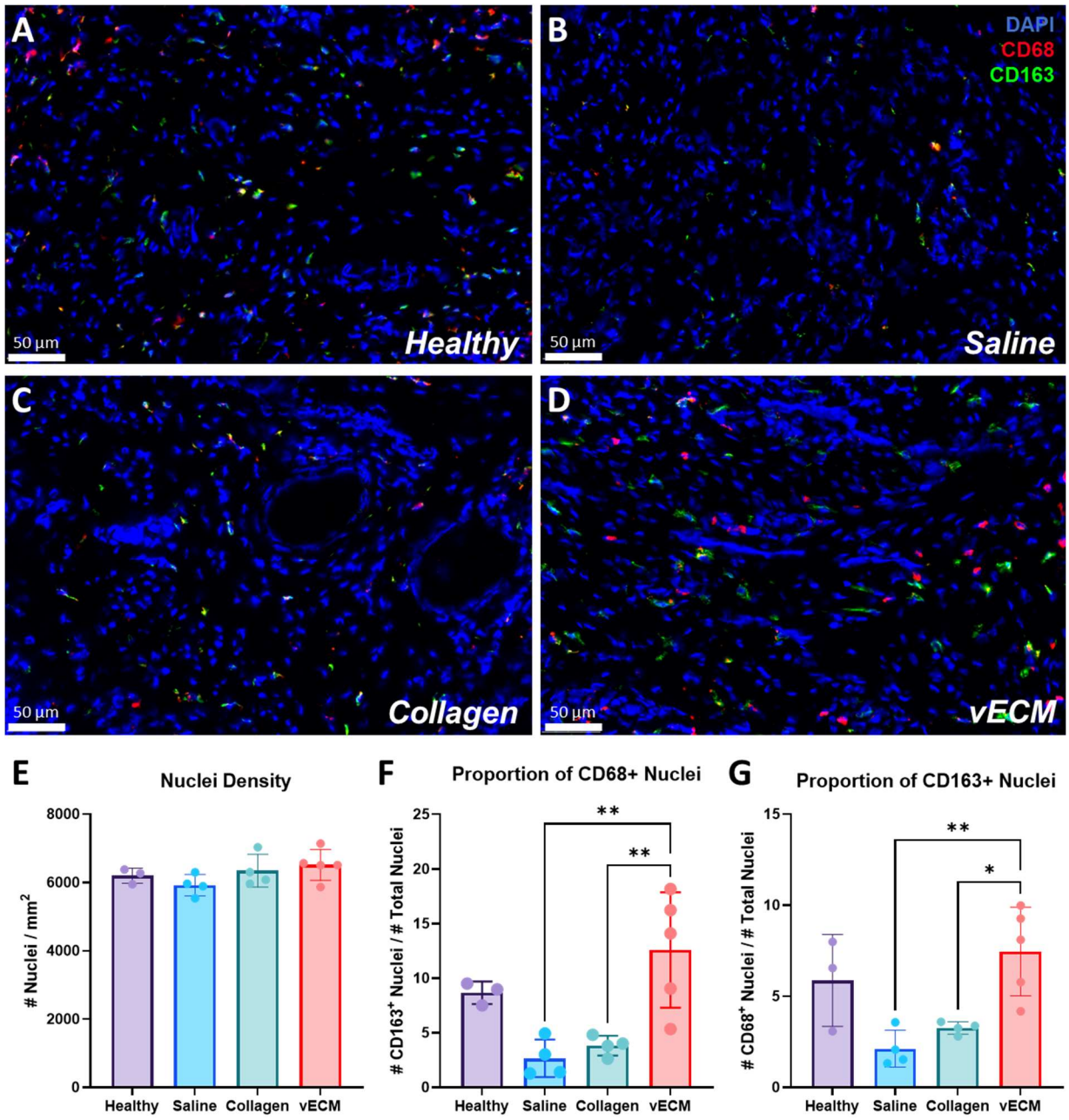


Figure 4.14 Assessment of macrophage infiltration in vaginal tissues after treatment

Vaginal tissue sections were stained against nuclei (DAPI, blue), a pan-macrophage membrane marker (CD68, red), and an M2 macrophage membrane marker (CD163, green). Representative immunofluorescent images are shown for healthy (unperturbed) controls (A) and ovariectomized rats treated with saline (B), collagen (C), or vECM 8 mg/mL (D). Groups were assessed for nuclei density within the lamina propria and muscularis (E), proportion of $CD68^+$ nuclei, indicating macrophages (F), and proportion of $CD163^+$ nuclei, indicating anti-inflammatory M2 macrophages (G).

4.3 Discussion

More than half of menopausal women experience vaginal itching, dryness, pain, and discomfort associated with GSM. However, the only effective and safe treatment available is topically applied estrogen cream, which many patients and providers reject on the basis of hormone-associated cancer risks as well as high costs. Furthermore, topical estrogen cream does not improve the fibromuscular phenotype. Thus, we aimed to develop a nonhormonal, acellular, and easily manufactured tissue regenerative therapeutic as an alternative treatment for all symptoms of vaginal atrophy associated with GSM.

Decellularized ECM biomaterials have demonstrated tissue regenerative capabilities in numerous injury and disease models through mechanisms of cellular recruitment, increased cellular proliferation and differentiation, immune modulation, neovascularization, and ECM remodeling. Additionally, various studies have shown enhanced therapeutic effect through utilizing an ECM source that is matched to the target tissue of interest. Thus, we aimed to develop the first vaginal tissue derived ECM hydrogel and optimized decellularization conditions for this new tissue type. We found that vaginal ECM required a much gentler decellularization with extended water rinsing duration as compared to skeletal and cardiac muscle decellularization. This is likely due to the differences in tissue structure and composition; while muscle tissues are largely composed of cellular content with relatively small amounts of ECM in the interstitial space, vaginal tissue is composed mostly of ECM with relatively little amount of cellular content – mainly the epithelium and smooth muscle. After optimizing decellularization conditions,

vECM was characterized for residual DNA, endotoxin, sulfated glycosaminoglycans, and cytocompatibility; all were within expected values for ECM hydrogels.

vECM was tested for therapeutic efficacy in an established preclinical model of menopause using bilateral ovariectomy in the rat. vECM was administered intravaginally at two doses – 6 and 8 mg/mL – alongside saline and collagen controls daily for a period of two weeks. At the end of treatment duration, we found that the higher dose of vECM demonstrated significant improvement to epithelial thickness as compared to saline and collagen controls and to the lower dose of vECM. Additionally, the 8 mg/mL vECM returned epithelium to a healthy phenotype, as determined by the density of cellular content and proportion of epithelium which was occupied by epithelial stem cells, while saline and collagen controls did not. Interestingly, we found that the intravaginal administration of 8 mg/mL vECM also improved smooth muscle thickness in this model, as compared to saline and collagen controls and the lower dose vECM. Furthermore, we found that 8 mg/mL vECM increased smooth muscle cell proliferation as compared to saline and collagen controls. Finally, 8 mg/mL vECM improved density of macrophages and anti-inflammatory macrophages compared to saline and collagen controls and was not significantly different from healthy controls in these metrics, suggesting that vECM treatment returned the vaginal immune response to a healthy phenotype.

To investigate how vECM yielded therapeutic improvements in the vaginal fibromuscularis despite intravaginal delivery, we assessed the localization and retention of fluorescently prelabeled vECM at 1, 2, and 3 days post-administration. At all timepoints, we observed cellular recruitment to the vECM in the vaginal lumen, and particularly pro-regenerative/anti-inflammatory M2 macrophages were observed localizing to vECM in the

lumen. M2 macrophages were investigated specifically in this study due to the robust literature supporting the interaction between decellularized ECM biomaterials and pro-regenerative macrophages. Surprisingly, we also observed vECM localized in subepithelial tissues – lamina propria and fibromuscularis – and colocalized with cell nuclei at all observations. vECM is too large to passively bypass the vaginal epithelium; as such, we hypothesized that cells may be trafficking vECM through the epithelium and into subepithelial tissues. Indeed, confocal imaging revealed that vECM was observed intracellularly, located within M2 macrophage membrane marker and adjacent to nuclei in areas where vECM was observed in the vaginal lamina propria and fibromuscular layers. While further studies should be conducted to corroborate these findings, this is an exciting new discovery regarding the interactions between decellularized ECM biomaterials and immune cells.

One limitation of this study is that while the bilateral ovariectomy surgical model of menopause does recapitulate the symptoms of vaginal atrophy associated with GSM, it does not incorporate the variable of age, which is intrinsically associated with natural onset of menopause in women. It is known that age can affect the immune response, particularly in how the immune system responds to ECM biomaterials. Thus, it is important to confirm the findings of this study in an aged rat model of menopause. Future studies should additionally test the therapeutic efficacy of vECM doses higher than 8 mg/mL, as so far, we have observed a dose-dependent therapeutic response in this model. Finally, clinical treatment of vaginal atrophy typically involves twice-weekly intravaginal application of estrogen cream; in this study, we assess daily treatment of

vECM. Future studies must investigate different dosing schemes and aim to reach the clinically expected twice-weekly treatment frequency.

4.4 Conclusion

In this study, we developed and characterized the first vaginal tissue-derived decellularized ECM hydrogel. We found that in a rat model of surgical menopause, vECM hydrogel delivered intravaginally at an 8 mg/mL concentration improved epithelial thickness, epithelial phenotype, smooth muscle thickness, and smooth muscle proliferation. Furthermore, we found that cells, particularly M2 macrophages, are recruited to vECM in the vaginal lumen and are observed with intracellular and membrane-attached vECM in the vaginal lamina propria and fibromuscular layers. In conclusion, we have demonstrated the development and application of a novel acellular biomaterial therapeutic for vaginal atrophy associated with GSM.

4.5 Materials and Methods

4.5.1 vECM hydrogel fabrication and characterization

Porcine vaginal tissues were acquired from young female pigs sourced from Midwest Research Swine (Collagen Solutions). Upon arrival, vaginal tissues were processed to remove the cervix from the proximal vagina and any skin tissue from the distal vagina, as well as associated fat, fascia, or other non-vaginal tissues that surrounded the vaginal tube. Several rounds of decellularization optimization were conducted.

In batch vECM-A, porcine vaginal tissues were hand-chopped to 0.5 cm cubes then decellularized in 1% SDS for 5 days, with daily solution changes. Decellularized

tissue then underwent a water rinse for 1 day to remove residual detergent. Tissue was then lyophilized, milled, and passed through a #60 filter.

In batch vECM-B, porcine vaginal tissues were hand-chopped to 0.5 cm cubes then decellularized in either 0.1%, 0.5%, or 1% SDS for 3 days, after which they were rinsed in water for 3 days, with daily changes of either solution or water. Decellularized tissues were lyophilized, milled, and passed through a #60 filter.

In batch vECM-C, porcine vaginal tissues were minced with a commercial meat grinder (Lem Products) then decellularized in 0.1% SDS for 3, 4, or 5 days, followed by a 3 day water rinse. Decellularized tissues were lyophilized, milled, and passed through a #60 filter.

In batch vECM-D, porcine vaginal tissues were minced with a commercial meat grinder then decellularized in 0.1% SDS for 3 days, followed by a 3 day water rinse. Decellularize tissues were lyophilized, milled, and passed through a #60 filter.

For all batches, milled and filter vECM underwent pepsin digestion at a 10 mg ECM/mL pepsin solution in 0.1M HCl for 48 hours. Digested vECM was pH and salt balanced, then incubated at concentrations of 4, 6, or 8 mg/mL at 37°C for 24 hours to test gelation.

The results of batch optimization determined that the conditions of vECM-D decellularization were most suitable. Thus, vECM-D was characterized for residual nuclear material, endotoxin content, sulfated glycosaminoglycans, and cytocompatibility. A PicoGreen (Thermo Fisher) fluorescent assay was used to quantify residual double stranded DNA in vECM. A limulus amebocyte lysate (GenScript) assay was used to quantify endotoxin content in vECM. A 1,9-dimethylmethylene blue assay was used to

quantify sulfated glycosaminoglycan content within vECM. To assess cytocompatibility, either L929 or HUVEC cell lines were encapsulated in 8 mg/mL vECM at a concentration of 200,000 cells/30 µL hydrogel. Encapsulated cells were incubated for 48 hours and observed every 24 hours to assess cellular morphology, migration, and interaction with vECM.

4.5.2 Preparation of vECM and collagen for intravaginal administration

To prepare vECM for intravaginal administration, milled and filtered vECM-D was pepsin digested then pH and salt balanced as described in Section 4.5.1. vECM was then brought to two different concentrations by modulating water addition during the resuspension stage: 6 mg/mL or 8 mg/mL. As a non-tissue specific control, collagen 1 derived from rat tail (Corning) was pH and salt balanced and used at a 6.5 mg/mL concentration in order to match the rheological properties (specifically low-shear rate complex viscosity) of vECM at the 8 mg/mL concentration.

4.5.3 Intravaginal administration of saline, vECM, and collagen

Utilizing a well-established rat model of surgical menopause, young (~3 month) female Sprague Dawley rats underwent bilateral ovariectomy, and the treatment study began two weeks after ovariectomy. For intravaginal administration, ovariectomized animals were first anesthetized under 3% isoflurane then transferred to a nose cone in the supine position. A 1 mL syringe without needle was loaded with 500 µL of saline, collagen, or vECM at 6 mg/mL or 8 mg/mL concentrations (n=4-8/group). The animals were left to rest for 10 minutes, after which they were returned to housing and observed until mobile. These treatments were carried out daily for each animal for a duration of two weeks. The day after the end of treatment, animals were euthanized, and vaginal tissues

were frozen for cryosectioning and subsequent histomorphological analyses. Additional unperturbed and not ovariectomized age matched Sprague Dawley female rats were used as healthy controls (n=3).

4.5.4 Histological assessment of epithelial thickness

For all treatment groups and healthy controls, tissue sections were stained with hematoxylin and eosin. Stained slides were imaged with an Olympus VS200 slide scanning microscope at 20X magnification. For each animal, 5 sections spanning the length of the vagina were sampled. Using QuPath v5 software, for each section, uniform gridlines were superimposed on the tissue cross-section, and 10-15 measurements of epithelial thickness were made where the epithelium intersected the grid. Epithelial measurements were averaged for the section then averaged again across all sections to produce an average epithelial thickness measurement for each animal, which was then used for statistical comparisons.

4.5.5 Histological assessment of epithelial stem cell activity and phenotype

Tissue sections were incubated with DAPI as well as antibodies against p63 (OriGene), an epithelial stem cell transcription factor, with an Alexa Fluor 647 secondary antibody (Invitrogen) and against filaggrin (Biorbyt), a vaginal epithelium membrane marker, with an Alexa Fluor 488 secondary antibody (Invitrogen). Immunofluorescent stained tissue sections were imaged with an Olympus VS200 slide scanning microscope at 40X magnification. Using QuPath v5 software, uniform gridlines were superimposed on 5 tissue sections per animal, sampling throughout the length of the vagina. For each tissue section, five 250 μm x 250 μm grids of epithelium were analyzed. The region of epithelium was traced using positive filaggrin signal. Then, the QuPath cell counter was

used to trace all nuclei within the grid. Finally, the number of nuclei costained with positive p63 signal within the epithelial region was counted. Using these measurements, three metrics were used to assess epithelial phenotype: density of cells within the epithelium (number of nuclei normalized by epithelium region area), density of epithelial stem cells within the epithelium (number of $p63^+$ nuclei normalized by epithelium region area), and proportion of epithelial stem cells (number of $p63^+$ nuclei normalized by total number of nuclei within the epithelium region area). For all metrics, data from all 5 regions were averaged per section then averaged again across all sections to produce an average measurement for each animal, which was then used for statistical comparisons.

4.5.6 Histological assessment of smooth muscle thickness and proliferation

Tissue sections were incubated with DAPI as well as antibodies against alpha smooth muscle actin (Dako), a smooth muscle marker, with an Alexa Fluor 568 secondary antibody (Invitrogen) and against Ki67 (Abcam), a nuclear marker for proliferating cells, with an Alexa Fluor 647 secondary antibody (Invitrogen). Immunofluorescent stained tissue sections were imaged with an Olympus VS200 slide scanning microscope at 40X magnification.

For analysis of smooth muscle thickness, using QuPath v5 software, uniform gridlines were superimposed on the tissue cross-sections. For each section, 10-15 measurements of smooth muscle thickness were made where the smooth muscle layer intersected the grid, and 5 tissue sections were analyzed per animal. Smooth muscle thickness measurements were averaged for the section then averaged again across 5 sections to produce an average smooth muscle thickness measurement for each animal, which was then used for statistical comparisons.

For analysis of smooth muscle proliferation, for each tissue section five 250 μm x 250 μm grids of epithelium were analyzed, and 5 tissue sections were analyzed per animal. The region of smooth muscle within the grid was traced, then QuPath positive cell counter was used to count the number of nuclei within the smooth muscle region as well as the number of $Ki67^+$ nuclei within the smooth muscle region. Using these measurements, smooth muscle proliferation was quantified by normalizing the proportion of $Ki67^+$ nuclei by the total number of nuclei within the smooth muscle regions. Data from all 5 regions were averaged per section then averaged again across all sections to produce an average measurement for each animal, which was then used for statistical comparisons.

4.5.7 Histological assessment of macrophage infiltration and phenotype after treatment

Tissue sections were incubated with DAPI as well as antibodies against CD68 (Abcam), a pan-macrophage membrane marker, with an Alexa Fluor 568 secondary antibody (Invitrogen) and against CD163 (BioRad), an anti-inflammatory M2 macrophage membrane marker, with an Alexa Fluor 488 secondary antibody (Invitrogen). Immunofluorescent stained tissue sections were imaged with an Olympus VS200 slide scanning microscope at 40X magnification.

For analysis of macrophage density in vaginal tissues, using QuPath v5 software, uniform gridlines were superimposed on the tissue cross-sections. For each tissue section five 250 μm x 250 μm grids of epithelium were analyzed, and 5 tissue sections were analyzed per animal. These grids were placed with only the DAPI channel visible, and were placed such that the entire grid covered lamina propria and fibromuscular tissue – vaginal epithelium was excluded from study. The QuPath positive cell counter was used

to count the total number of nuclei, the number of $CD68^+$ nuclei, and the number of $CD163^+$ nuclei within each grid. Data from all 5 regions were averaged per section then averaged again across all sections to produce an average measurement for each animal, which was then used for statistical comparisons.

4.5.8 Intravaginal administration of fluorescently prelabeled vECM and macrophage staining at early timepoints

To assess retention and localization of vECM in the vagina, vECM was prepared for intravaginal administration as previously described. One hour before administration, vECM was mixed with an NHS Succinimidyl Ester fluorescently tagged with Alexa Fluor 647. After mixing the fluorescent tag with vECM, the suspension was incubated at room temperature for 1 hour to ensure complete binding of the dye to free amines within the vECM.

Ovariectomized rats, two weeks after the procedure, were anesthetized with 3% isoflurane then transferred to a nose cone in the supine position. 500 µL of fluorescently prelabeled vECM was administered intravaginally with a syringe, aided by water-soluble lubricant. The rats were rested on the nose cone for 10 minutes, after which they were returned to housing and observed until mobile. Rats were survived for 1, 2, or 3 days after intravaginal administration, at which point animals were euthanized and vaginal tissues were frozen for histomorphological analysis (n=3/timepoint).

Frozen tissues were cryosectioned then stained against CD68 and CD163 as described in section 4.5.7. Immunofluorescently stained tissue sections were imaged with an Olympus VS200 slide scanning microscope and with a Dragonfly confocal microscope.

4.5.9 Statistical analysis

All statistical analysis was completed utilizing GraphPad Prism version 10.2. For all analyses, a one-way ANOVA with Tukey's post-hoc multiple comparisons test was used to determine statistically significant differences between all groups.

4.6 Acknowledgements

Chapter 4, in part is currently being prepared for submission for publication of the material. Emma I. Zelus, Marianna Alperin, Karen L. Christman. The dissertation author was the primary researcher and author of this material.

Chapter 5: Conclusions and Future Directions

5.1 Summary of Work

This dissertation presents a thorough investigation of the therapeutic potential of decellularized ECM hydrogels in translationally relevant models of clinically underserved soft tissue disorders. ECM hydrogels sourced from skeletal muscle were investigated for the regeneration of tongue tissue following surgical resection and of the EUS following SBI, and a novel ECM hydrogel sourced from vaginal tissue was developed and applied for treatment of vaginal atrophy associated with GSM.

The first chapter reviewed the history of decellularized ECM biomaterials and presented a thorough overview of decellularization methods, specifically from the perspective of understanding their benefits and drawbacks with regards to manufacturing processes, scalability, and clinical translation. It provides a comprehensive review of decellularized ECM biomaterials that have been used clinically, including their source tissue and clinical application, and demonstrates that overwhelmingly, the decellularized ECM materials used clinically are sheets, grafts, patches, and similar. ECM biomaterials which require further processing, such as powders and hydrogels, are relatively unexplored clinically, providing ample opportunity for research within this space. This chapter goes on to discuss the mechanisms by which decellularized ECM biomaterials induce tissue repair and regeneration, as shown through both clinical and preclinical studies. This chapter provides the rationale for the research to follow, which applies knowledge of decellularization techniques, clinical application, and mechanisms of pro-repair to engineer decellularized ECM hydrogels for novel applications in highly translational disease models.

The second chapter presents the use of a decellularized skeletal muscle derived ECM hydrogel for tissue regeneration in a model of tongue fibrosis due to partial glossectomy. Clinically, patients recovering from head and neck cancer treatment, which include surgical resection and radiation, are likely to experience tongue fibrosis and atrophy, leading to tongue dysphagia. The SKM hydrogel, given previous research, is well suited to promote tissue repair in this model of skeletal muscle injury. Indeed, this chapter demonstrates that the SKM hydrogel reduces scar formation, improves muscle regeneration, and transiently increases neovascularization in a translational rat model of surgical resection. Furthermore, mechanistic studies utilizing both targeted and unbiased gene expression experimental approaches demonstrate that the SKM hydrogel is immunomodulatory and induces a pro-regenerative immune response particularly in macrophages. Finally, this chapter provides novel evidence that SKM hydrogel recruits fibroadipogenic progenitors, which mediate interactions with pro-regenerative immune response to stimulate muscle regeneration. Thus, this chapter demonstrates that the SKM hydrogel is a promising option for future clinical translation in the regeneration of tongue muscle and treatment of dysphagia.

The third chapter investigates an array of translational preclinical models of SUI in the rat, including single SBI, repeated SBI, retired breeder, and ovariectomy models. It shows the progression of urethral function recovery in these different models, establishing that none are a completely reliable model of SUI contrary to what is presented in the literature. It further demonstrates that there is no deficit in EUS morphology in any models, suggesting that there is not necessarily a direct correlation between EUS morphology and urethral function in the rat. Using this data, the single SBI model was selected as the most

economical and consistent model of SUI in which to test the therapeutic potential of SKM injection for EUS regeneration and urethral function improvement. After optimizing injection volumes to the EUS for safety and feasibility, an initial study investigated the therapeutic efficacy of SKM hydrogel injection compared to saline and found no differences in urethral function or EUS morphology outcomes between injection groups. Overall, this chapter provides a comprehensive study of different preclinical models for SUI that have been previously suggested in the literature and enables further translational studies investigating novel injectable therapeutics for treatment of SUI.

The fourth chapter details the development of a novel porcine vaginal tissue derived ECM hydrogel, vECM, along with manufacturing conditions and characterization. It then presents results from studies assessing the therapeutic efficacy of vECM when administered daily in a rat model of surgical menopause. This chapter demonstrates that vECM improves vaginal epithelial thickness and restores the epithelium to a healthy phenotype. Furthermore, vECM improves smooth muscle thickness despite only being administered intravaginally, and vECM increases smooth muscle proliferation. This chapter explores potential mechanisms underpinning these surprising results and shows that immune cells, particularly macrophages, are observed interacting with vECM in the vaginal lumen and associated with vECM intracellularly in the vaginal fibromuscularis. It further demonstrates that vECM treatment increases macrophage and pro-regenerative M2 macrophage density in vaginal tissues. Overall, this chapter presents a novel, promising, and highly translatable ECM hydrogel therapeutic for treatment of vaginal atrophy associated with GSM.

Overall, the studies presented within this dissertation demonstrate the expansive translational potential of ECM hydrogels. As discussed in the introduction, ECM patches and sheets are widely used clinically, paving the way for more advanced forms of ECM biomaterials that may be used in more diverse applications. Herein, ECM hydrogels are applied in three different highly translatable and novel therapeutic applications, utilizing established mechanisms of pro-repair and even demonstrating new mechanisms through which ECM hydrogels can mediate tissue regeneration.

5.2 Future Directions and Outlooks

To continue development and eventual translation of ECM hydrogels for the regeneration of various soft tissue disorders discussed in this thesis, there are many avenues for potential exploration.

For the continuation of research on ECM hydrogels for tissue regeneration in a model of tongue fibrosis, it is possible that repeated injections of the SKM hydrogel may yield more complete scar remission and muscle regeneration in the tongue tissue. Furthermore, this model may be modulated to be more reflective of clinical pathophysiology by introducing a combinatorial surgical resection and radiation injury. Especially considering that we could not produce functional differences in tongue active force production with the partial glossectomy alone, the use of a more severe model which may produce a deficit in tongue function may increase the translational potential of the SKM hydrogel for this application. Additionally, other means of assessing tongue function, such as radiation swallow procedure protocols explored by other groups, may be coadapted for assessment of the therapeutic potential of SKM.

For the application of SKM hydrogel in treatment of SUI, much work remains to be done. In the present studies, SKM hydrogel did not demonstrate significant improvement in urethral function as compared to saline. However, we did develop an effective delivery modality for injectable therapeutics to the EUS for treatment of SUI. Thus, future studies may investigate the efficacy of SKM delivered at smaller doses or at later timepoints to avoid potential deleterious effects to the urethral tissues. Additionally, the ECM hydrogel may be combined with cellular therapies, which have already entered clinical investigation for treatment of SUI, to produce a stronger combined therapeutic effect. Finally, other injectable acellular biomaterials could be explored as an alternative to ECM hydrogels. For example, MAP hydrogels have demonstrated tissue regenerative potential, and given their increased stiffness and rheological characteristics compared to ECM hydrogel, they may serve as both a bulking agent to improve urethral continence in the short-term as well as a tissue regenerative agent to address the underlying pathophysiology of SUI.

For the application of vECM hydrogel in treating vaginal atrophy associated with GSM, the research presented in this dissertation is only an early investigation of an extremely promising novel therapeutic application for ECM hydrogels. Additional higher doses of vECM may be tested, as we have already shown a dose-dependent therapeutic response to vECM in this model. Furthermore, non-tissue specific ECM hydrogels, such as SKM or cardiac tissue derived ECM, should be assessed in the rat model of menopause to assess whether the observed regeneration can be achieved without a tissue-specific ECM hydrogel. It will be necessary to compare the therapeutic effect of vECM to a dose-matched treatment of topical estrogen cream, which is the current standard of care clinically. Additionally, in order to align with patient care expectations,

vECM treatment should be optimized to allow for twice-weekly treatment, rather than daily treatment, which would be prohibitively laborious and expensive for patients. Finally, given the exciting and promising therapeutic potential of the vECM hydrogel, we may test the application of vECM in other vaginal tissue disorders, such as vaginal fibrosis following vaginal irradiation, which frequently afflicts cervical cancer patients.

In summary, ECM hydrogels have demonstrated remarkable potential for tissue regeneration in a variety of soft tissue disorders, and their translational potential is further improved by the minimally invasive and versatile delivery enabled by the hydrogel form. The research presented in this dissertation pave the way for future translational studies utilizing ECM hydrogels for tissue regeneration.

REFERENCES

1. Theocharis, A. D., Skandalis, S. S., Gialeli, C. & Karamanos, N. K. Extracellular matrix structure. *Adv Drug Deliv Rev* **97,** 4–27 (2016).

2. Lantz, G. C., Badylak, S. F., Coffey, A. C., Geddes, L. A. & Blevins, W. E. Small intestinal submucosa as a small-diameter arterial graft in the dog. *J Invest Surg* **3,** 217–227 (1990).

3. Voytik-Harbin, S. L., Brightman, A. O., Waisner, B. Z., Robinson, J. P. & Lamar, C. H. Small intestinal submucosa: A tissue-derived extracellular matrix that promotes tissue-specific growth and differentiation of cells in vitro. *Tissue Eng* **4,** 157–174 (1998).

4. Zhang, Y., Xu, Y. & Gao, J. The engineering and application of extracellular matrix hydrogels: a review. *Biomater Sci* **11,** 3784–3799 (2023).

5. McInnes, A. D., Moser, M. A. J. & Chen, X. Preparation and Use of Decellularized Extracellular Matrix for Tissue Engineering. *Journal of Functional Biomaterials 2022, Vol. 13, Page 240* **13,** 240 (2022).

6. Nicholls, D. L., Rostami, S., Karoubi, G. & Haykal, S. Perfusion decellularization for vascularized composite allotransplantation. *SAGE Open Med* **10,** (2022).

7. Phillips, M., Maor, E. & Rubinsky, B. Nonthermal irreversible electroporation for tissue decellularization. *J Biomech Eng* **132,** (2010).

8. Gilbert, T. W., Sellaro, T. L. & Badylak, S. F. Decellularization of tissues and organs. *Biomaterials* **27,** 3675–3683 (2006).

9. Seo, Y., Jung, Y. & Kim, S. H. Decellularized heart ECM hydrogel using supercritical carbon dioxide for improved angiogenesis. *Acta Biomater* **67,** 270–281 (2018).

10. Alshaikh, A. B., Padma, A. M., Dehlin, M., Akouri, R., Song, M. J., Brännström, M. & Hellström, M. Decellularization and recellularization of the ovary for bioengineering applications; Studies in the mouse. *Reproductive Biology and Endocrinology* **18,** 1–10 (2020).

11. Crapo, P. M., Gilbert, T. W. & Badylak, S. F. An overview of tissue and whole organ decellularization processes. *Biomaterials* **32,** 3233 (2011).

12. Lumpkins, S. B., Pierre, N. & McFetridge, P. S. A mechanical evaluation of three decellularization methods in the design of a xenogeneic scaffold for tissue engineering the temporomandibular joint disc. *Acta Biomater* **4,** 808–816 (2008).

13. Wainwright, J. M., Czajka, C. A., Patel, U. B., Freytes, D. O., Tobita, K., Gilbert, T. W. & Badylak, S. F. Preparation of Cardiac Extracellular Matrix from an Intact Porcine Heart. *Tissue Eng Part C Methods* **16,** 525 (2010).

14. Keane, T. J., Londono, R., Carey, R. M., Carruthers, C. A., Reing, J. E., Dearth, C. L., D'Amore, A., Medberry, C. J. & Badylak, S. F. Preparation and Characterization of a Biologic Scaffold from Esophageal Mucosa. *Biomaterials* **34,** 6729 (2013).

15. Gilpin, A. & Yang, Y. Decellularization Strategies for Regenerative Medicine: From Processing Techniques to Applications. *Biomed Res Int* **2017,** (2017).

16. Zhang, W., Du, A., Liu, S., Lv, M. & Chen, S. Research progress in decellularized extracellular matrix-derived hydrogels. *Regen Ther* **18,** 88–96 (2021).

17. Petrie, K., Cox, C. T., Becker, B. C. & MacKay, B. J. Clinical applications of acellular dermal matrices: A review. *Scars Burn Heal* **8,** 205951312110383 (2022).

18. Parmaksiz, M., Dogan, A., Odabas, S., Elçin, A. E. & Elçin, Y. M. Clinical applications of decellularized extracellular matrices for tissue engineering and regenerative medicine. *Biomedical Materials* **11,** 022003 (2016).

19. Costa, A., Naranjo, J. D., Londono, R. & Badylak, S. F. Biologic Scaffolds. doi:10.1101/cshperspect.a025676

20. Iorio, T. & Blumberg, D. Short-Term Results of Treating Primary and Recurrent Anal Fistulas with a Novel Extracellular Matrix Derived from Porcine Urinary Bladder. *https://doi.org/10.1177/000313481508100532* **81,** 498–502 (2015).

21. Kruper, G. J., VandeGriend, Z. P., Lin, H.-S. & Zuliani, G. F. Salvage of failed local and regional flaps with porcine urinary bladder extracellular matrix aided tissue regeneration. *Case Rep Otolaryngol* **2013,** 1–5 (2013).

22. Rommer, E. A., Peric, M. & Wong, A. Urinary bladder matrix for the treatment of recalcitrant nonhealing radiation wounds. *Adv Skin Wound Care* **26,** 450–455 (2013).

23. LeCheminant, J. & Field, C. Porcine urinary bladder matrix: a retrospective study and establishment of protocol. *J Wound Care* **21,** 476–482 (2012).

24. InnovaMatrix PD - Convatec Triad Life Sciences, LLC. at <https://innovamatrix.com/innovamatrix-pd/>

25. Spang, M. T. & Christman, K. L. Extracellular matrix hydrogel therapies: In vivo applications and development. *Acta Biomater* **68,** 1–14 Preprint at https://doi.org/10.1016/j.actbio.2017.12.019 (2018)

26. Traverse, J. H., Henry, T. D., Dib, N., Patel, A. N., Pepine, C., Schaer, G. L., DeQuach, J. A., Kinsey, A. M., Chamberlin, P. & Christman, K. L. First-in-Man Study

of a Cardiac Extracellular Matrix Hydrogel in Early and Late Myocardial Infarction Patients. *JACC Basic Transl Sci* **4,** 659–669 (2019).

27. Golebiowska, A. A., Intravaia, J. T., Sathe, V. M., Kumbar, S. G. & Nukavarapu, S. P. Decellularized extracellular matrix biomaterials for regenerative therapies: Advances, challenges and clinical prospects. *Bioact Mater* **32,** 98 (2024).

28. Neishabouri, A., Soltani Khaboushan, A., Daghigh, F., Kajbafzadeh, A. M. & Majidi Zolbin, M. Decellularization in Tissue Engineering and Regenerative Medicine: Evaluation, Modification, and Application Methods. *Front Bioeng Biotechnol* **10,** (2022).

29. Xiao, H., Chen, X., Liu, X., Wen, G. & Yu, Y. Recent advances in decellularized biomaterials for wound healing. *Mater Today Bio* **19,** 100589 (2023).

30. Toprakhisar, B., Verfaillie, C. M. & Kumar, M. Advances in Recellularization of Decellularized Liver Grafts with Different Liver (Stem) Cells: Towards Clinical Applications. *Cells* **12,** (2023).

31. Willemse, J., van Tienderen, G., van Hengel, E., Schurink, I., van der Ven, D., Kan, Y., de Ruiter, P., Rosmark, O., Westergren-Thorsson G, G., Schneeberger, K., van der Eerden, B., Roest, H., Spee, B., van der Laan, L., de Jonge, J. & Verstegen, M. Hydrogels derived from decellularized liver tissue support the growth and differentiation of cholangiocyte organoids. *Biomaterials* **284,** (2022).

32. Wang, R. M., Mesfin, J. M., Hunter, J., Cattaneo, P., Guimarães-Camboa, N., Braden, R. L., Luo, C., Hill, R. C., Dzieciatkowska, M., Hansen, K. C., Evans, S. & Christman, K. L. Myocardial matrix hydrogel acts as a reactive oxygen species scavenger and supports a proliferative microenvironment for cardiomyocytes. *Acta Biomater* **152,** 47–59 (2022).

33. Hunter, J. D., Mesfin, J. M., Ahmed, T., Chen, A., Reimold, K., Hancko, A., Braden, R. L., Davis, M. E. & Christman, K. L. Myocardial Matrix Hydrogels Mitigate Negative Remodeling and Improve Function in Right Heart Failure Model. *JACC Basic Transl Sci* **9,** 322 (2024).

34. Wolf, M. T., Daly, K. A., Brennan-Pierce, E. P., Johnson, S. A., Carruthers, C. A., D'Amore, A., Nagarkar, S. P., Velankar, S. S. & Badylak, S. F. A hydrogel derived from decellularized dermal extracellular matrix. *Biomaterials* **33,** 7028–7038 (2012).

35. DeQuach, J. A., Lin, J. E., Cam, C., Hu, D., Salvatore, M. A., Sheikh, F. & Christman, K. L. Injectable skeletal muscle matrix hydrogel promotes neovascularization and muscle cell infiltration in a hindlimb ischemia model. *Eur Cell Mater* **23,** 400–412 (2013).

36. Chen, Z., Huang, Y., Xing, H., Tseng, T., Edelman, H., Perry, R. & Kyriakides, T. R. Novel muscle-derived extracellular matrix hydrogel promotes angiogenesis and neurogenesis in volumetric muscle loss. *Matrix Biology* **127,** 38–47 (2024).

37. Diaz, M. D., Tran, E., Spang, M., Wang, R., Gaetani, R., Luo, C. G., Braden, R., Hill, R. C., Hansen, K. C., DeMaria, A. N. & Christman, K. L. Injectable Myocardial Matrix Hydrogel Mitigates Negative Left Ventricular Remodeling in a Chronic Myocardial Infarction Model. *JACC Basic Transl Sci* 1–12 (2021). doi:10.1016/j.jacbts.2021.01.003

38. Duran, P., Sesillo, F. B., Burnett, L., Menefee, S. A., Cook, M., Zazueta-Damian, G., Dzieciatkowska, M., Do, E., French, S., Shah, M. M., Sanvictores, C., Hansen, K. C., Shtrahman, M., Christman, K. L. & Alperin, M. Pro-regenerative Extracellular Matrix Hydrogel Prevents and Mitigates Pathological Alterations of Pelvic Muscles Following Birth Injury. *bioRxiv* 2021.05.28.446170 (2021). doi:10.1101/2021.05.28.446170

39. Evangelista-Leite, D., Carreira, A. C. O., Nishiyama, M. Y., Gilpin, S. E. & Miglino, M. A. The molecular mechanisms of extracellular matrix-derived hydrogel therapy in idiopathic pulmonary fibrosis models. *Biomaterials* **302,** (2023).

40. Hussein, K. H., Park, K. M., Yu, L., Kwak, H. H. & Woo, H. M. Decellularized hepatic extracellular matrix hydrogel attenuates hepatic stellate cell activation and liver fibrosis. *Mater Sci Eng C Mater Biol Appl* **116,** (2020).

41. Wu, X., Kathuria, N., Patrick, C. W. & Reece, G. P. Quantitative analysis of the microvasculature growing in the fibrin interface between a skin graft and the recipient site. *Microvasc Res* **75,** 119–129 (2008).

42. Ungerleider, J. L., Johnson, T. D., Hernandez, M. J., Elhag, D. I., Braden, R. L., Dzieciatkowska, M., Osborn, K. G., Hansen, K. C., Mahmud, E. & Christman, K. L. Extracellular Matrix Hydrogel Promotes Tissue Remodeling, Arteriogenesis, and Perfusion in a Rat Hindlimb Ischemia Model. *JACC Basic Transl Sci* **1,** 32–44 Preprint at https://doi.org/10.1016/j.jacbts.2016.01.009 (2016)

43. Wassenaar, J. W., Gaetani, R., Garcia, J. J., Braden, R. L., Luo, C. G., Huang, D., Demaria, A. N., Omens, J. H. & Christman, K. L. Evidence for Mechanisms Underlying the Functional Benefits of a Myocardial Matrix Hydrogel for Post-MI Treatment. *J Am Coll Cardiol* **67,** 1074 (2016).

44. Spang, M. T., Middleton, R., Diaz, M., Hunter, J., Mesfin, J., Banka, A., Sullivan, H., Wang, R., Lazerson, T. S., Bhatia, S., Corbitt, J., D'Elia, G., Sandoval-Gomez, G., Kandell, R., Vratsanos, M. A., Gnanasekaran, K., Kato, T., Igata, S., Luo, C., Osborn, K. G., Gianneschi, N. C., Eniola-Adefeso, O., Cabrales, P., Kwon, E. J., Contijoch, F., Reeves, R. R., DeMaria, A. N. & Christman, K. L. Intravascularly infused extracellular matrix as a biomaterial for targeting and treating inflamed tissues. *Nat Biomed Eng* **7,** 94 (2023).

45. Diaz, M. D., Kandell, R. M., Wu, J. R., Chen, A., Christman, K. L. & Kwon, E. J. Infusible Extracellular Matrix Biomaterial Promotes Vascular Integrity and Modulates the Inflammatory Response in Acute Traumatic Brain Injury. *Adv Healthc Mater* **12,** 2300782 (2023).

46. Hudson, T. W., Zawko, S., Deister, C., Lundy, S., Hu, C. Y., Lee, K. & Schmidt, C. E. Optimized acellular nerve graft is immunologically tolerated and supports regeneration. *Tissue Eng* **10,** 1641–1651 (2004).

47. Ma, Y. huan, Shi, H. juan, Wei, Q. shuai, Deng, Q. wen, Sun, J. hui, Liu, Z., Lai, B. qin, Li, G., Ding, Y., Niu, W. ting, Zeng, Y. shan & Zeng, X. Developing a mechanically matched decellularized spinal cord scaffold for the in situ matrix-based neural repair of spinal cord injury. *Biomaterials* **279,** 121192 (2021).

48. Kellaway, S. C., Roberton, V., Jones, J. N., Loczenski, R., Phillips, J. B. & White, L. J. Engineered neural tissue made using hydrogels derived from decellularised tissues for the regeneration of peripheral nerves. *Acta Biomater* **157,** 124–136 (2023).

49. de Paula, A. G. P., de Lima, J. D., Bastos, T. S. B., Czaikovski, A. P., dos Santos Luz, R. B., Yuasa, B. S., Smanioto, C. C. S., Robert, A. W. & Braga, T. T. Decellularized Extracellular Matrix: The Role of This Complex Biomaterial in Regeneration. *ACS Omega* **8,** 22256 (2023).

50. McInnes, A. D., Moser, M. A. J. & Chen, X. Preparation and Use of Decellularized Extracellular Matrix for Tissue Engineering. *J Funct Biomater* **13,** (2022).

51. Valentin, J. E., Stewart-Akers, A. M., Gilbert, T. W. & Badylak, S. F. Macrophage Participation in the Degradation and Remodeling of Extracellular Matrix Scaffolds. *Tissue Eng Part A* **15,** 1687 (2009).

52. Fishman, J. M., Lowdell, M. W., Urbani, L., Ansari, T., Burns, A. J., Turmaine, M., North, J., Sibbons, P., Seifalian, A. M., Wood, K. J., Birchall, M. A. & De Coppi, P. Immunomodulatory effect of a decellularized skeletal muscle scaffold in a discordant xenotransplantation model. *Proc Natl Acad Sci U S A* **110,** 14360–14365 (2013).

53. Yu, Y., Zhang, W., Liu, X., Wang, H., Shen, J., Xiao, H., Mei, J., Chai, Y. & Wen, G. Extracellular matrix scaffold-immune microenvironment modulates tissue regeneration. *Compos B Eng* **230,** 109524 (2022).

54. Kasravi, M., Ahmadi, A., Babajani, A., Mazloomnejad, R., Hatamnejad, M. R., Shariatzadeh, S., Bahrami, S. & Niknejad, H. Immunogenicity of decellularized extracellular matrix scaffolds: a bottleneck in tissue engineering and regenerative medicine. *Biomater Res* **27,** (2023).

55. Loffredo, L. F., Savage, T. M., Ringham, O. R. & Arpaia, N. Treg–tissue cell interactions in repair and regeneration. *J Exp Med* **221,** (2024).

56. Allman, A. J., McPherson, T. B., Badylak, S. F., Merrill, L. C., Kallakury, B., Sheehan, C., Raeder, R. H. & Metzger, D. W. Xenogeneic extracellular matrix grafts elicit a TH2-restricted immune response. *Transplantation* **71,** 1631–1640 (2001).

57. Moore, E. M., Maestas, D. R., Cherry, C. C., Garcia, J. A., Comeau, H. Y., Huyer, L. D., Kelly, S. H., Peña, A. N., Blosser, R. L., Rosson, G. D. & Elisseeff, J. H. Biomaterials direct functional B cell response in a material-specific manner. *Sci Adv* **7,** 5830 (2021).

58. Wang, R. M., Mesfin, J. M., Karkanitsa, M., Ungerleider, J. L., Zelus, E., Zhang, Y., Kawakami, Y., Kawakami, Y., Kawakami, T. & Christman, K. L. Immunomodulatory contribution of mast cells to the regenerative biomaterial microenvironment. *NPJ Regen Med* **8,** (2023).

59. Dellis, S., Papadopoulou, S., Krikonis, K. & Zigras, F. Sarcopenic Dysphagia. A Narrative Review. *J Frailty Sarcopenia Falls* **03,** 1–7 (2018).

60. Pauloski, B. R. Rehabilitation of Dysphagia Following Head and Neck Cancer. doi:10.1016/j.pmr.2008.05.010

61. García-Peris, P., Parón, L., Velasco, C., de la Cuerda, C., Camblor, M., Bretón, I., Herencia, H., Verdaguer, J., Navarro, C. & Clave, P. Long-term prevalence of oropharyngeal dysphagia in head and neck cancer patients: Impact on quality of life. *Clinical Nutrition* **26,** 710–717 (2007).

62. Hyo Choi, K., Ri Son, Y. & Gyun Kim, T. Dysphagia in Tongue Cancer Patients. *Annals of Rehabilitation Medicine Original Article Ann Rehabil Med* **39,** 210–217 (2015).

63. Nguyen, N. P., Moltz, C. C., Frank, C., Vos, P., Smith, H. J., Karlsson, U., Dutta, S., Midyett, F. A., Barloon, J. & Sallah, S. Dysphagia following chemoradiation for locally advanced head and neck cancer. *Annals of Oncology* **15,** 383–388 (2004).

64. Langmore, S. E. & Pisegna, J. M. Efficacy of exercises to rehabilitate dysphagia: A critique of the literature. *Int J Speech Lang Pathol* **17,** 222–229 (2015).

65. Tran, E. K., Juarez, K. O. & Long, J. L. Stem cell treatments for oropharyngeal dysphagia: Rationale, benefits, and challenges. *World J Stem Cells* **12,** 1001–1012 (2020).

66. Vahabzadeh-Hagh, A. M., Goel, A. N., Frederick, J. W., Berke, G. S. & Long, J. L. Transplanted Human Multipotent Stromal Cells Reduce Acute Tongue Fibrosis in Rats. (2018). doi:10.1002/lio2.202

67. Nativ-Zeltzer, N., Kuhn, M. A., Evangelista, L., Anderson, J. D., Nolta, J. A., Gregory, ; D, Canestrari, E., Jankowski, R. J. & Belafsky, P. C. Autologous Muscle-Derived Cell Therapy for Swallowing Impairment in Patients Following Treatment for Head and Neck Cancer. (2021). doi:10.1002/lary.29606

68. Rao, N., Agmon, G., Tierney, M. T., Ungerleider, J. L., Braden, R. L., Sacco, A. & Christman, K. L. Engineering an Injectable Muscle-Specific Microenvironment for

Improved Cell Delivery Using a Nanofibrous Extracellular Matrix Hydrogel. *ACS Nano* **11,** 3851–3859 (2017).

69. Seif-Naraghi, S. B., Singelyn, J. M., Salvatore, M. A., Osborn, K. G., Wang, J. J., Sampat, U., Kwan, O. L., Strachan, G. M., Wong, J., Schup-Magoffin, P. J., Braden, R. L., Bartels, K., DeQuach, J. A., Preul, M., Kinsey, A. M., DeMaria, A. N., Dib, N. & Christman, K. L. Safety and Efficacy of an Injectable Extracellular Matrix Hydrogel for Treating Myocardial Infarction. *Sci Transl Med* **5,** 173ra25 LP-173ra25 (2013).

70. Nezhad, Z. M., Poncelet, A., De Kerchove, L., Gianello, P., Fervaille, C. & Khoury, G. El. Small intestinal submucosa extracellular matrix (CorMatrix®) in cardiovascular surgery: a systematic review. *Z.Mosala Nezhad)* (2016). doi:10.1093/icvts/ivw020

71. Sarrafian, T. L., Bodine, S. C., Murphy, B., Grayson, J. K. & Stover, S. M. Extracellular matrix scaffolds for treatment of large volume muscle injuries: A review. *Veterinary Surgery* **47,** 524–535 (2018).

72. Hernandez, M. J., Zelus, E. I., Spang, M. T., Braden, R. L. & Christman, K. L. Dose optimization of decellularized skeletal muscle extracellular matrix hydrogels for improving perfusion and subsequent validation in an aged hindlimb ischemia model. *Biomater Sci* **8,** 3511–3521 (2020).

73. Lu, H., Huang, D., Ransohoff, R. M. & Zhou, L. Acute skeletal muscle injury: CCL2 expression by both monocytes and injured muscle is required for repair. *The FASEB Journal* **25,** 3344 (2011).

74. Reichel, C. A., Rehberg, M., Lerchenberger, M., Berberich, N., Bihari, P., Khandoga, A. G., Zahler, S. & Krombach, F. Ccl2 and Ccl3 mediate neutrophil recruitment via induction of protein synthesis and generation of lipid mediators. *Arterioscler Thromb Vasc Biol* **29,** 1787–1793 (2009).

75. Deng, B., Wehling-Henricks, M., Villalta, S. A., Wang, Y. & Tidball, J. G. Interleukin-10 triggers changes in macrophage phenotype that promote muscle growth and regeneration. *J Immunol* **189,** 3669 (2012).

76. Kang, X., Yang, M. Y., Shi, Y. X., Xie, M. M., Zhu, M., Zheng, X. L., Zhang, C. K., Ge, Z. L., Bian, X. T., Lv, J. T., Wang, Y. J., Zhou, B. H. & Tang, K. L. Interleukin-15 facilitates muscle regeneration through modulation of fibro/adipogenic progenitors. *Cell Communication and Signaling* **16,** 1–11 (2018).

77. Kuswanto, W., Burzyn, D., Panduro, M., Wang, K. K., Jang, Y. C., Wagers, A. J., Benoist, C. & Mathis, D. Poor repair of skeletal muscle in aging mice reflects a defect in local, interleukin-33-dependent, accumulation of regulatory T cells. *Immunity* **44,** 355 (2016).

78. Varga, T., Mounier, R., Patsalos, A., Gogolák, P., Peloquin, M., Horvath, A., Pap, A., Daniel, B., Nagy, G., Pintye, E., Poliska, S., Cuvellier, S., Ben Larbi, S.,

Sansbury, B. E., Spite, M., Brown, C. W., Chazaud, B. & Nagy, L. Macrophage PPARγ, a Lipid Activated Transcription Factor Controls the Growth Factor GDF3 and Skeletal Muscle Regeneration. (2016). doi:10.1016/j.immuni.2016.10.016

79. Alfaro, M. P., Deskins, D. L., Wallus, M., Dasgupta, J., Davidson, J. M., Nanney, L. B., Guney, M. A., Gannon, M. & Young, P. P. A physiological role for connective tissue growth factor in early wound healing. *Laboratory Investigation* **93,** 81–95 (2012).

80. Alameddine, H. S. & Morgan, J. E. Matrix Metalloproteinases and Tissue Inhibitor of Metalloproteinases in Inflammation and Fibrosis of Skeletal Muscles. *J Neuromuscul Dis* **3,** 455–473 (2016).

81. Coletti, D., Mccarthy, J. J., Scicchitano, B. M., Mozzetta, C., Madaro, L., Biferali, B. & Proietti, D. Fibro-Adipogenic Progenitors Cross-Talk in Skeletal Muscle: The Social Network. (2019). doi:10.3389/fphys.2019.01074

82. Wosczyna, M. N., Biswas, A. A., Cogswell, C. A. & Goldhamer, D. J. Multipotent progenitors resident in the skeletal muscle interstitium exhibit robust BMP-dependent osteogenic activity and mediate heterotopic ossification. *Journal of Bone and Mineral Research* **27,** 1004 (2012).

83. Hardy, D., Besnard, A., Latil, M., Jouvion, G., Briand, D., Thépenier, C., Pascal, Q., Guguin, A., Gayraud-Morel, B., Cavaillon, J.-M., Tajbakhsh, S., Rocheteau, P. & Chrétien, F. Comparative Study of Injury Models for Studying Muscle Regeneration in Mice. (2016). doi:10.1371/journal.pone.0147198

84. Sicari, B. M., Dziki, J. L., Siu, B. F., Medberry, C. J., Dearth, C. L. & Badylak, S. F. The promotion of a constructive macrophage phenotype by solubilized extracellular matrix. *Biomaterials* **35,** 8605–8612 (2014).

85. Saldin, L. T., Cramer, M. C., Velankar, S. S., White, L. J. & Badylak, S. F. Extracellular Matrix Hydrogels from Decellularized Tissues: Structure and Function. *Acta Biomater* **49,** 1 (2017).

86. Yang, W. & Hu, P. Skeletal muscle regeneration is modulated by inflammation. *J Orthop Translat* **13,** 25–32 (2018).

87. Kuswanto, W., Burzyn, D., Panduro, M., Wang, K. K., Jang, Y. C., Wagers, A. J., Benoist, C. & Mathis, D. Poor repair of skeletal muscle in aging mice reflects a defect in local, interleukin-33-dependent, accumulation of regulatory T cells. *Immunity* **44,** 355 (2016).

88. Biferali, B., Proietti, D., Mozzetta, C. & Madaro, L. Fibro–Adipogenic Progenitors Cross-Talk in Skeletal Muscle: The Social Network. *Front Physiol* **10,** 1074 (2019).

89. Kang, X., Yang, M. Y., Shi, Y. X., Xie, M. M., Zhu, M., Zheng, X. L., Zhang, C. K., Ge, Z. L., Bian, X. T., Lv, J. T., Wang, Y. J., Zhou, B. H. & Tang, K. L. Interleukin-15 facilitates muscle regeneration through modulation of fibro/adipogenic progenitors. *Cell Commun Signal* **16,** (2018).

90. Hernandez, M. J., Zelus, E. I., Spang, M. T., Braden, R. L. & Christman, K. L. Dose optimization of decellularized skeletal muscle extracellular matrix hydrogels for improving perfusion and subsequent validation in an aged hindlimb ischemia model. *Biomater Sci* **8,** 3511–3521 (2020).

91. Ungerleider, J. L., Johnson, T. D., Rao, N. & Christman, K. L. Fabrication and characterization of injectable hydrogels derived from decellularized skeletal and cardiac muscle. *Methods* **84,** 53–59 (2015).

92. Oral Cavity & Oropharyngeal Cancer Key Statistics 2021. at <https://www.cancer.org/cancer/oral-cavity-and-oropharyngeal-cancer/about/key-statistics.html>

93. Viktrup, L. & Lose, G. The risk of stress incontinence 5 years after first delivery. *Am J Obstet Gynecol* **185,** 82–87 (2001).

94. Viktrup, L., Rortveit, G. & Lose, G. Does the impact of subsequent incontinence risk factors depend on continence status during the first pregnancy or the postpartum period 12 years before? A cohort study in 232 primiparous women. *Am J Obstet Gynecol* **199,** 73.e1-73.e4 (2008).

95. Viktrup, L., Rortveit, G. & Lose, G. Risk of stress urinary incontinence twelve years after the first pregnancy and delivery. *Obstetrics and gynecology* **108,** 248–254 (2006).

96. Rubin, E. B., Buehler, A. E. & Halpern, S. D. States Worse Than Death Among Hospitalized Patients With Serious Illnesses. *JAMA Intern Med* **176,** 1557–1559 (2016).

97. Gao, J., Liu, X., Zuo, Y., Li, X. & Shalaby, M. N. Risk factors of postpartum stress urinary incontinence in primiparas: What should we care. *Medicine* **100,** E25796 (2021).

98. Wesnes, S. L., Hunskaar, S., Bo, K. & Rortveit, G. The effect of urinary incontinence status during pregnancy and delivery mode on incontinence postpartum. A cohort study. *BJOG* **116,** 700–707 (2009).

99. Van Brummen, H. J., Bruinse, H. W., Van De Pol, G., Heintz, A. P. M. & Van Der Vaart, C. H. Bothersome lower urinary tract symptoms 1 year after first delivery: prevalence and the effect of childbirth. *BJU Int* **98,** 89–95 (2006).

100. Meyer, S., Schreyer, A., De Grandi, P. & Hohlfeld, P. The effects of birth on urinary continence mechanisms and other pelvic-floor characteristics. *Obstetrics and Gynecology* **92,** 613–618 (1998).

101. Snooks, S. J., Swash, M., Setchell, M. & Henry, M. M. Injury to innervation of pelvic floor sphincter musculature in childbirth. *Lancet* **2,** 546–550 (1984).

102. Gunnarsson, M. & Mattiasson, A. Female Stress, Urge, and Mixed Urinary Incontinence Are Associated With a Chronic and Progressive Pelvic Floor/Vaginal Neuromuscular Disorder: An Investigation of 317 Healthy and Incontinent Women Using Vaginal Surface Electromyography. **18,** 613–621 (1999).

103. Theofrastous, J. P., Wyman, J. F., Bump, R. C., McClish, D. K., Elser, D. M., Bland, D. R. & Fantl, J. A. Effects of pelvic floor muscle training on strength and predictors of response in the treatment of urinary incontinence. *Neurourol Urodyn* **21,** 486–490 (2002).

104. Kamo, I., Torimoto, K., Chancellor, M. B., De Groat, W. C. & Yoshimura, N. Urethral closure mechanisms under sneeze-induced stress condition in rats: a new animal model for evaluation of stress urinary incontinence. *Am J Physiol Regul Integr Comp Physiol* **285,** (2003).

105. Memon, H. U. & Handa, V. L. Vaginal childbirth and pelvic floor disorders. *Womens Health (Lond)* **9,** 265–277 (2013).

106. Lane, F. L., Jacobs, S. A., Craig, J. B., Nistor, G., Markle, D., Noblett, K. L., Osann, K. & Keirstead, H. In vivo recovery of the injured anal sphincter after repair and injection of myogenic stem cells: an experimental model. *Dis Colon Rectum* **56,** 1290–1297 (2013).

107. Memon, H. U., Blomquist, J. L., Dietz, H. P., Pierce, C. B., Weinstein, M. M. & Handa, V. L. Comparison of levator ani muscle avulsion injury after forceps-assisted and vacuum-assisted vaginal childbirth. *Obstetrics and gynecology* **125,** 1080–1087 (2015).

108. Duran, P., Ward, S., Christman, K. L. & Alperin, M. Mechanical impact of parturition-related strains on rat pelvic striated sphincters. *Neurourol Urodyn* **38,** 912–919 (2019).

109. Sadeghi, Z., Isariyawongse, J., Kavran, M., Izgi, K., Marini, G., Molter, J., Daneshgari, F., Flask, C. A., Caplan, A. & Hijaz, A. Mesenchymal stem cell therapy in a rat model of birth-trauma injury: functional improvements and biodistribution. *Int Urogynecol J* **27,** 291 (2016).

110. Deng, K., Lin, D. L., Hanzlicek, B., Balog, B., Penn, M. S., Kiedrowski, M. J., Hu, Z., Ye, Z., Zhu, H. & Damaser, M. S. Lower Urinary Tract Symptoms: Mesenchymal stem cells and their secretome partially restore nerve and urethral function in a dual

muscle and nerve injury stress urinary incontinence model. *Am J Physiol Renal Physiol* **308,** F92 (2015).

111. Li, G., Yu, C., Yu, P., Peng, Q., Wang, Q., Ren, S., Li, H., Li, M., Li, P. & He, R. Periurethral and Intravenous Injections of Adipose-Derived Stem Cells to Promote Local Tissue Recovery in a Rat Model of Stress Urinary Incontinence. *Urology* **167,** 82–89 (2022).

112. Chermansky, C. J., Tarin, T., Kwon, D. D., Jankowski, R. J., Cannon, T. W., De Groat, W. C., Huard, J. & Chancellor, M. B. Intraurethral muscle-derived cell injections increase leak point pressure in a rat model of intrinsic sphincter deficiency. *Urology* **63,** 780–785 (2004).

113. Janssen, K., Deng, K., Majerus, S. J. A., Lin, D. L., Hanzlicek, B., Butler, R. S., van der Vaart, C. H. & Damaser, M. S. Transurethral versus suprapubic catheterization to test urethral function in rats. *Sci Rep* **11,** (2021).

114. Bachmann, G. & Santen, R. J. *Clinical manifestations and diagnosis of genitourinary syndrome of menopause (vulvovaginal atrophy)*.

115. Wysocki, S., Kingsberg, S. & Krychman, M. Management of Vaginal Atrophy: Implications from the REVIVE Survey. *Clin Med Insights Reprod Health* **8,** CMRH.S14498 (2014).

116. Peacock Kimberly, K. K. *Menopause*. (StatPearls, 2020).

117. Mac Bride, M. B., Rhodes, D. J. & Shuster, L. T. Vulvovaginal atrophy. *Mayo Clin Proc* **85,** 87–94 Preprint at https://doi.org/10.4065/mcp.2009.0413 (2010)

118. Anderson, D. J., Marathe, J. & Pudney, J. The Structure of the Human Vaginal Stratum Corneum and its Role in Immune Defense. *American Journal of Reproductive Immunology* **71,** 618–623 (2014).

119. Ali, A., Syed, S. M., Jamaluddin, M. F. B., Colino-Sanguino, Y., Gallego-Ortega, D. & Tanwar, P. S. Cell Lineage Tracing Identifies Hormone-Regulated and Wnt-Responsive Vaginal Epithelial Stem Cells. *Cell Rep* **30,** 1463-1477.e7 (2020).

120. Goldstein, I., Dicks, B., Kim, N. N. & Hartzell, R. Multidisciplinary Overview of Vaginal Atrophy and Associated Genitourinary Symptoms in Postmenopausal Women. *Sex Med* **1,** 44–53 Preprint at https://doi.org/10.1002/sm2.17 (2013)

121. Boreham, M. K., Wai, C. Y., Miller, R. T., Schaffer, J. I. & Word, R. A. Morphometric analysis of smooth muscle in the anterior vaginal wall of women with pelvic organ prolapse. *Am J Obstet Gynecol* **187,** 56–63 (2002).

122. Ghosh, M., Rodriguez-Garcia, M. & Wira, C. R. The immune system in menopause: Pros and cons of hormone therapy. *Journal of Steroid Biochemistry and Molecular Biology* **142,** 171–175 (2014).

123. Tomlin, H. & Piccinini, A. M. A complex interplay between the extracellular matrix and the innate immune response to microbial pathogens. *Immunology* **155,** 186–201 Preprint at https://doi.org/10.1111/imm.12972 (2018)

124. Tyagi, T., Alarab, M., Leong, Y., Lye, S. & Shynlova, O. Local oestrogen therapy modulates extracellular matrix and immune response in the vaginal tissue of post-menopausal women with severe pelvic organ prolapse. *J Cell Mol Med* **23,** 2907–2919 (2019).

125. Bachmann, G., Santen, R. J., Barbieri, R. L. & Burstein, H. J. *Treatment of genitourinary syndrome of menopause (vulvovaginal atrophy)*.

126. Angelou, K., Grigoriadis, T., Diakosavvas, M., Zacharakis, D. & Athanasiou, S. The Genitourinary Syndrome of Menopause: An Overview of the Recent Data. *Cureus* **12,** (2020).

127. Alperin, M., Burnett, L., Lukacz, E. & Brubaker, L. The mysteries of menopause and urogynecologic health: Clinical and scientific gaps. *Menopause* **26,** 103–111 (2019).

128. Naumova, I. & Castelo-Branco, C. Current treatment options for postmenopausal vaginal atrophy. *Int J Womens Health* **10,** 387–395 Preprint at https://doi.org/10.2147/IJWH.S158913 (2018)

129. You, S., Liu, S., Dong, X., Li, H., Zhu, Y. & Hu, L. Intravaginal Administration of Human Type III Collagen-Derived Biomaterial with High Cell-Adhesion Activity to Treat Vaginal Atrophy in Rats. *ACS Biomater Sci Eng* **6,** 1977–1988 (2020).

130. Johnson, T. D., Dequach, J. A., Gaetani, R., Ungerleider, J., Elhag, D., Nigam, V., Behfar, A. & Christman, K. L. Human versus porcine tissue sourcing for an injectable myocardial matrix hydrogel. *Biomater Sci* **2,** 735–744 (2014).

131. Johnson, T. D., Hill, R. C., Dzieciatkowska, M., Nigam, V., Behfar, A., Christman, K. L. & Hansen, K. C. Quantification of decellularized human myocardial matrix: A comparison of six patients. *Proteomics Clin Appl.* **10,** 75–83 (2016).